

E.T.S. de Ingeniería Industrial,
Informática y de Telecomunicación

Design of terahertz sensors based on metasurfaces for fungal infection detection



Grado en Ingeniería
en Tecnologías de Telecomunicación

Trabajo Fin de Grado

Irati Jáuregui López

Miguel Beruete, Pablo Rodriguez-Ulibarri

Pamplona, 28/06/2016

Acknowledgments

I would like to express my appreciation to every single person who helped me during my degree. Without them, I would not be the person I am today.

First, I want to extend my gratitude to Dr. Miguel Beruete for his warm welcome since the very first day, for making me become passionate about my work and for his constant and excellent guidance (both on a personal and scientific level). I would also like to express my gratefulness to Pablo Rodriguez Ulibarri, for helping me at many times during my work.

Throughout these years I've found and met extraordinary people with whom I've shared joys and sorrows. To all these good friends, thank you for being there and having become my other "family". A thank you as well to friends who I already had outside of college, whose friendships have been strengthened over this time.

And last but not least, my family. I feel very proud to have the family I do, and I would like to thank them for their constant love and support and for encouraging me during every difficult moment. Without them none of this would be possible.

Abstract

The proposed work is about the design of sensors in the terahertz band, for the detection of thin films, and microorganisms, in particular fungi. Firstly, a deep simulation study of the behavior of some metasurfaces and its performance as sensors, using the commercial software CST Microwave Studio has been performed. Three kind of structures have been studied: first, a cross-dipole structure, then a hole array structure, and finally, a densely packed frequency selective surfaces in two different configurations (transmission and reflection). Parametric studies have been carried out varying the concentration of microorganisms or the film thickness deposited on each structure. The optimization of structures with better prospects for biosensing applications have been undertaken. Once the statistical study of these structures was finished, an experimental study of the most promising ones has been carried out, using the instrumentation available in the TERALAB. The results demonstrate the promising perspectives of THz sensing based on metasurfaces.

Resumen

El trabajo propuesto trata sobre el diseño de sensores en la banda de terahercios para la detección de “thin films” y microorganismos, en particular de hongos. En primer lugar, se ha realizado un estudio profundo de simulación del comportamiento de varias metasuperficies para su uso como sensores de detección de invasiones fúngicas, mediante el software comercial CST Microwave Studio. Tres tipos de estructuras han sido estudiadas: en primer lugar, un “cross-dipole”, seguido de un “hole array” y, finalmente, una estructura selectiva en frecuencia, en dos configuraciones diferentes (transmisión y reflexión). Se han realizado estudios paramétricos variando la concentración de microorganismos o grosor de analito depositados sobre cada estructura. Se ha acometido la optimización de las estructuras con mejores perspectivas en la aplicación de biosensado. Una vez realizado el estudio estadístico de dichas estructuras, un estudio experimental de las más prometedoras, usando la instrumentación disponible en el TERALAB ha sido realizado. Los resultados demuestran las prometedoras perspectivas del sensado de THz basado en metasuperficies.

Key words

Terahertz, Extraordinary transmission, metasurfaces, metamaterials, sensors.

Index

| | |
|---|----|
| Acknowledgments..... | 1 |
| Abstract | 0 |
| Resumen..... | 0 |
| Key words | 0 |
| 1. Introduction and state of the art | 1 |
| 1.1. THz technology..... | 1 |
| 1.2. Metamaterials and metasurfaces | 5 |
| 1.3. Sensing at THz | 9 |
| 1.4. Regular and anomalous ET | 10 |
| 1.5. Outline..... | 11 |
| 2. Methodology | 12 |
| 2.1. Numerical simulator: CST Microwave Studio..... | 12 |
| 2.2. Experimental measurements: ABmm VNA analyzer | 14 |
| 3. Results and discussions | 16 |
| 3.1. Cross Dipole..... | 16 |
| 3.1.1. Patch structure (notch filter)..... | 16 |
| 3.1.2. Complementary (slot) structure (BPF) | 22 |
| 3.2. Hole Array..... | 28 |
| 3.3. Densely Packed Frequency Selective Surface | 42 |
| 3.3.1. Capacitive structure | 42 |
| 3.3.1. Inductive structure | 50 |
| 3.4. Experimental measurements | 59 |
| 4. Conclusions and future work | 64 |
| 4.1. Conclusions | 64 |
| 4.2. Future work..... | 65 |
| 5. Bibliography and references | 65 |
| 6. Author's merits..... | 68 |

1. Introduction and state of the art

1.1. THz technology

The terahertz (THz) band is the region of the electromagnetic spectrum that lies between microwaves and far-infrared. The exact boundaries are not clearly defined yet and still generate controversy. Following the classical band definition of microwaves the THz range falls between 0.1 and 10 THz, but some researchers from other communities extend the upper limit to 30 THz and the lower limit to 300 GHz. Along this document, we will stick to the most accepted definition of THz, in the range of 0.1 and 10 THz.

This band has been historically referred to as the “THz gap” due to the lack of efficient generators and detectors at this range. Radiation at lower frequencies such as microwaves, or at very high frequencies like infrared can be easily generated and the technology is nowadays mature. Nevertheless, it is not so simple at the THz band. As depicted in figure 1.1, the classical sources both from microwaves and infrared experiment an important power decrease in this band. With the apparition of new techniques such as the optical rectification and photomixing, as well as new THz sources like quantum cascade lasers (QCL), the situation has changed and now the THz band has opened a field of study of great interest.

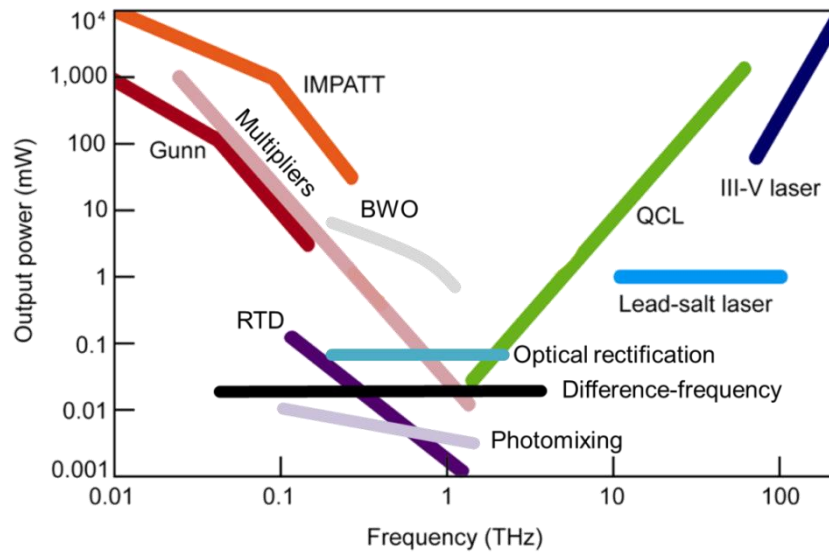


FIG. 1.1. The problem of generation. Power-frequency graphs of different sources in the THz band [M. Navarro’s personal communication].

Today, there are three principal techniques to generate and detect THz radiation: thermal sources, electrical, and optical (see figure 1.2). Next, the most used ones are explained:

- **Electro-optic method:** this is a non-linear process that consist in the generation of a change in the polarization of a laser beam. A femtosecond laser emits a laser beam trough a quasi-optical bench that confines the beam to a sensor. The spectral bandwidth of a femtosecond laser is pretty large if compared with the pulses duration.

The mixing of different frequency components in the process produces a beating polarization that results in radiation at the THz band.

- Photoconductive method: A dipole “photoconductive antenna”, usually called the “Grischkowsky antenna”[1] is used in this technique. A photosensitive material is placed between the two arms of the dipole where a voltage difference exists. When the antenna is gated on by a laser pulse, it creates charge carriers in the material giving rise to electron hole pairs. This results in an increase of the conductance and a current flow is generated, what results in THz radiation.
- Quantum Cascade Laser: the quantum cascade laser works with electric injection, and it is formed by regularly repeated energy levels, with small bandgaps, forming a succession of energy bands or cascades. The electron starts at the first level, and generates THz radiation, then jumps to the next level, where the process is repeated, so electrons emit THz radiation in every step. Even though this is the only technique capable to generate intrinsic THz radiation, it is the one least used, being the previous two techniques the most frequently in THz generation.
- Electric up-conversion: based on solid state frequency multipliers, using Schottky or GUNN diodes.

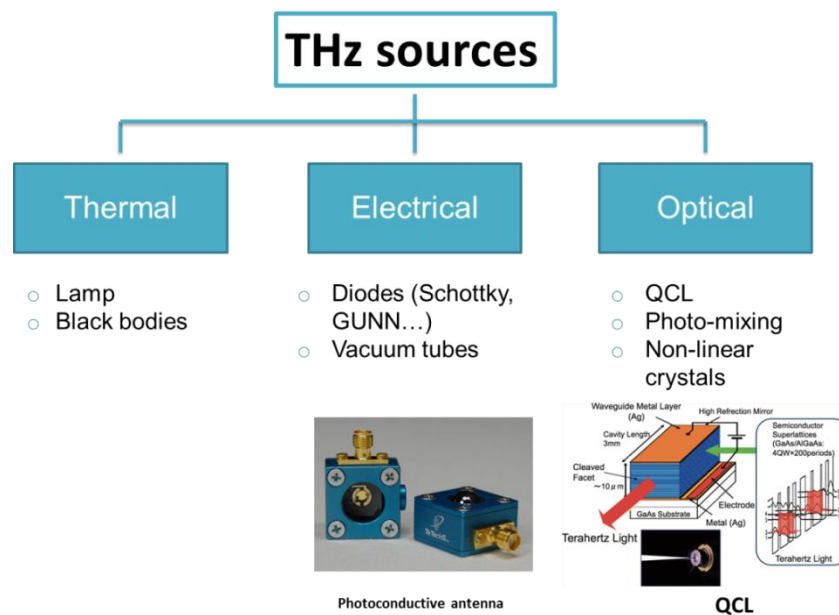


FIG. 1.2. Classification of THz sources.

Regarding the detection of THz radiation, the situation has also improved in the last decades. In the first THz detectors it was indispensable to cool the sources to cryogenic temperatures with the help of liquid nitrogen or helium. Today is much easier to detect THz radiation at ambient temperature thanks to the appearance of new and cheaper detectors based on microwave heterodyne detection or photomixing [2] among others. A classification of THz detectors is shown in figure 1.3.

- Thermal detectors: All of them are based on temperature changes. When a THz radiation falls on a thermal detector, it produces an increment of its temperature, causing physical changes such as expansion given that the absorber has a thermal conductance. The radiated power is given as a function of this thermal conductance and the temperature difference. This kind of detectors are incoherent, this means that they only detect the amplitude but not the phase. Some examples of thermal detectors are:
 - Bolometers
 - Photo-acoustic detectors
 - Golay cells
 - Pyroelectric effect-based detectors
- Electro-optic detectors: similar to the electro-optic generation. The presence of THz radiation in electro-optic materials causes a change in the refractive index. This change can be monitored by a light beam falling on the material, and it changes with the beam polarization. The electro-optic detectors use beams with different delays and polarizations, using normally a quarter-wave plate and a Wollaston prism. This kind of detection is coherent, which means that they can recover both the amplitude and phase of the signal. With coherent detectors, the speed of detection can be very fast, and the THz signal can be sampled on a very short time scale.
- Photoconductive detectors: when THz radiation falls on a photoconductive material, its conductivity changes. Despite the fact that the THz photons have very low energy to create new electron-hole pairs, they can modulate a pre-existing current produced by a probe beam by photoexcitation. As electro-optic detectors, this is also coherent detection, and both are the basis of time-domain spectroscopy.

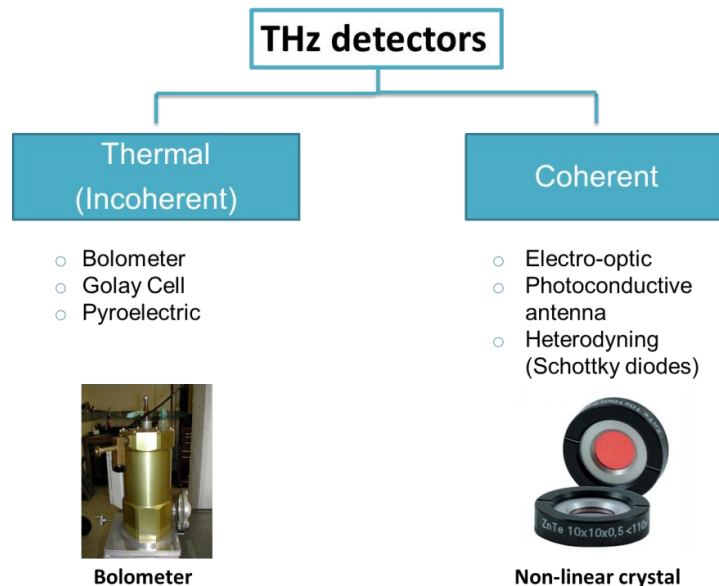


FIG. 1.3. Classification of THz detectors.

These discoveries have opened up the door toward exciting applications in the THz band, unexplored until now due to the difficulties in the signals generation and reception. Nowadays, the THz band is attracting considerable interest in many applications such as spectroscopy and imaging, sensing, communications and medical diagnostic, among others.

Communications

Nowadays, a number of reasons make communications at the THz band very attractive. In the first place, this band is a developing region of the spectrum. Contrarily to the region of microwaves, where the spectrum is collapsed, there is a lot of bandwidth available in the THz gap, in addition to the larger bandwidth allowed by the THz carriers. Some communications like radar or satellite networks can benefit from the small antenna sizes needed to produce signals at THz band, due to the limited payload. One of the main disadvantages of THz communications is the absorption through the atmosphere because of water vapor, but this is not a problem for satellite communications that occurs in the stratosphere, where the scattering is much lower in comparison with the one produced at IR or microwaves (proportional to f^2 instead of f^4) [3]. Besides, in security applications the signals attenuation is a plus for THz radiation when one does want to preserve certain information from being accessible out of a particular place or room.

Spectroscopy and imaging

The technique of THz spectroscopy is based on Fourier analysis of the time dependence of a laser pulse. The analysis is based on the absorption peaks as a function of frequency.

As THz waves have less energy than IR waves, they can excite vibrations of higher wavelength. That results in molecular vibrations in organic materials that are unique for each material and differentiate it from others. This is a great advantage, given that with THz it is possible to identify dangerous or even explosive materials from non-hazardous materials, even though they might have similar or identical physical appearance. It is also possible the imaging through low loss dielectric materials with very high resolution. In particular, THz waves are able to penetrate through clothes. This property has been exploited in modern see-through-cloth radars that are now operating in security applications, for example at airports. With them it is possible to detect weapons or dangerous objects like explosives, etc. under several layers of clothing. As is well-know, the imaging resolution depends on how small the beam diameter is (the smaller the diameter, the higher the resolution), and the wavelength size. Small beam diameters can be produced by using mirrors or glasses. Moreover, the wavelength at THz is of the order of hundreds of microns. Hence, it is possible to get accurate images of objects.

THz technology is also making an impact in the pharmaceutical industry. Not being an invasive technique is perfect for detecting polymorphisms and solid crystal properties in pharmaceutical products like drugs or beauty products.

Medical diagnosis

One of the main benefits of THz technology is that the radiation is nonionizing, and therefore exposure is not harmful, at difference with X rays. This makes an advantage of using

THz to imaging tumors in skin or breast tissue without invasive surgery. THz waves have limited penetration depth in human tissue because of the strong water absorption, opening the possibility to radiate skin tumors without affecting any organ or tissue deeper. Some studies have demonstrated that carcinogenic cells have different percentage of moisture. Because THz absorption is sensitive to polar molecules, reflections of cancer issue can be detected. These kinds of cells usually have also different refractive index (a higher one), so their frequency response is different and, therefore, easy to detect.

1.2. Metamaterials and metasurfaces

In 1968, Veselago (considered the father of metamaterials), proposed for the first time a medium with simultaneous negative permittivity and permeability [4]. He found that in these media, the phase and group velocity are antiparallel (opposite direction). This, makes the refraction index negative, and the vectors E (electric field), H (magnetic field), and k form what is called a left-handed triplet (they follow the left-hand rule). These media have interesting properties like inverse Snell's law (see figure 1.4), or inverse Doppler effect, among others.

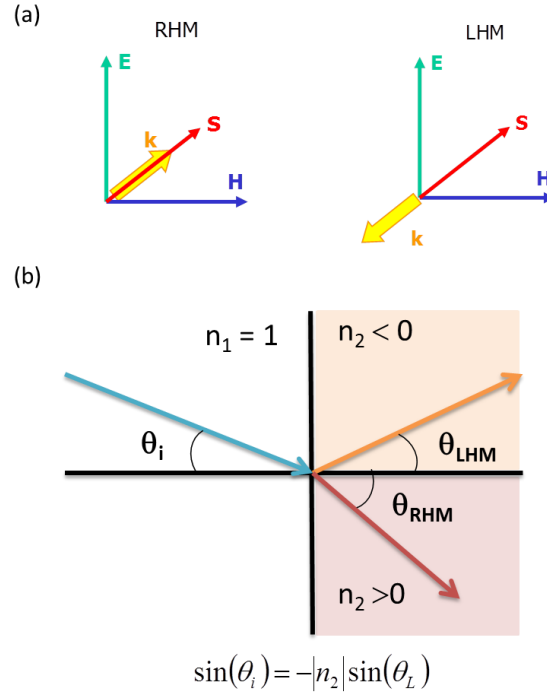


FIG. 1.4. (a) left-handed-triplet and left-handed-triplet representation. (b) Schematic of Snell's law in a media with positive refractive index and in a media with negative index.

In 1999, Pendry proposed a subwavelength structure with a strong magnetic response using non-magnetic components, the so-called Split Ring Resonator (SRR), see schematic in figure 1.5(a) [5]. Under an axial magnetic field excitation, this structure is able to produce a negative permeability within a narrow frequency range around the first resonance. After this, it was in the year 2000 when Smith achieved the first experimental demonstration of metamaterials, synthesizing a medium with both negative permittivity and permeability (i.e. double negative media) [6]. Smith and co-workers fabricated a prototype based on the combination of a matrix of SRR, with $\mu < 0$ (whose frequency response presents a dip in the

transmission); and an array of thin straight wires, with $\varepsilon < 0$ (whose frequency response presents another dip in transmission) Combining both types of arrays, a new prototype was created, whose frequency response presents a peak of transmission (see figure 1.5(b)).

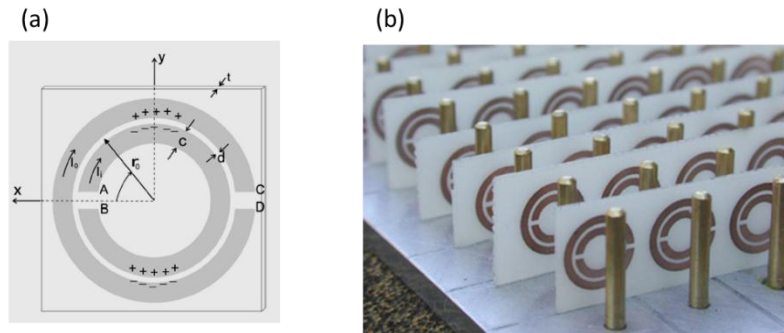


FIG. 1.5. (a) Schematic of Pendry's SRR. (b) Prototype of Smith's DNM material

In 2000, Pendry revolutionized the metamaterials research by proposing the Pendry's lens [7]. This lens was composed of a slab of negative refractive index material (with $\mu = \varepsilon = -1$), that was able to regenerate the image with all its components, i.e. with infinite resolution (ideally), although in practice this is not possible due to the material losses. The operation of this lens is shown in figure 1.6.

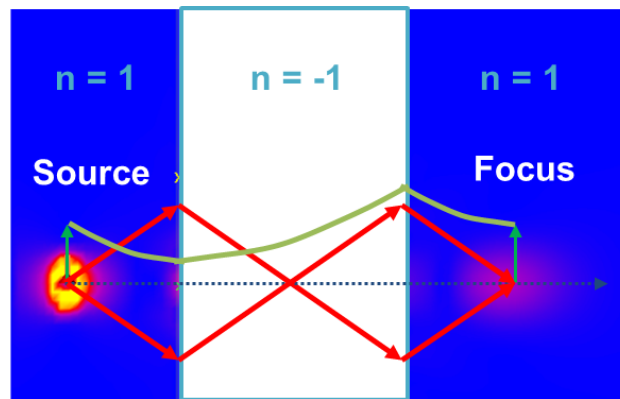


FIG. 1.6. Operation of perfect Pendry's lens.

The other great landmark in metamaterials history was the possibility to obtain an invisibility cloak. Invisibility can be achieved by developing metamaterials that deflect electromagnetic waves so that they do not interact with the concealed object, making it invisible to an external observer. Even though cloaking still have many imperfections, this has become a very interesting field of study for many researchers [8][9].

A possible definition of metamaterials was suggested by Roger M. Walser in 1999:

"Metamaterials are macroscopic composites having man-made, three-dimensional, periodic cellular architecture designed to produce an optimized combination, not available in nature, of two or more responses to specific excitation."

Sixteen years after Walser's statement, the definition of metamaterials has evolved enormously, encompassing a great deal of artificial structure, but they are still based on the idea of combining elementary particles that present a desired electromagnetic response. As we cannot create new elements, the solution to create new materials with properties beyond natural materials are the metamaterials.

Metamaterials are constructed by a collection of unit cells or resonators with sizes much smaller than the operation wavelength, so an electromagnetic wave sees an homogenous medium. In electromagnetism, the materials are characterized by their dielectric permittivity, ϵ , and magnetic permeability, μ . There are four different classes of metamaterials depending on the sign of ϵ and μ , like is shown in figure 1.7:

- Double-positive metamaterials (DPS) or right-handed media: both ϵ and μ are positive.
- Double negative metamaterials (DNG) or left-handed media: both ϵ and μ are negative.
- Negative permittivity media (ENG): where ϵ is negative and there is no propagation.
- Negative permeability media (MNG): where μ is negative and there is no propagation.

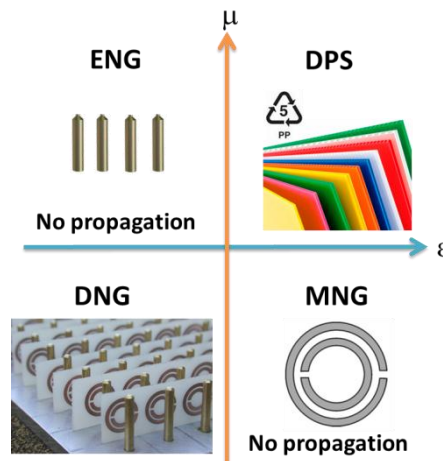


FIG. 1.7. Classification of material in the permittivity-permeability plane.

Each resonator that forms metamaterials produces a frequency response, typically a resonance. This resonance may result in a band-pass, if the structure presents a peak at resonance; or notch response, if the structure presents a dip at resonance. The frequency of this resonance can be modified by varying the structure dimensions. This means that metamaterials can be scaled. The unit cells of metamaterials are usually formed by a metallic thin film lying on a dielectric substrate, with a Lorentzian resonance response that is comparable to the one obtained from a RLC filter circuit, where the capacitance, C , and the inductance, L , are determined by the properties of the dielectric substrate and the metallic film [10].

Metamaterials (3D structures) evolved soon towards metasurfaces (2D structures) because of the obvious advantages as can be space saving, or manageability. Metasurfaces are

planar screens designed to be transparent (or not) in some frequency bands while reflective, or absorbing to others. Although they require micro and nano system technology or planar technology for their fabrication, with nowadays technology they are easier to create than 3D structures. Because of this, many sensors are based on them. They are generally designed by assembling arrays of resonators whose size and spacing between them are much smaller than the wavelength; and with geometric parameters (shape, size, etc.) that can be modified to create a desired frequency response.

There are many types of metasurfaces (capacitive, inductive, absorbent, etc.) and with different behavior (notch filters, band pass filters, etc.). There are also some type of structures, called “Wallpaper materials” [11]. These are formed by several periodic stacked metal + dielectric structures. In this group, two kind of structures can be highlighted:

- Metasurfaces based on thin films: composed of a lossy dielectric film lying on a substrate material (see figure 1.8(a)). By choosing correctly the substrate and dielectric materials, the phase that the incident wave undergoes when reflected at the interface between air and the dielectric, or between the dielectric and the substrate, can be controlled, making it possible to engineer the reflection spectrum. As these films are much smaller than the wavelength, as said before, a semi-infinite equivalent medium with the same spectrum that the one presented by the structure can be defined, so the structure can be considered as a metamaterial with controllable impedance and refractive index.
- 2D structures with a repeated pattern on a surface (substrate). The planar unit cell of these structures present electric or magnetic properties, so the cell that is repeated on the structure is an electric or magnetic particle, such an SRR (nonmagnetic ring structure with one or more splits filled with dielectric that can have many different geometries), square pattern, cross pattern, etc. (See figure 1.8(b)).

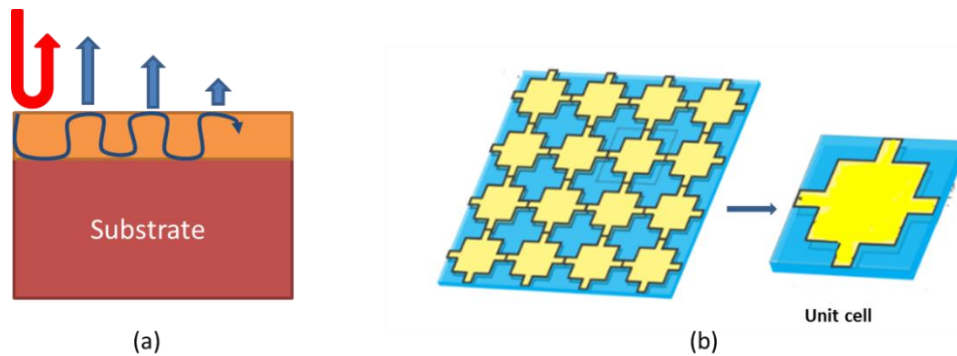


FIG. 1.8 (a) Reflection process from a thin film over a lossy substrate. (b) Schematic of a metamaterial slab formed by a composition of unit square cells [12].

Currently, the study of metamaterials and metasurfaces is a field of great interest to many researchers, and are used for many applications such as cloaking devices, polarizers, analog computing and sensing, among others. Here, we will focus just on the sensing applications. The rest of applications are beyond this study, but they can be consulted in many reviews and articles about the subject [13][14][15].

1.3. Sensing at THz

Nowadays, sensing is one of the most interesting THz applications, due to its importance in numerous applications such as quality control, medicine, security, etc. In particular, there are some sensing devices based on plasmonics, metamaterials, and frequency selective surfaces, among others. One of the main objectives of this work is the detection of biological substances (fungi, in our case), and the design of thin film sensors using THz radiation. In the literature one can find some studies focused on this field, amongst which we can highlight the next ones:

- S. J. Park and co-workers used metallic arrays of square ring with a micro-gap at the center, for penicillium sensing [16].
- Lijuan Xie and co-workers, used a square-shaped metallic structure to detect trace amounts of molecules of kanamycin sulfate (antibiotic) [17].
- L. Cong *et al.* presented two different perfect metamaterial absorbers to use them as sensors [18].
- The antennas group also have experience in sensing at THz using metasurfaces [19].

The objective of a sensing device is to identify the presence of some analyte or sample on the structure. The deposition of the sample should introduce a visible change of the properties in the empty structure. This change may be a shift of the frequency, amplitude, or any other visible parameter.

The key parameters for sensing are sensitivity, resonance linewidth, and figure of merit (FoM) [19]. The sensitivity is a parameter designed by the researcher, and depends on the field of study and application. For this reason, is not easy to give a global definition. One of the questions that sensitivity has to answer about the sample is: can it be identified with no ambiguity? [10]. In our case, we define the sensitivity as a ratio between the resonance frequency shift (Δf_R) (or amplitude) with the variation of the refractive index:

$$S = \Delta f_R / \Delta n \text{ [Hz/RIU]} \quad (1)$$

Nevertheless, it can be related also with other parameters such as the concentration, or the analyte thickness, for example. In this work, the parameter chosen will depend on the kind of the sensor:

- Refractometer: $S = \Delta f_R / \Delta n$.
- Thin film sensor: $S = \Delta f_R / \Delta h_a$ (being h_a the analyte thickness).
- Fungi detector: $S = \Delta f_R / \Delta N$ (being N the fungi concentration).

The resonance linewidth is also known as the full-width at half-maximum (FWHM) and is related with the width of a pulse, in our case, the resonance (peak or dip). It is important not just having high values of sensitivity, but also a narrow FWHM. For this reason, the parameter used to measure the quality of a sensor is the figure of merit (FoM). The FoM is a relation between the sensitivity and the FWHM and is defined as below (equation 2). This means, that the higher the sensitivity and narrower the FWHM, the higher the quality of a sensor.

$$\text{FoM} = S/\text{FWHM} \quad (2)$$

1.4. Regular and anomalous ET

In 1998, T. W. Ebbesen and co-workers analyzed two-dimensional arrays of cylindrical cavities in metallic films and found sharp peaks in transmission at wavelengths as large as ten times the diameter of the cylinders [20]. They named this phenomenon as extraordinary optical transmission (EOT), since the peaks took place in the cutoff regions of the holes. In 2000, Avrutsky *et al.* found that ET appeared in a structure with only periodic corrugations [21]. Later on, in 2004, extraordinary transmission (ET) in millimeter waves was demonstrated, generalizing the phenomenon [22]. Since then, the ET has been a phenomenon of great attention given that it provides potential applications, particularly in the field of metamaterials and plasmonics. It is now well established [23][24] that ET occurs in periodic metallic structures with electric holes where the periodicity is much larger than the diameter of the holes. Now, eighteen years later, all these theories have evolved, most of them focusing on the applications of the ET, as done in this work.

This phenomenon refers to the appearance of peaks of transmission at certain frequencies below cutoff when the polarization is parallel to the large periodicity which correspond to the regular ET resonance. The ET resonance when the distance between the holes in the structure is comparable to the wavelength and is much larger than the hole size. Additionally, if a rectangular cell is used and the structure is loaded with a dielectric substrate they can also support transmission below cutoff for the polarization parallel to the short hole periodicity, a phenomenon called anomalous ET [25][26][24]. In the anomalous ET, the appearance of zeros and poles is strongly conditioned by the F factor defined in [25], a parameter described as follows:

$$F = \frac{h\sqrt{\epsilon-1}}{d_y} \quad (3)$$

Depending on the value of the F factor we can distinguish among different performances:

- If $F \geq 0.25$, there will be a frequency, known as Wood's frequency, where we will have a null of transmission, called Wood's anomaly.
- If $F < 0.25$, a pole does not appear at any frequency.

1.5. Outline

In this work three different types of metasurfaces are presented and its behavior as refractometer, thin film sensor or fungi detector is evaluated. This document has been organized as follows:

- In chapter 2, the numerical simulator and the vector network analyzer used in this work are explained.
- In chapter 3 different structures are designed and their behavior as sensor is numerically evaluated:
 - In chapter 3.1 a cross-dipole structure in both notch filter and band-pass filter configurations is presented, and its behavior as a fungi detector is evaluated in both cases.
 - In chapter 3.2 a hole array structure is designed to work at the frequency of 850 GHz. Its behavior as a thin film sensor, refractometer and fungi detector is evaluated and discussed.
 - In chapter 3.3 two different densely packed frequency selective surfaces (DP-FSS) are presented, one of them in transmission configuration, and the other in reflection configuration. The behavior of both of them as refractometer and fungi detector is evaluated and a comparison of the two configurations is carried out.
 - In chapter 3.4, experimental measurements are performed and compared with the numerical results obtained in the previous chapter.
- Finally, the conclusions of this study and future work in the field, added to the bibliography used to make this work and the author's merits are presented in the last chapters of this document.

2. Methodology

2.1. Numerical simulator: CST Microwave Studio

CST Microwave Studio is an electromagnetic full wave simulation software founded in 1992 by Thomas Weiland. It was an evolution of the MAFIA packet software: “solving Maxwell’s equations using the Finite Integration Algorithm”, introduced in 1977, based on the Finite Integration (FIT) technique.[27]

Today CST is one of the main commercial tools for the 3D electromagnetic simulation of high frequency components. It offers multiple templates according to the area of study and solvers modules integrated into one user interface so that the user can choose the most appropriate for a given problem class.

CST MWS contains several solvers to best suit a given problem class (transient solver, frequency domain solver, eigenmode solver, resonant solver, integral equation solver, asymptotic solver, and TLM solver). To solve the electromagnetic problem, the simulation domain is first divided in small cells, wherein Maxwell’s equations are solved. The program offers different meshing options, being the main ones hexahedral and tetrahedral mesh. With the hexahedral mesh, the whole simulation domain is divided into small cubes (either of uniform or varying size) whereas with the tetrahedral mesh, only the objects are divided in small tetrahedrons and the rest of the simulation domain is left unmeshed. Due to the intrinsic features of each mesh type there are some fundamental differences. The most relevant difference for this project is that hexahedral meshes do not conform to material jumps whereas tetrahedral ones conform to solid-boundaries and consequently conform to material jumps. With both hexahedral and tetrahedral meshes, there are two options to choose[28]:

- Automatic mesh generation: the mesh generator creates automatically a mesh that fits the simulated structure and the electromagnetic fields.
- Adaptive mesh refinement: the software makes repeated simulations and evaluates different solutions, recognizing regions where the mesh needs to be locally refined. Although this option spends more simulation time, it also provides improved accuracy.

The mesh influences the accuracy and speed of the simulations. Small mesh cells usually lead to more accurate solutions but at the expense of increasing the computation time and vice versa. Regarding hexahedral or tetrahedral performance, generally hexahedral meshes take shorter simulation time, whereas tetrahedral meshes are more accurate with the presence of small or curved dielectric solids. For these reasons, it is difficult to give a general statement of which mesh is better for a given problem class. Therefore, the software offers different mesh types depending on the solver type used. An example of hexahedral and tetrahedral mesh can be shown in figure 2.1.

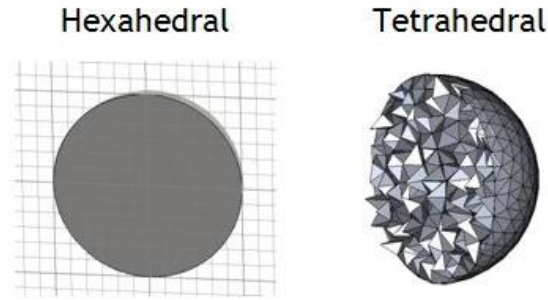


FIG. 2.1. Example of hexahedral and tetrahedral meshing of a sphere[28]

In this work, the problem under study is based on planar periodic structures. This type of structures fits with the template “Frequency Selective Surfaces (FSS)”. With this template the following simulation parameters are automatically defined:

- Template: FSS - Unit Cell
- Units: mm, GHz
- Solver: Frequency Domain Solver
- Meshing: tetrahedral meshing
- Background: vacuum
- Boundaries: x, y unit cell (phase shift defined by the angle of incidence inward traveling plane wave).
- Floquet port: Zmin+Zmax

It is observed that the transversal boundary conditions are “Unit Cell”. In periodic structures a single, unit cell is sufficient to describe the whole structure that contains an infinite matrix of identical elements periodically replicated. Working with the unit cell, Floquet ports appear automatically in Zmin and Zmax, so that is not necessary to draw them.

Frequency Domain Solver:

The frequency domain solver is a general purpose simulator. It delivers electromagnetic near- and far-fields as well as S parameters, among other electromagnetic parameters. Although the transient solver also delivers broadband frequency results like S parameters, the frequency domain solver is preferable for the calculation of electrically small structures or with high Q-value. It can work with hexahedral or tetrahedral meshing, although the latter is usually preferable. The frequency domain solver is also ideally suited (in fact, the only choice in CST) for periodic structures.

Tetrahedral and Surface mesh generation:

The procedure to create a tetrahedral mesh can be explained in three steps[28] (See figure 2.2):

1. Building a non-manifold simulation model: this operation is to convert two coincident faces of two solids into a single common double-sided face, so we can generate a consistent mesh with identical mesh cells at the edge of both solids.

2. Meshing edges and faces (surface meshing).
3. Meshing the model's volumes based on surface meshing (volume meshing).

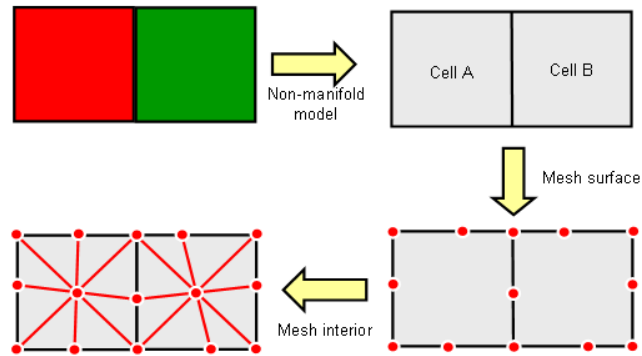


FIG. 2. 2. Tetrahedral mesh generation procedure [28]

Once the tetrahedral mesh is created, we can improve its quality by using mesh smoothing or mesh optimization, which swaps faces and edges reconnecting them to generate better quality tetrahedrons.

2.2. Experimental measurements: ABmm VNA analyzer

For experimental measurements of the fabricated metasurfaces the Vector Network Analyzer (VNA) MVNA-8-350-4 [29] available in the Antennas Group – TERALAB of UPNA has been used. This analyzer covers the frequency range from 8 GHz to 1 THz, and it measures the complex, (or vector) impedance in the millimeter and sub-millimeter frequency domain. The detection system includes a tunable microwave source and a detector, frequency stabilization unit, data acquisition and data processing system. It provides both, the amplitude and phase of the transmitted and reflected signal. The operational and logical control of the analyzer is done with a PC computer. The MVNA used in this work is shown in figure 2.2.

The basic configuration of the MVNA-8-350 is:

- MVNA central unit
- PC computer with interface cards, with the software package
- Graphic printer attached to the PC computer
- Control oscilloscope visualizing at real time the detected waves



FIG. 2. 2. UPNA's MVNA-8-350-4

As the MVNA-8-350 covers different bands it has different multipliers heads that provides the availability of sources for each band. In the MVNA the beam is transmitted by a corrugated horn antenna, and is converted to intermediate frequency by a Schottky diode harmonic mixer. Then, the signal generated goes through a quasioptical bench formed by 2 pairs of elliptical mirrors that confine the signal beam and collimate it on the sample, avoiding diffraction. Ideally, the beam radius at the sample position is minimum. Then, another pair of mirrors focuses the beam into the receiving antenna, and the high frequency signal is processed in the heterodyne vector receiver. In the reflection configuration, only one antenna is necessary, and acts as a generator and receiver at the same time. In this configuration is necessary to add a coupler to the design. The signal reflected on the sample is measured (See figure 2.3).

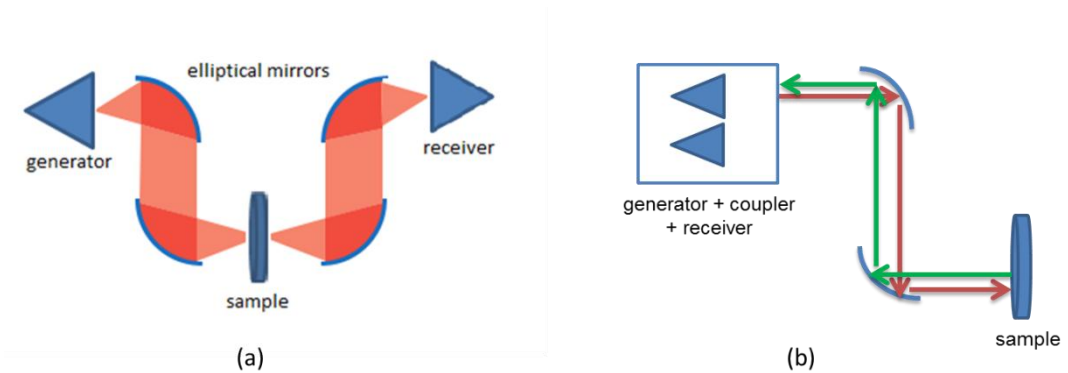


FIG. 2. 3. Scheme of MVNA operation (a) Transmission configuration. (b) Reflection configuration.

16. Results and discussions

In this chapter, three kind of structures are presented. Their behavior as sensors is going to be numerically evaluated. Statistical studies as well as quality parameters like sensitivity and FoM have been calculated and are discussed in this chapter.

3.1. Cross Dipole

In this section, two different frequency selective surfaces (FSS) based on a patch and slot cross-dipole elements are evaluated. Their performance as biological sensors (fungi detection) is numerically evaluated.

3.1.1. Patch structure (notch filter)

The first FSS analyzed is an array of cross-dipole patch elements. The schematic and dimensions of a unit cell structure are shown in figure 3.1(a). It consists of a metallic patch of hollow cross shape with a strip width of $2\ \mu\text{m}$ and infinitesimal thickness, periodically repeated with period $d_y = 100\ \mu\text{m}$ on top of a thin polypropylene (PP) layer of thickness $40\ \mu\text{m}$ and permittivity $\epsilon_{pp} = 2.25$. PP has been chosen due to its optimal features at THz like low absorptivity and dispersion, as well as its resistance against various chemical solvents and acids, and the fact that it is a ductile material. The analysis is done assuming loss-less elements, so the loss tangent of PP is disregarded and the metallic cross is modelled as a perfect electric conductor (PEC).

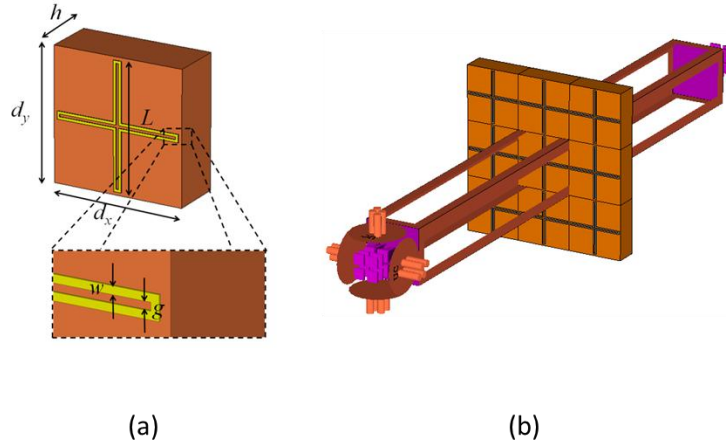


FIG. 3.1. (a) Schematic of the designed unit cell. Dimensions: polypropylene substrate height, $h = 40\ \mu\text{m}$; unit cell lateral period, $d_x = d_y = 100\ \mu\text{m}$; cross length, $L = 95\ \mu\text{m}$; cross track width, $w = 2\ \mu\text{m}$; gap between metallic strips, $g = 2\ \mu\text{m}$. Dielectric properties of the substrate: PP permittivity, $\epsilon_{pp} = 2.25$. (b) Boundary conditions of the unit cell.

The aim of this study is to verify the behavior of this cross dipole FSS structure as a biological sensor and, more concretely, to prove its performance as a fungi detector. To accomplish it, several simulations have been carried out depositing a different concentration of fungi each time, with the purpose of checking whether we are able to find some parameter that allows us to discriminate between different fungi concentrations deposited on the FSS.

For modelling purposes, fungi were characterized as spheres, with a radius of 2 μm and a permittivity $\epsilon_{\text{fungi}} = 8$.

The structure shown in figure 3.1 was simulated using the electromagnetic software CST Microwave Studio. It was characterized under normal and oblique incidence (for both TE and TM polarizations). Note that under normal incidence this is equivalent to using linear orthogonal polarizations, vertical and horizontal. To model the FSS as an infinitely periodic structure, the simulation characteristics mentioned in the methodology chapter were applied: Unit Cell boundary conditions in x and y axes, and Open + Add Space (i.e. perfectly matched layers) in z axis. The structure was simulated in the frequency span from 600 GHz to 900 GHz.

Figure 3.2 shows the transmission in dB of the cross-dipole FSS without fungi. As we can observe, the structure presents a stop-band resonance at the $f_R = 832$ GHz. This is due to the metallic cross-dipole fundamental dipolar half-wavelength resonance. In a first order approach, this resonance frequency is determined by the cross length, L , by the effective permittivity seen by the FSS, which is different from the PP permittivity and the capacitance between the metal strips, which reduce the resonance frequency. As the FSS is also in contact with air (with a relative permittivity of 1), and because the substrate can be considered semi-infinite ($h \geq 0.1 \cdot \lambda_R$, being λ_R the resonance wavelength), the effective permittivity for the substrate ϵ_{eff} , can be calculated as the arithmetic mean of both polypropylene and air : $\epsilon_{\text{eff}} = \frac{2.25+1}{2} = 1.625$ [19]. In our case $L \approx \lambda/2 = 0.1$ mm, so $\lambda = 0.2$ mm. The resonance frequency in vacuum should be $f_0 = c / \lambda = 1.5$ THz. If we consider the presence of the PP substrate, the frequency in this case should be $f = f_0 / \sqrt{\epsilon_{\text{eff}}} = 1.27$ THz. This value is quite different from the real resonance frequency, which demonstrates the strong effect of the capacitance between the metal strips mentioned before.

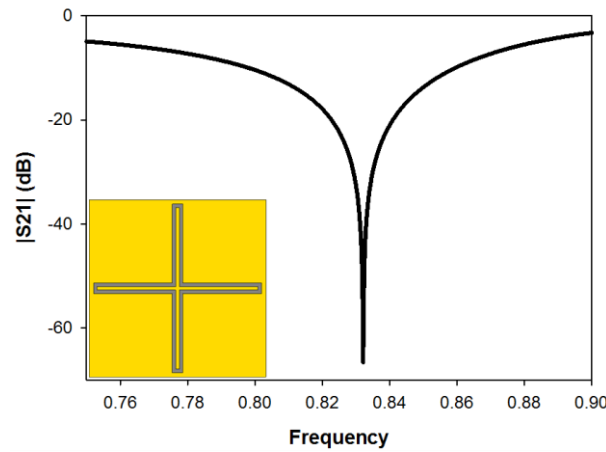


FIG. 3.2. Transmission of the cross-dipole under normal incidence and without fungi.

Next, the performance in the presence of fungi was evaluated. The response was analyzed by depositing different amounts of fungi, from 0 to 250 with a step width of 50. In order to bring the measurement as close as possible to reality, 10 simulations were made for each case, with the corresponding statistical study: average and variance for each case. The spheres that model the fungi microorganisms were created and placed on the structure with a

random distribution, using an external MatlabTM script explicitly written for this application. In this way it was ensured that in principle all simulations were different. The results of this study are shown in figure 3.3.

As observed there, the resonance shift for each case is pretty different and, as we can see in figure 3.4, strongly depends on the spheres distribution over the FSS. The variance in all cases is moderately high in comparison with the average frequency shift achieved, causing an overlap between different fungi concentrations.

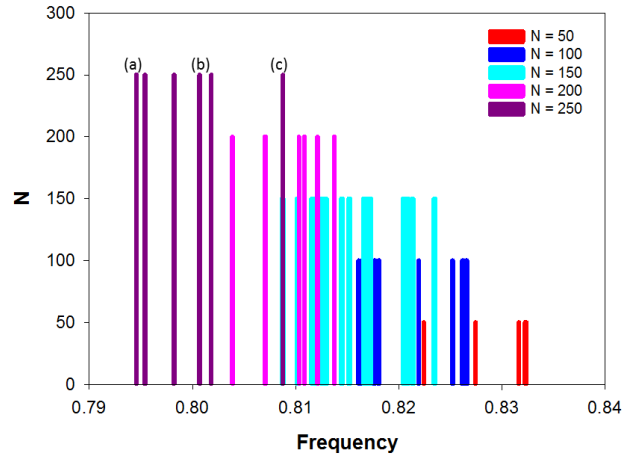


FIG. 3.3. Representation of the frequency resonance for all the simulations carried out for each fungi concentration.

| N | Frequency resonance for different simulations (GHz) | | | | | | | | | | Average (GHz) | Variance |
|-----|---|-------|-------|-------|-------|-------|-------|-------|-------|-------|---------------|----------|
| 0 | | | | | | | | | | | 832 | |
| 50 | 827.4 | 822.4 | 832.2 | 827.4 | 822.4 | 832.4 | 832.4 | 831.6 | 822.4 | 827.4 | 829 | 144.2 |
| 100 | 816.1 | 826.6 | 825.2 | 826.5 | 822.0 | 817.7 | 818.1 | 826.6 | 826.2 | 818.0 | 821.6 | 18.7 |
| 150 | 808.7 | 810.2 | 815.2 | 816.9 | 812.3 | 816.6 | 817.2 | 823.5 | 820.8 | 820.5 | 815.6 | 19.7 |
| 200 | 810.9 | 803.9 | 807.0 | 801.8 | 807.1 | 813.7 | 810.3 | 812.1 | 807.1 | 803.9 | 806.9 | 16.4 |
| 250 | 795.4 | 800.7 | 794.6 | 795.4 | 800.7 | 794.6 | 801.8 | 798.2 | 808.8 | 800.7 | 799.1 | 19.7 |

Table 3.1. Frequency resonance for all the simulations carried out for each fungi concentration, average and variance for each case

This variation of the frequency resonance may be due to the arrangement of the spheres in the structure. To check this hypothesis, the distribution of spheres corresponding to the extreme results with $N = 250$ have been represented in figure 3.4. This case is chosen because is the one with higher frequency variation. The resonance shift is due to the higher or lower interaction between the induced electric field and the spheres. The highest interaction will occur in areas where the metal acts as a capacitor, that is, between the two metal strips of the cross. If we take a look at that area in figure 3.4, we can see that, indeed, the number of spheres within the metallic strips is about 26 in the case corresponding to the simulation with largest frequency redshift, figure 3.4(a). Whereas in figure 3.4(c), the number of spheres within the strips is, approximately, 19. Thus, we have a difference of 27% between both cases. By looking the intermediate case at figure 3.4(b), it can be observed that the number of spheres

within the strips is about 22, what corresponds approximately with the average between both cases.

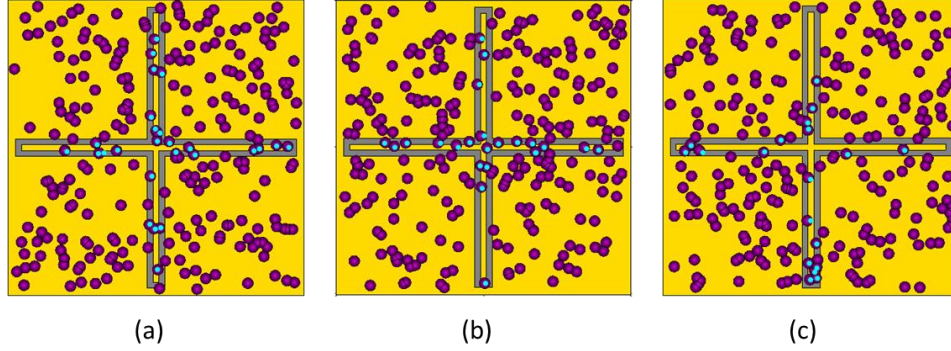


FIG. 3.4. Distribution of spheres on simulations corresponding to the edges of the case $N = 250$. (a) Highest frequency variation (resonance at 794 GHz). (b) Intermediate case (resonance at 800 GHz). (c) Lowest frequency variation (resonance at 808 GHz).

As mentioned above, there are frequency shifts from different concentrations that are overlapped. Then, the study can be cumbersome. To overcome this, we have calculated the average frequency shift for each case, and chosen the simulation that was closest to the average. A schematic of the front view of the structure is represented in figure 3.5(a). For clarity, only the cases for $N = 50$, $N = 150$ and $N = 250$ are represented. We have taken the curves closest to the average, so the effect of overlapping disappears, and represented them in figure 3.5(b).

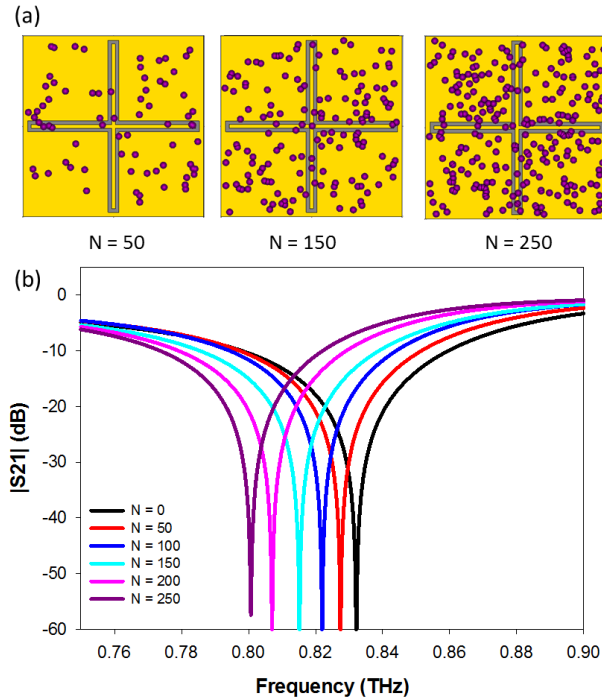


FIG. 3.5. (a) Front view of the structure with $N = 50$, $N = 150$, and $N = 250$ fungi (purple spheres). (b) Results of simulated transmission without fungi (black curve), and after the deposition of fungi: $N = 50$ (red curve), $N = 100$ (blue curve), $N = 150$ (cyan curve), $N = 200$ (pink curve) and $N = 250$ (purple curve).

Figure 3.6 shows the frequency-shift of the resonance dependence with the fungi concentration (number of spheres) and the obtained sensitivity and FoM. By looking at figure 3.6 (a), it can be seen that the frequency of the stop-band resonance experiences a redshift as we increase the fungi concentration. A minimum frequency shift of $\approx 5\text{GHz}$ and a maximum of $\approx 32\text{GHz}$, that corresponds with a variation of 0.6 % and 4% of the resonance frequency, can be observed for $N = 50$ and $N = 250$ respectively. From this frequency shift, we obtain the sensitivity that varies between 0.008 and 0.022. Regarding the FoM, it barely reaches a value of 2.2×10^{-4} , see figure 3.6 (inset).

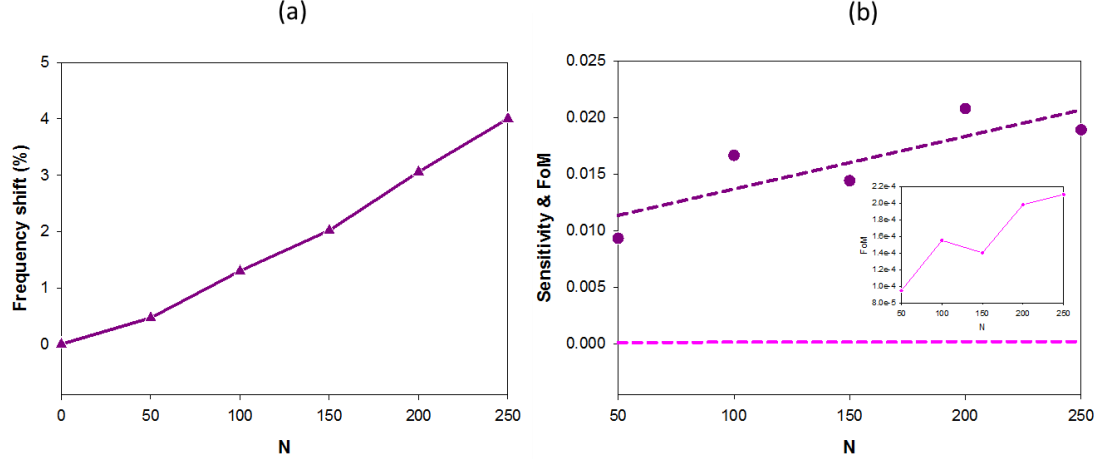


FIG. 3.6. (a) Frequency shift of the stop-band resonance vs. the variation of the fungi concentration. (b) Sensitivity: markers correspond to the calculated values, whereas dashed purple curve is the regression line; FoM (dashed pink curve).

As we can see, these are not very encouraging values, even having selected only a representative simulation for each case as it has been said before. With these results, a question raises: What would happen if all the spheres would fall in the right place? As we can see in figure 3.1, this cross-dipole has a narrow inner gap where a high electric field is confined at resonance. The frequency shift depends on the capacitance added by the gap between the metallic strips. To check this, two more simulations have been carried out.

Firstly, the horizontal slot between the metallic strips was filled with fungi, and the structure was excited with both vertical and horizontal polarizations. In the case of vertical polarization, a large interaction occurs between the vertical electric field and fungi and, therefore, a large frequency displacement is observed in the resonance. Specifically, as it can be seen in figure 3.7, the displacement is 30 GHz. On the other hand, the displacement under horizontal polarization is lower (20 GHz), since in this case, the interaction of the horizontal electric field with the spheres is smaller.

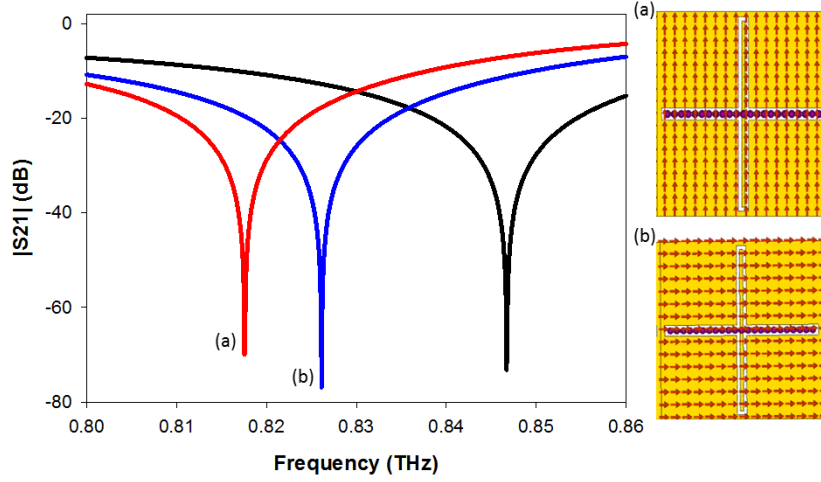


FIG. 3.7. Transmission coefficient and electric fields distribution for vertical polarization (red solid line) and horizontal polarization (blue solid curve); and comparison with the empty structure, without fungi (black solid curve).

This can be explained by the surface currents absolute magnitude that are represented in figure 3.8. With vertical polarization, the surface current is more intense in the horizontal arm (where spheres are located) than in the vertical one. Therefore, the electric field absolute magnitude is also more intense in that case, leading to a greater interaction with the spheres and hence a larger frequency shift in the case of vertical polarization, in agreement with the results of figure 3.7.

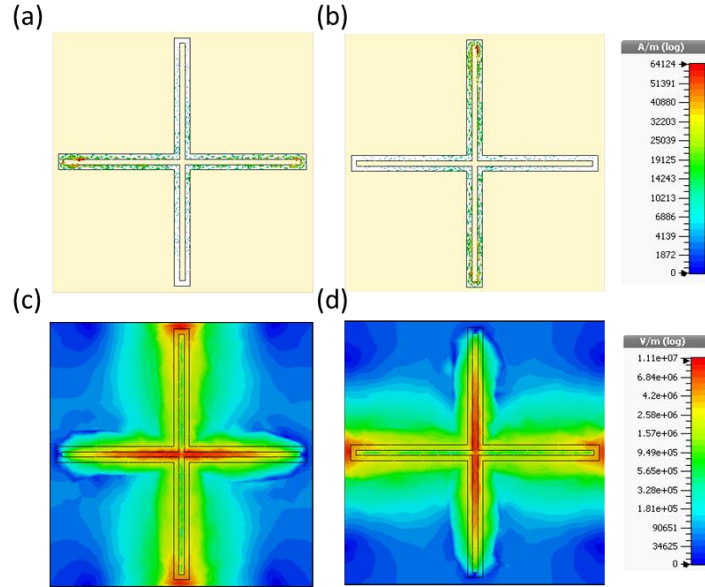


FIG. 3.8. (a) Surface currents for vertical polarization: absolute magnitude. (b) The same as (a) for horizontal polarization. (c) Electric field for vertical polarization: absolute magnitude. (d) The same as (c) for horizontal polarization.

In a second study, the vertical slot between the metallic strips was also filled with fungi. With this new arrangement, we should expect larger frequency shifts than the previous case, since now the interaction of the spheres with the electric field should be higher. Indeed,

with this configuration, the frequency resonance experiments a displacement of 40 GHz with respect to the structure without fungi (33% more than the previous case), as shown in figure 3.9. We can also note that, in this case, both vertical and horizontal polarization frequency resonances fall at the same frequency. This is what we expected, because of the symmetry of the structure.

This displacement of 40 GHz mentioned in the last paragraph, corresponds with a relative frequency shift of 3.7%, greater than the frequency shift in the case of $N = 250$ (relative shift of 3.76%); but in this case we only have 45 fungi, so it is a case comparable with the one of $N = 50$. So we are talking about a difference of 40 GHz versus 4 GHz or, in relative magnitude, a displacement of almost 5% versus another of 0.4%. This fact shows, again, that is not so important the number of spheres present in the structure, but its location. However, it is true that the more spheres we have in the unit cell, the greater probability that fall in areas of interest.

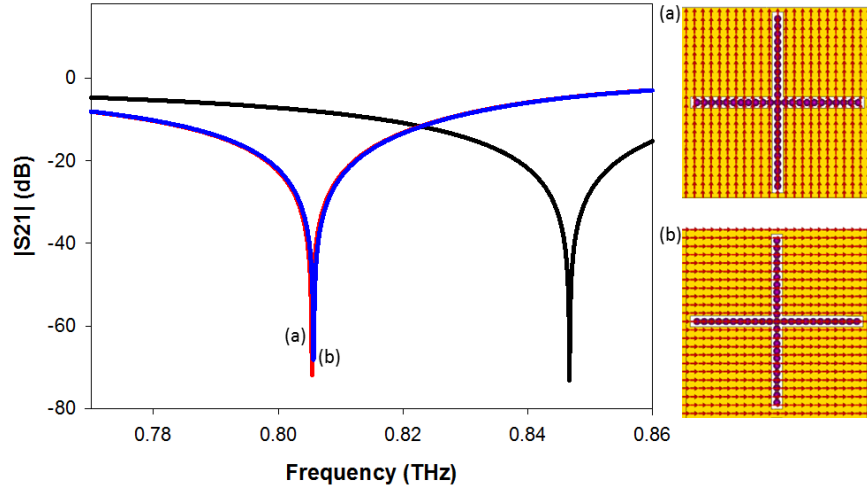


FIG. 3.9. Transmission coefficient and electric fields for vertical polarization (red solid line) and horizontal polarization (blue solid curve); and comparison with the empty structure, without fungi (black solid curve).

3.1.2. Complementary (slot) structure (BPF)

In this section the complementary structure of the cross-dipole, namely the slot cross-dipole, is analyzed. This new structure also lays on a polypropylene substrate and has the same dimensions as the previous one. The only difference is that now we are depositing a thin film conductive material over the substrate, on which a cross shaped slot is carved. Given that now we have a slot-type FSS, the frequency response must have band-pass instead of stop-band characteristic. This is corroborated in figure 3.10, where the transmission of an infinite FSS without any fungi is plotted. As observed, the structure presents a clear pass-band centered at $f_R = 810$ GHz.

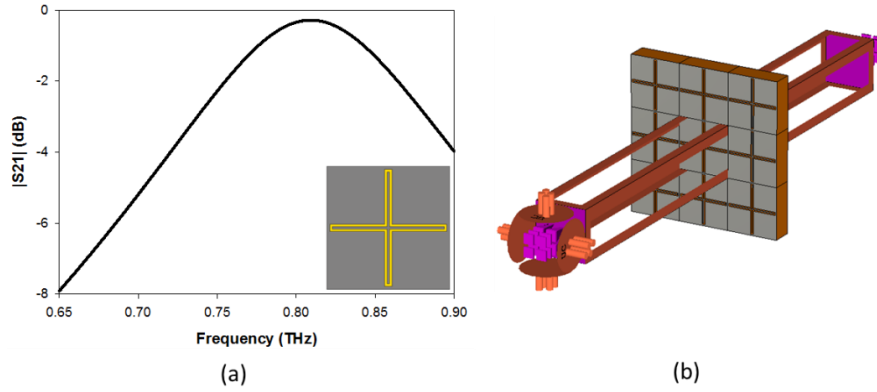


FIG. 3.10. Transmission of the slot cross-dipole without fungi

We performed the same study as before, depositing different concentrations of fungi and obtaining the response, see figure 3.11. At first sight, the results are very similar to the patch structure. Hence, only three scenarios were evaluated, namely $N = 50$, $N = 150$, and $N = 250$. Again, 10 simulations were done for each instance. As the intermediate cases have been eliminated ($N = 100$ and $N = 200$), the overlap disappears (See figure 3.11). The rest of the simulations results can be seen in table 3.2.

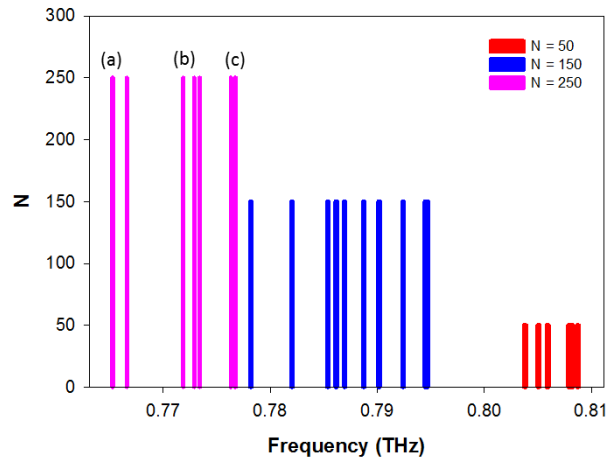


FIG. 3.11. Representation of the frequency resonance for all the simulations carried out for each fungi concentration.

| N | Frequency resonance for different simulations (GHz) | | | | | | | | | | Average(GHz) | Variance |
|-----|---|-------|-------|-------|-------|-------|-------|-------|-------|-------|--------------|----------|
| 0 | | | | | | | | | | | 810 | |
| 50 | 805,1 | 808,2 | 803,8 | 808,2 | 807,9 | 805,9 | 805,1 | 808,7 | 807,9 | 807,5 | 806.6 | 3.88 |
| 150 | 794,7 | 786,9 | 792,4 | 794,5 | 790,2 | 786,2 | 778,2 | 785,4 | 788,7 | 782,0 | 787.9 | 28.3 |
| 250 | 766,6 | 776,3 | 772,9 | 765,3 | 776,7 | 771,9 | 773,4 | 765,3 | 776,7 | 771,9 | 771.7 | 20.5 |

Table 3.2. Frequency resonance for all the simulations carried out for each fungi concentration, average and variance for each case.

If we now focus on the extreme cases, the highest interaction will also occur in areas where we have a capacitor. As we can observe in figure 3.12, in the simulation with highest

frequency variation 3.12(a) we have 40 fungi in the slot between the central cross and the ground plane, whereas only 28 fungi appear in the case of minimum frequency variation (about 30% decrease). If we look to the intermediate case at figure 3.12(b), it can be observed that the number of spheres within the strips is about 34 that, again, corresponds with an average between both cases.

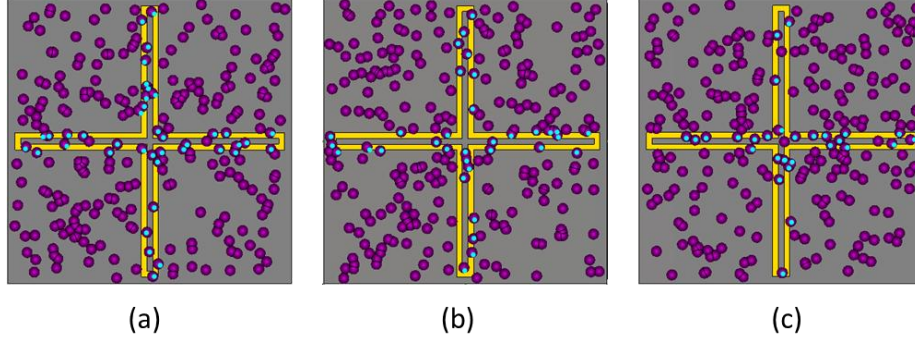


FIG. 3.12. Distribution of spheres on simulations corresponding to the edges of the case $N=250$. (a) Highest frequency variation (resonance at 765 GHz). (b) Intermediate case (resonance at 771 GHz). (c) Lowest frequency variation (resonance at 776 GHz).

As before, the simulations with a peak closest to the average were chosen for each case. The results are represented in figure 3.13.

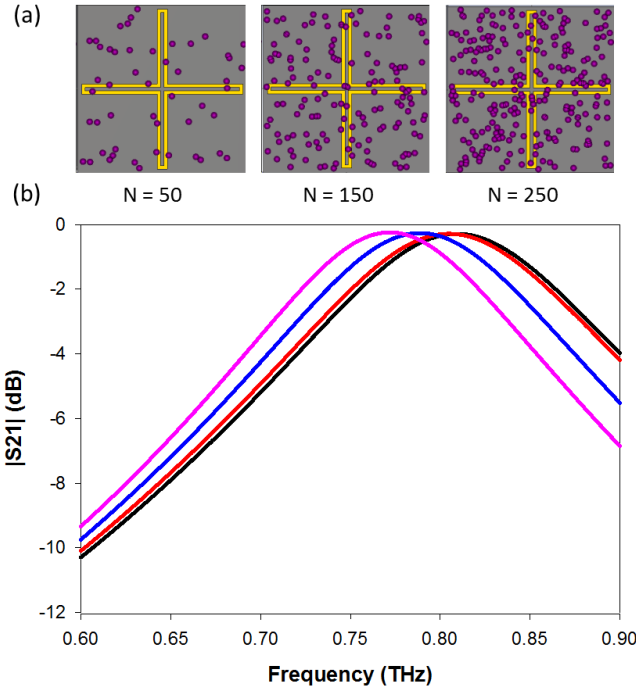


FIG. 3.13. (a) Front view of the structure with $N = 50$, $N = 150$, and $N = 250$ fungi (purple spheres). (b) Results of simulated transmission without fungi (black curve), and after the deposition of fungi: $N = 50$ (red curve), $N = 150$ (blue curve) and $N = 250$ (pink curve).

In this case, a redshift also appears in the spectrum, with a minimum frequency shift of ≈ 6 GHz (with $N = 50$) and a maximum shift of ≈ 40 GHz (with $N = 250$), that corresponds with a 5% frequency shift. This is also presented in figure 3.14, along with the sensitivity and FoM. In

this case, the structure has a sensitivity that varies between 0.011 and 0.023. Regarding the FoM, it reaches a maximum value of 1.44×10^{-4} . If we compare these values with the ones in the previous structure, we realize that the sensitivity is enhanced around 4.5%. Nevertheless, in this case the FoM has decreased its value by around 40%, so we still have not very encouraging values.

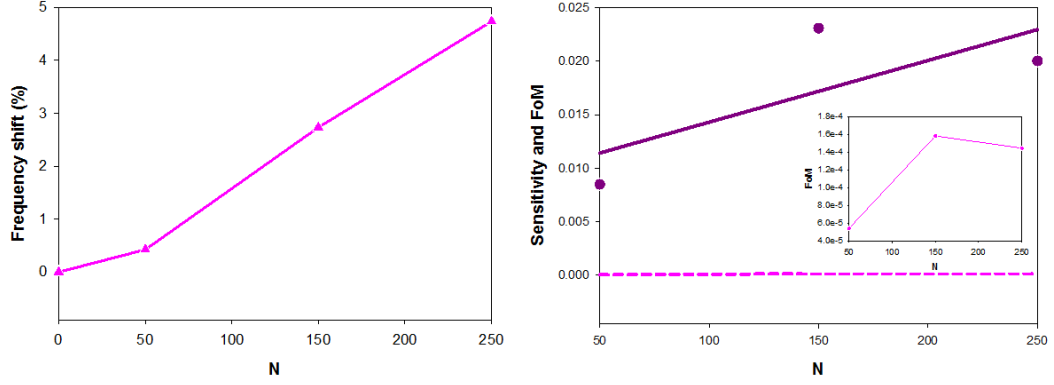


FIG. 3.14. (a) Frequency shift of the stop-band resonance vs. the variation of the fungi concentration. (b) Sensitivity: markers correspond to the calculated values, whereas dashed purple curve is the regression line; FoM (dashed pink curve).

As before, we found the response when fungi were placed in the zone with high electric field is enclosed. As mentioned above, this is the slot between the central cross and the ground plane. First, we filled the horizontal arm of the dipole and observed its behavior. This is depicted in figure 3.15.

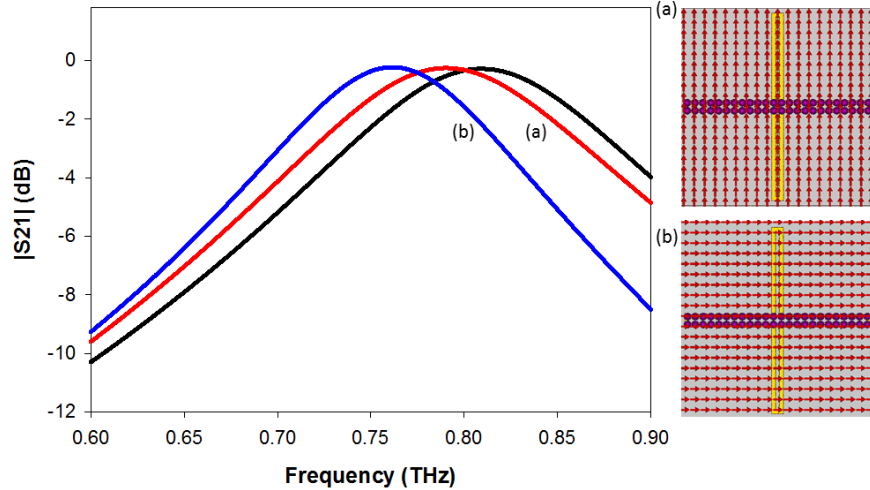


FIG. 3.15. Transmission coefficient and electric fields for vertical polarization (red solid line) and horizontal polarization (blue solid curve); and comparison with the empty structure, without fungi (black solid curve).

In this case, the vertical polarization has a smaller shift (20 GHz) than the horizontal polarization (52 GHz), contrary to what happened in the previous structure. This can be explained by attending to the surface currents that are represented in figure 3.16. As we can see, the surface current in the horizontal arm of the dipole where the fungi have been placed (figure 3.16(b)), is more intense for the horizontal than for the vertical polarization (figure 3.16(a)). Therefore, the electric field (see figure 3.16(c,d)) is also more intense in the former case, leading to an enhanced interaction with the spheres and hence a larger frequency shift.

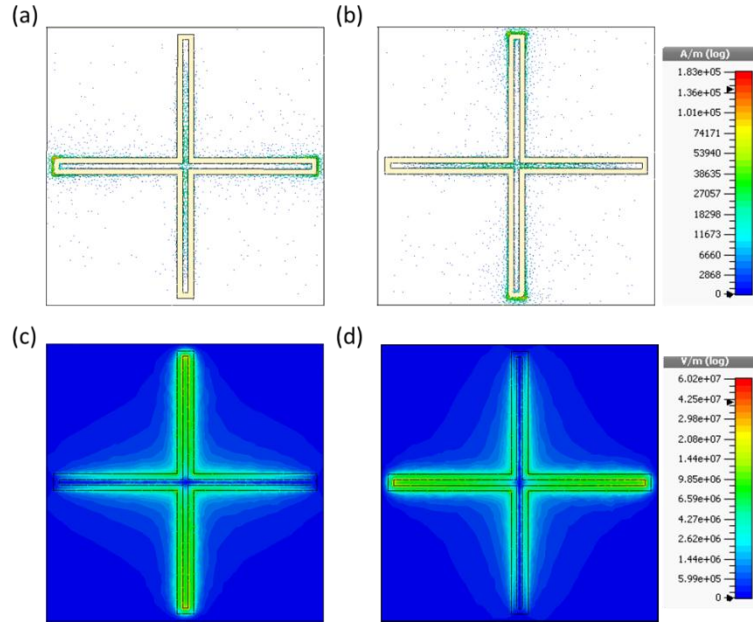


FIG. 3.16. (a) Surface currents for vertical polarization: absolute magnitude. (b) The same as (a) for horizontal polarization. (c) Electric field for vertical polarization: absolute magnitude. (d) The same as (c) for horizontal polarization.

Next, we filled completely the slot with fungi. In this case, we expect a larger displacement of the frequency maximum, because the interaction with fungi and electric field should be higher. Now, we can observe in figure 3.17 that the frequency shift is about 65 GHz, 25% more than the previous case and also larger than the one observed in the best case of the patch structure (65 GHz vs. 40 GHz). Again, both vertical and horizontal polarizations frequency resonances fall at the same frequency. As before, this is a direct consequence of the symmetry of the structure.

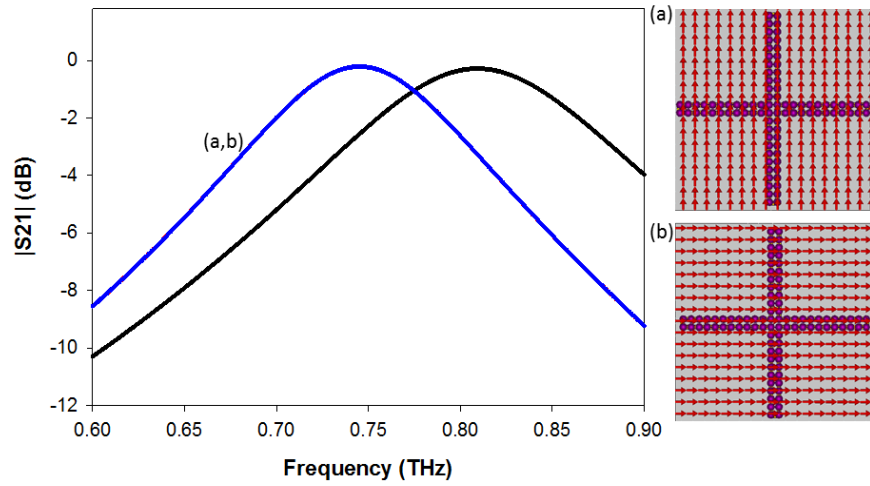


FIG. 3.17. Transmission and electric fields for vertical polarization (red solid line) and horizontal polarization (blue solid curve); and comparison with the empty structure, without fungi (black solid curve).

Finally, a comparison between both structures is done in table 3.3.

| | | Patch structure | Slot structure |
|-----------------------|----------------|---------------------|---------------------|
| N = 0 | Resonance | 832 GHz | 810 GHz |
| N = 50 | Resonance | 828.5 GHz | 806.6 GHz |
| | Δf (%) | 0.42 | 0.42 |
| N = 150 | Resonance | 815.6 GHz | 787.9 GHz |
| | Δf (%) | 1.97 | 2.72 |
| N = 250 | Resonance | 800.7 GHz | 771.7 GHz |
| | Δf (%) | 3.76 | 4.73 |
| Sensitivity (máx) | | $2.2 \cdot 10^{-2}$ | $2.3 \cdot 10^{-2}$ |
| Figure of Merit (máx) | | $2.4 \cdot 10^{-4}$ | $1.4 \cdot 10^{-4}$ |

Table 3.3. Comparison between patch structure and slot structure

Although the patch structure shows better performance than the slot one in terms of FoM, both present low values of sensitivity and FoM. However, it is true that the quantity of analyte (in this case, fungi) deposited on the unit cell is also very small, so in proportion, these are quite good values. Anyway, other structures with better results will be studied in the following sections, intended both for thin-film and microorganism sensing.

3.2. Hole Array

In this section another periodic structure based on a subwavelength hole array is evaluated. This hole array structure has been intensively studied in the last fifteen years in the context of extraordinary transmission phenomenon [22]. The objective of this study is to verify the behavior of this hole array as a thin film sensor, refractometer and, last but not least, to assess its performance as a fungi detector.

The schematic and dimensions of the unit cell structure are shown in figure 3.18(a). It consists of an aluminum (lossy metal) thin film of $0.3 \mu\text{m}$ thickness and electric conductivity, $\sigma_{Al} = 1.5 \times 10^7 \text{ S/m}$, on which a hole slot of diameter $\varnothing = 105 \mu\text{m}$ is etched, periodically repeated with periods $d_x = 52.5 \mu\text{m}$, $d_y = 350 \mu\text{m}$ on top of a thin polypropylene (PP) layer of thickness $75 \mu\text{m}$ and permittivity $\epsilon_{pp} = 2.25$.

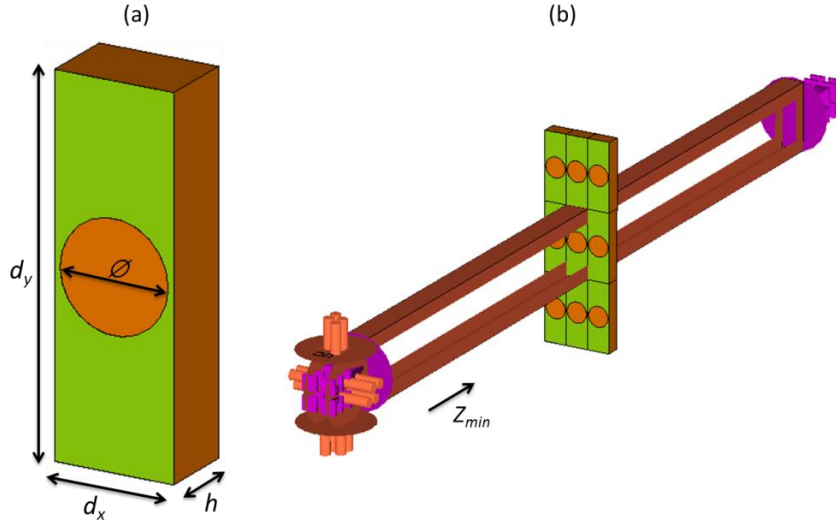


FIG. 3.18.(a) Schematic of the unit cell. Dimensions: polypropylene substrate height, $h = 75 \mu\text{m}$; unit cell vertical period, $d_y = 350 \mu\text{m}$; unit cell horizontal period, $d_x = 52.5 \mu\text{m}$; aluminum thickness, $h_{Al} = 0.3 \mu\text{m}$ hole diameter, $\varnothing = 105 \mu\text{m}$. Dielectric properties of the substrate: PP permittivity, $\epsilon_{pp} = 2.25$. Electric properties of the metallic film: Aluminum electric conductivity, $\sigma_{Al} = 1.5 \times 10^7 \text{ S/m}$. (b) Boundary conditions of the unit cell.

Figure 3.19 shows the transmission in dB of the hole array without the presence of analyte. As we can observe, the structure presents a peak of transmission followed by a null of transmission in both, regular ET and anomalous ET. In the regular ET, we have two peaks, at 647 GHz and at 844 GHz, and two nulls, at 718 GHz and at 857 GHz. If we calculate the frequency of this nulls of transmission, the first should be around 672 GHz ($f = c/d_y \sqrt{\epsilon_{eff}}$, where ϵ_{eff} can be calculated as the arithmetic mean of ϵ_{air} and ϵ_{pp}). As we can realize, the simulated value differs from this theoretical value, because we are not taking into account the substrate thickness. The second null corresponds with the Wood's anomaly, situated at Wood's frequency ($f_{Wood} = c/d_y$). As mentioned before, in this case $d_y = 350 \mu\text{m}$, so $f_{Wood} = 857 \text{ GHz}$, as expected. With the characteristics and dimensions mentioned in figure 3.18, the F factor explained in the Introduction chapter is: $F = \frac{75 \cdot \sqrt{2.25-1}}{350} = 0.24$

Although this value of F is below the condition to properly speak of anomalous ET ($F < 0.25$) it is close enough so that it gives rise to a clear resonance in the spectrum in which we have only a peak at 849 GHz, and a null at 857 GHz (at f_{Wood}). For the following studies, we are going to focus on the frequency shift of the peaks on both transmissions.

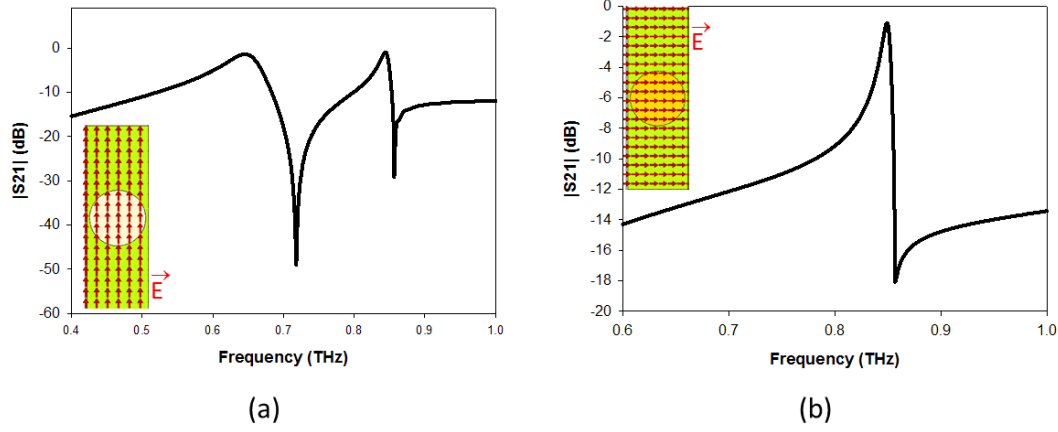


FIG. 3.19 (a) Results of simulated regular ET without analyte. Inset: electric field polarization. (b) Results of simulated anomalous ET without analyte. Inset: electric field polarization.

Now, the performance as a thin film sensor is evaluated. To achieve this, several simulations have been carried out depositing an analyte with different thickness each time, to check if we are able to find some parameter that allows us to discriminate between different thicknesses deposited in the structure. The analyte has been deposited in the back face (opposite to the aluminum film), for two main reasons. The first, increasing the substrate thickness accentuates the appearance and frequency movement of the anomalous ET. Furthermore, by sensing in the substrate side, we avoid damaging the metal in the process of depositing and removing the analyte. The analyte has a permittivity of $\epsilon_{\text{Analyte}} = 2.855$ and we are going to vary its thickness between $h_a = 0$ and $50 \mu\text{m}$ with a step of $5 \mu\text{m}$. The simulations characteristics are the same as in the cross dipole: Unit Cell boundary conditions in x and y axes, and Open + Add Space (i.e. perfectly matched layers) in z axis, taking the excitation from Z_{max} . The structure was simulated in the frequency span from 400 GHz to 1000 GHz. The transmission for each analyte thickness can be observed in figure 3.19.

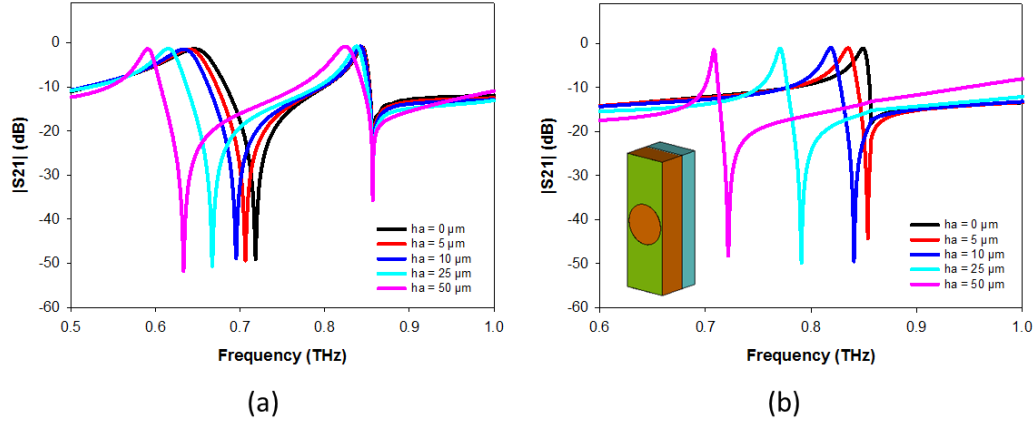


FIG. 3.20.(a) Results of simulated regular ET without analyte (black curve), with $h_a = 5 \mu\text{m}$ (red curve), $h_a = 10 \mu\text{m}$ (blue curve), $h_a = 25 \mu\text{m}$ (cyan curve), and $h_a = 50 \mu\text{m}$ (pink curve). (b) Results of simulated anomalous ET. Inset: perspective view of the case of $h_a = 50 \mu\text{m}$.

We can observe that both regular and anomalous ET peaks experience a frequency shift towards lower frequencies as we increase the analyte thickness. By looking at figure 3.21, for regular ET the minimum frequency shift is ≈ 7 GHz which corresponds with 1% frequency shift; and the maximum shift is 57 GHz (8% frequency shift). For anomalous ET the minimum shift is 14 GHz (1.6% frequency shift), and the maximum is 141 GHz, corresponding with almost 17%.

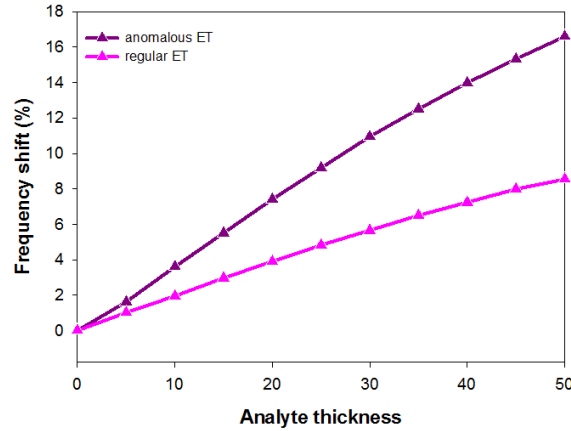


FIG. 3.21. Frequency shift of the peak vs. the analyte thickness for regular ET (pink curve), and anomalous ET (dark pink curve).

From the previous plot, we obtain the sensitivity that varies between 0.7 and 1.3 in the case of the regular ET, and between 2.1 and 3.3 in the case of the anomalous ET. As for the FoM, it varies in the range of 0.02 to 0.04 (regular ET) and 0.2 to 0.46 (anomalous ET), see figure 3.22. All these parameters are summarized in table 3.4.

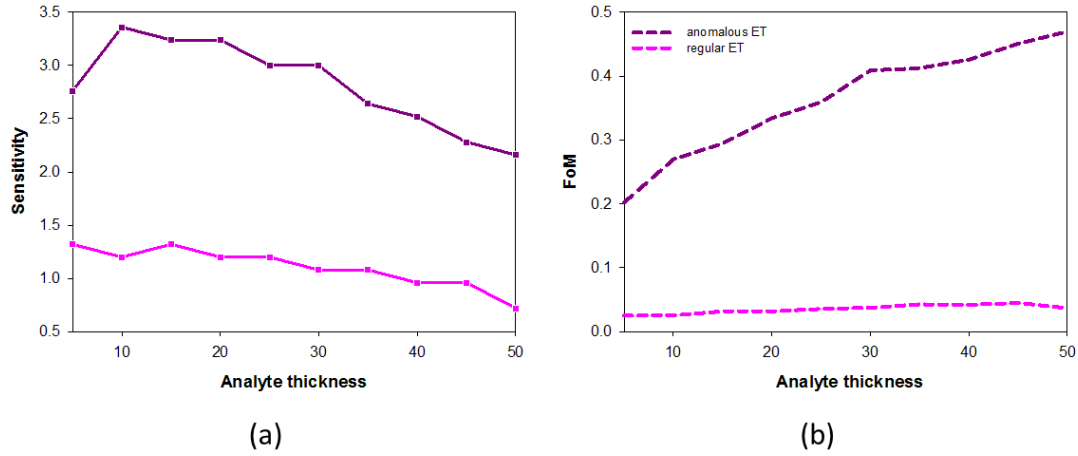


FIG. 3.22. (a) Sensitivity for the regular ET (pink curve) and anomalous ET (dark pink curve). (b) FoM for the regular ET (pink curve) and anomalous ET (dark pink curve).

| | | Regular ET | Anomalous ET |
|------------------------|----------------|------------|--------------|
| $h_a = 0 \mu\text{m}$ | Frequency peak | 646 GHz | 849 GHz |
| $h_a = 5 \mu\text{m}$ | Frequency peak | 639.4 GHz | 835.2 GHz |
| | Δf (%) | 1 | 1.6 |
| $h_a = 10 \mu\text{m}$ | Frequency peak | 633.4 GHz | 818.4 GHz |
| | Δf (%) | 1.9 | 3.6 |
| $h_a = 25 \mu\text{m}$ | Frequency peak | 614.8 GHz | 771 GHz |
| | Δf (%) | 4.8 | 9.2 |
| $h_a = 50 \mu\text{m}$ | Frequency peak | 590.8 GHz | 708 GHz |
| | Δf (%) | 8.5 | 16.6 |
| Sensitivity | | 0.7-1.3 | 2.1-3.3 |
| FoM | | 0.02-0.04 | 0.2-0.5 |

Table 3.4. . Behavior of a subwavelength hole array with different analyte thicknesses.

With these results it is clear that the values of sensitivity and FoM reached with the anomalous ET are quite better than the ones reached with the regular ET, and they are good enough to use it as a thin film sensor, as we achieve considerable frequency shift even for small thicknesses. This result makes sense, since as mentioned before, the anomalous ET depends strongly on the dielectric.

Next, the structure behavior as a refractometer is studied. More concretely, we want to test the capability of distinguishing between different materials with different permittivity and hence, different refractive index ($n = \sqrt{\epsilon}$). To accomplish it, this time we deposit an analyte with constant thickness, considering two cases $h_a = 10 \mu\text{m}$ and $20 \mu\text{m}$, and vary its refractive index from 1 to 2 with a step width of 0.2. The transmission for both regular ET (left) and anomalous ET (right) can be observed at figure 3.23. As it can be seen at first sight, when the analyte thickness increases, we achieve a larger frequency shift. Concretely, for the case of $h_a =$

10 μm we have a minimum frequency shift of 5 GHz and a maximum of 18 GHz for the regular ET, and a minimum of 6 GHz, maximum of 52 GHz for the anomalous ET; while for the case of $h_a = 20 \mu\text{m}$ we achieve a minimum and maximum of 10 GHz and 36 GHz for the regular ET, and a variation in the range between 13 GHz to 104 GHz for the anomalous, a considerable difference in comparison to the previous case.

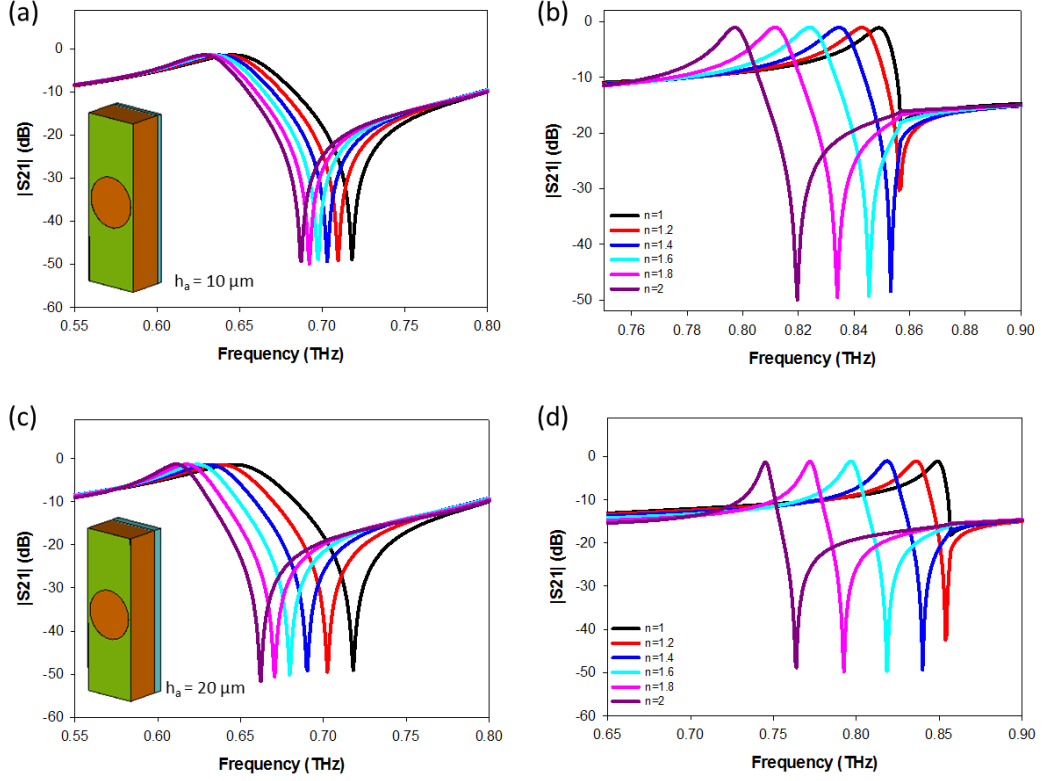


FIG. 3.23. (a) Regular ET for the prototype with analyte thickness $h_a = 10 \mu\text{m}$ at different refractive index values. (b) Anomalous ET for the prototype with analyte thickness $h_a = 10 \mu\text{m}$ at different refractive index values. (c) Same as (a) for $h_a = 20 \mu\text{m}$. (d) Same as (b) for $h_a = 20 \mu\text{m}$.

This difference of the frequency shift is plotted in figure 3.24. As mentioned before, there is a great difference between both analyte thicknesses, giving a variation from 6% in the case of anomalous ET and $h_a = 10 \mu\text{m}$ to 12% in the same case but with $h_a = 20 \mu\text{m}$; and from a maximum of almost 3% ($h_a = 10 \mu\text{m}$) to 5.4% ($h_a = 20 \mu\text{m}$) in the case of regular ET.

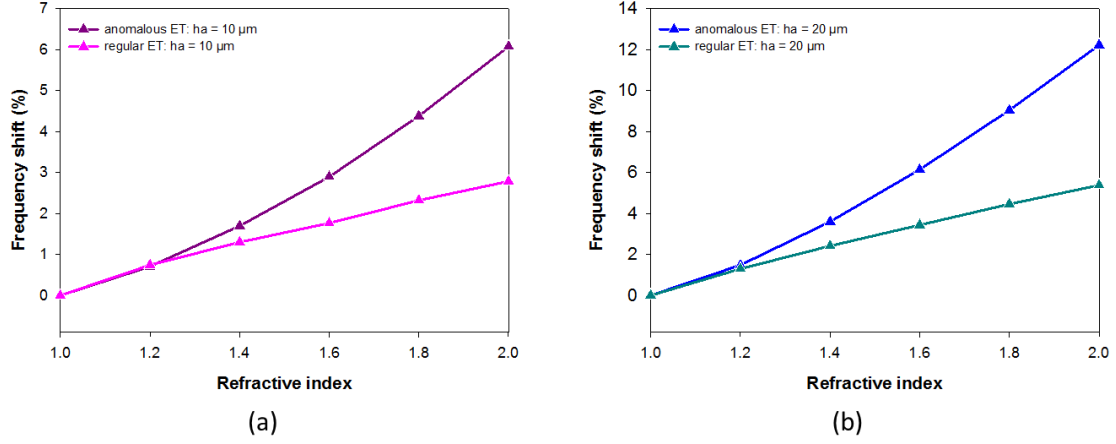


FIG. 3.24. (a) Frequency shift of the maximum of transmission vs. refractive index for regular ET (pink curve), and anomalous ET (dark pink curve) and $h_a = 10 \mu\text{m}$. (b) Same as (a) for regular ET (dark cyan curve), and anomalous ET (blue curve) for $h_a = 20 \mu\text{m}$.

From this frequency shift, we obtain the sensitivity that varies between 15 and 24 ($h_a = 10 \mu\text{m}$); and between 30 and 42 ($h_a = 20 \mu\text{m}$), for the regular ET; while the values improve substantially for anomalous ET case, with a variation from 30 to 72 ($h_a = 10 \mu\text{m}$) and 63 to 135 ($h_a = 20 \mu\text{m}$). Regarding the FoM, it registers very small values for the regular ET (almost 0), but takes much better values for the anomalous ET. Concretely, it reaches a value of 6 in the case of $h_a = 10 \mu\text{m}$; and a value of 20 in the case of $h_a = 20 \mu\text{m}$ (70% improvement), see figure 3.25.

With these values, the improvement obtained by increasing the analyte thickness on $10 \mu\text{m}$ is 43% for the regular ET resonance, and 47% for the anomalous ET case. A comparison between both analyte thicknesses can be seen in table 3.5.

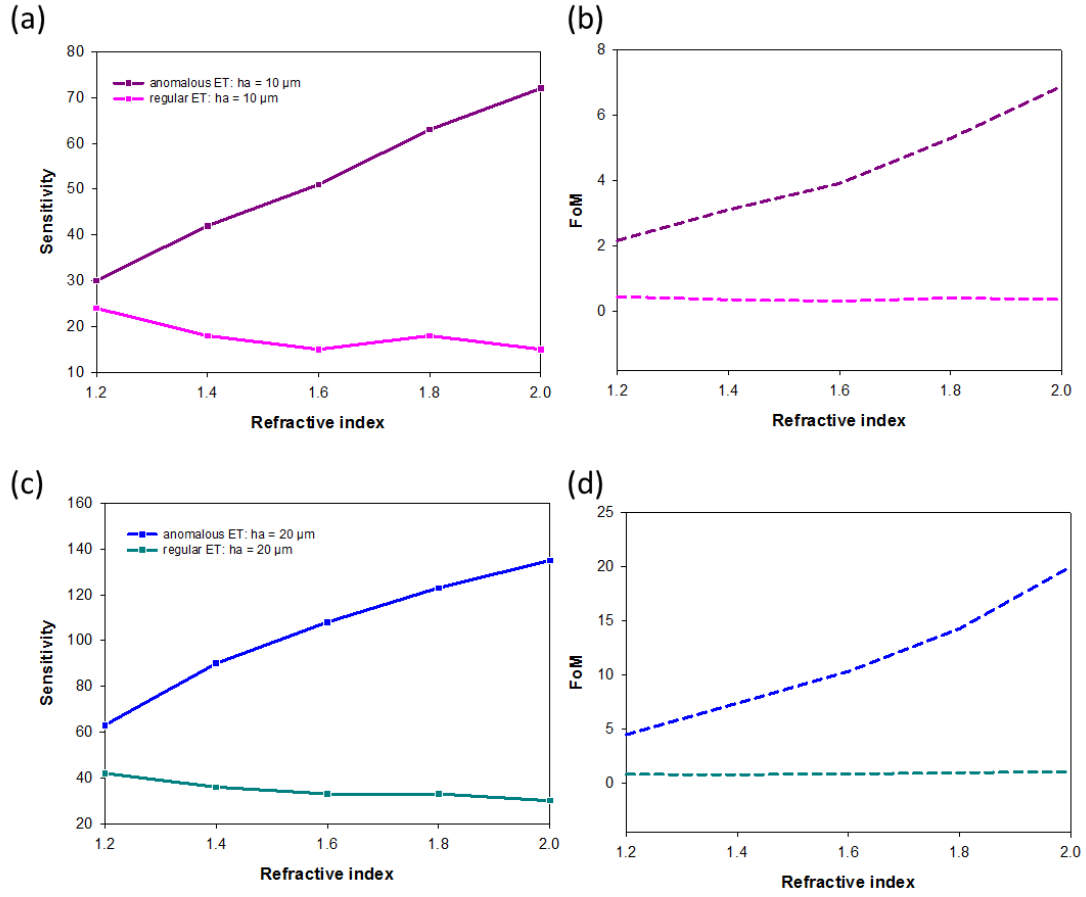


FIG. 3.25. (a) Sensitivity for anomalous and regular ET for $h_a = 10 \mu\text{m}$. (b) FoM for anomalous and regular ET for $h_a = 10 \mu\text{m}$. (c) Same as (a) for $h_a = 20 \mu\text{m}$. (d) Same as (b) for $h_a = 20 \mu\text{m}$.

| | | $h_a = 10 \mu\text{m}$ | | $h_a = 20 \mu\text{m}$ | |
|-------------|----------------|------------------------|--------------|------------------------|--------------|
| | | Regular ET | Anomalous ET | Regular ET | Anomalous ET |
| $n = 1$ | Frequency peak | 646 GHz | 849 GHz | 646 | 849 |
| $n = 1.2$ | Frequency peak | 641.2 GHz | 843 GHz | 637.6 GHz | 836.4 GHz |
| | Δf (%) | 0.7 | 0.7 | 1.3 | 1.5 |
| $n = 1.4$ | Frequency peak | 637.6 GHz | 834.6 GHz | 630.4 GHz | 818.4 GHz |
| | Δf (%) | 1.3 | 1.7 | 2.4 | 3.6 |
| $n = 1.6$ | Frequency peak | 634.6 GHz | 824.4 GHz | 623.8 GHz | 796.8 GHz |
| | Δf (%) | 1.8 | 2.9 | 3.4 | 6.1 |
| $n = 1.8$ | Frequency peak | 631 GHz | 811.8 GHz | 617.2 GHz | 772.2 GHz |
| | Δf (%) | 2.3 | 4.4 | 4.4 | 9 |
| $n = 2$ | Frequency peak | 628 GHz | 797.4 GHz | 611.2 GHz | 745.2 GHz |
| | Δf (%) | 2.8 | 6 | 5.4 | 12.2 |
| Sensitivity | | 15-24 | 30-72 | 30-42 | 63-135 |
| FoM | | 0.7-2.7 | 0.7-6 | 0.8-1 | 4.5-20 |

Table 3.5. Comparison between structures with different analyte thickness.

With this table we can conclude that the performance of the sensor improves for thick analytes. However, it must be taken into account that in general one of the main applications is the detection of thin films, so a good compromise solution must be found.

Finally, fungi with different concentrations have been deposited on the structure, in the aluminum side, with the aim to see if this type of hole arrays can act as a fungi detector. Fungi have been modelled as in the previous section: spheres with a radius of 2 μm and a permittivity $\epsilon_{\text{fungi}} = 8$. As in this time we have a bigger structure, we have decided to choose larger concentrations. Concretely, $N = 200$, $N = 400$, and $N = 600$ fungi. The results of these simulations can be seen in figure 3.26.

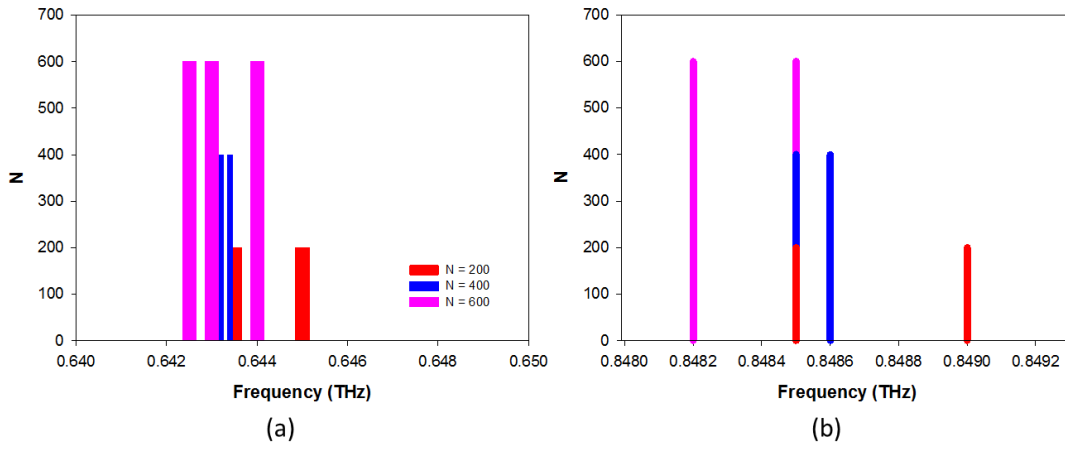


FIG. 3.26. (a) Representation of the frequency resonance for all the simulations carried out for $N = 200$ (red curve), $N = 400$ (blue curve), and $N = 600$ (pink curve) for regular ET. (b) The same as (a) for anomalous ET.

As shown in figure 3.26, it becomes impossible to distinguish between different concentrations, even though the number of spheres is very high. All the considered cases present a strong overlapping, with a very weak frequency shift. For these reasons, we did not perform any statistical study for hole arrays.

The results of one simulation for each case is plotted at figure 3.27. We can observe that the frequency shift is negligible in all cases. This can be due to the small size of the spheres in comparison with the structure and, in particular, with the hole. As we said in the cross-dipole study, the best place to place the spheres is in the regions of high electric field concentration. In a simple model, the hole of the array acts like a capacitor, so there is a high electric field in the hole. At the same time, surface currents are generated just around it at resonance. These currents are, indeed, in phase so this act as an inductance and give rise to an intense magnetic field. Joined together, this acts as an LC filter, with a shunt impedance equal to the parallel of both capacitance and inductance: $Z = \frac{j\omega L}{1 - \omega^2 LC}$. When the angular frequency, ω , is equal to the resonant angular frequency, $\omega_0 = \frac{1}{\sqrt{LC}}$, the impedance Z goes to infinite, and maximum transmission takes place; whereas when $\omega = 0$, $Z = 0$; and we have a null of transmission (pole).

A 3D plot of the calculated the electric field and surface currents at resonance is presented in figure 3.28.

A possible solution to this could be to rescale the diameter of the hole so that it is comparable to the size of the spheres. The problem is that, if we keep the rest of parameters unchanged, the quality factor of the structure would be extremely high. We would have an overly resonant structure, and if losses were considered, the transmission peak would disappear from the spectrum. Another possibility could be varying the frequency range. The problem with this, is that although we could scale the lateral periods, d_x and d_y , the dielectric width is non-scalable, and it would be too wide for the purpose of sensing.

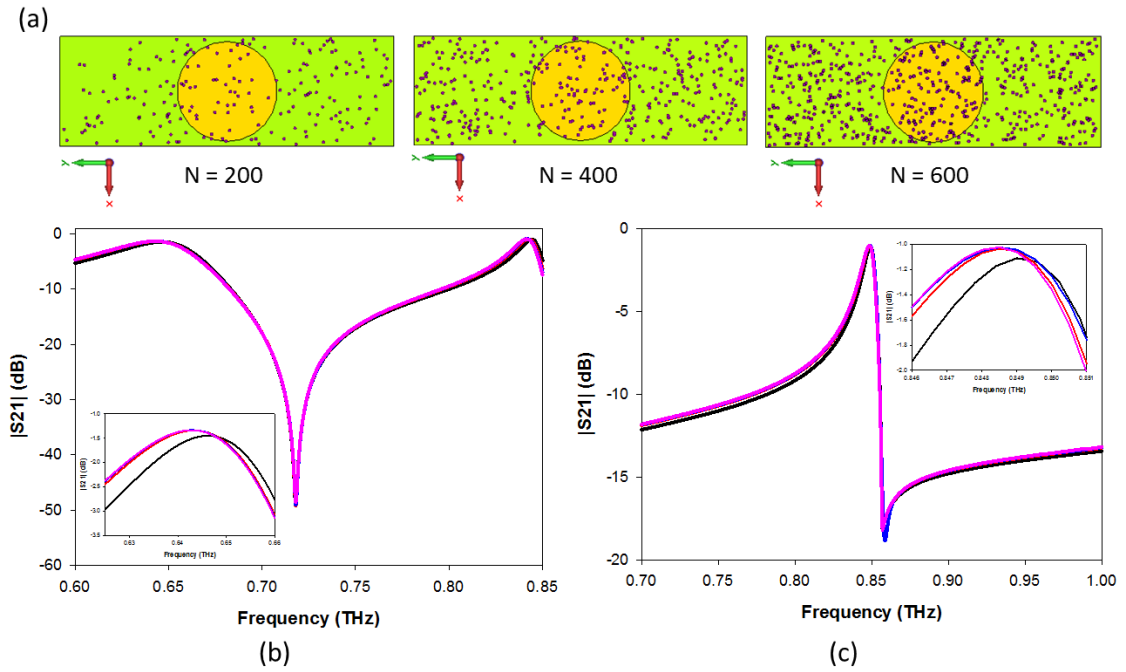


FIG. 3.27. (a) Front view of the structure for $N = 200$, $N = 400$, and $N = 600$ fungi. (b) Regular ET for $N = 0$ (black curve), $N = 200$ (red curve), $N = 400$ (blue curve), and $N = 600$ (pink curve). Inset: zoom of the maximum first peak of transmission. (c) Anomalous ET for $N = 0$ (black curve), $N = 200$ (red curve), $N = 400$ (blue curve), and $N = 600$ (pink curve). Inset: zoom of the maximum peak of transmission.

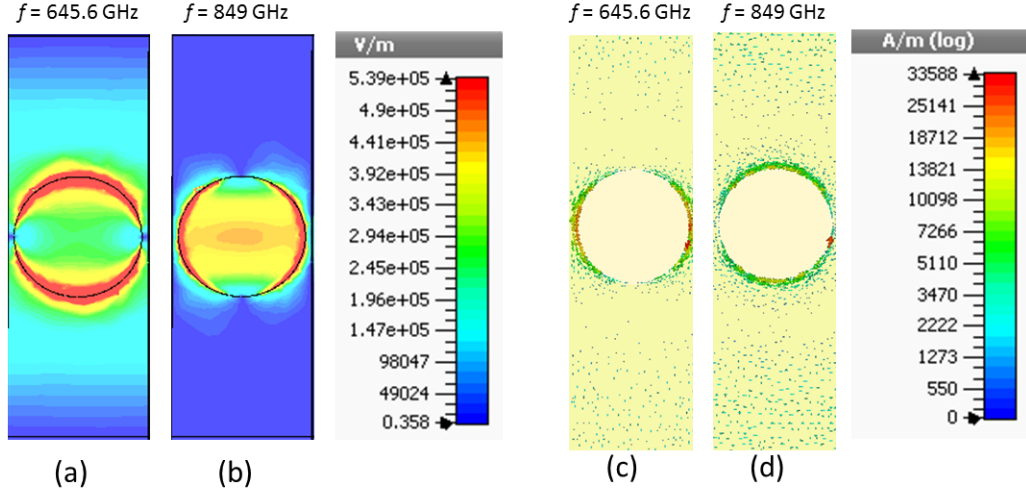


FIG. 3.28. (a) Absolute magnitude of the electric field for vertical polarization. (b) The same as (a) for horizontal polarization. (c) Surface currents for vertical polarization (absolute magnitude). (d) Same as (b) for horizontal polarization.

After doing this study, a last question was raised. In a structure in which the anomalous ET is about to appear, how much analyte thickness should we deposit for the anomalous ET to emerge in the spectrum?

A new structure with the same design parameters as those shown in figure 3.18(a), but with a different PP thickness, now equal to 55 μm instead of 75 μm , has been designed. By decreasing this substrate thickness, h , we manage to decrease the F factor, as it is directly dependent on h , as mentioned at the introduction. So, with this new parameters, the F factor is now: $F = \frac{55 \cdot \sqrt{2.25 - 1}}{350} = 0.17$. With this F (well below 0.25), a pole does not take place. This can be seen in figure 3.29, where the simulated empty structure is plotted. In these conditions a peak appears near the Wood's anomaly (857GHz), but a pole does not take place.

To evaluate the sensing performance, we have deposited the same analyte as before ($\epsilon_{\text{Analyte}} = 2.855$) varying its thickness between 0 and 30 μm , with a step width of 5 μm . A selection of the results of the simulated anomalous transmission are shown in figure 3.30.

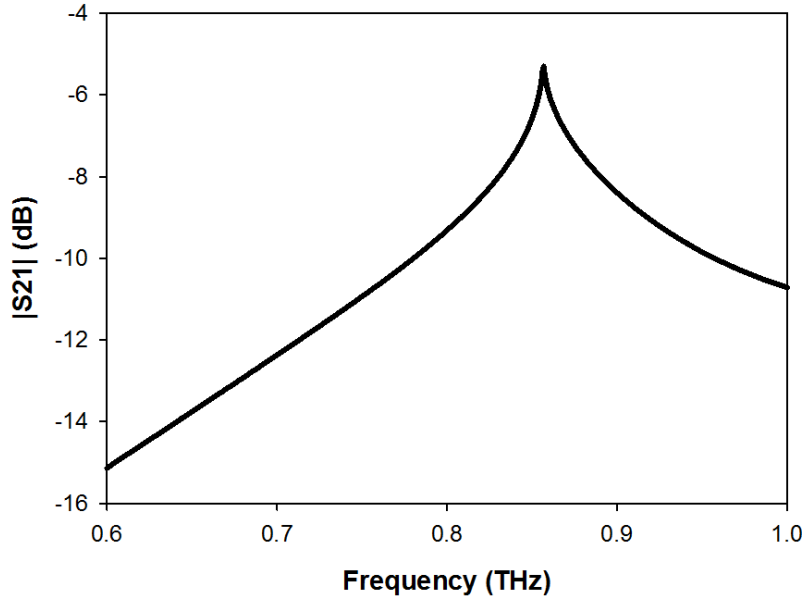


FIG. 3.29. Anomalous ET for the Hole Array with PP thickness, $h = 55 \mu\text{m}$, where only a peak, but not a pole is observed.

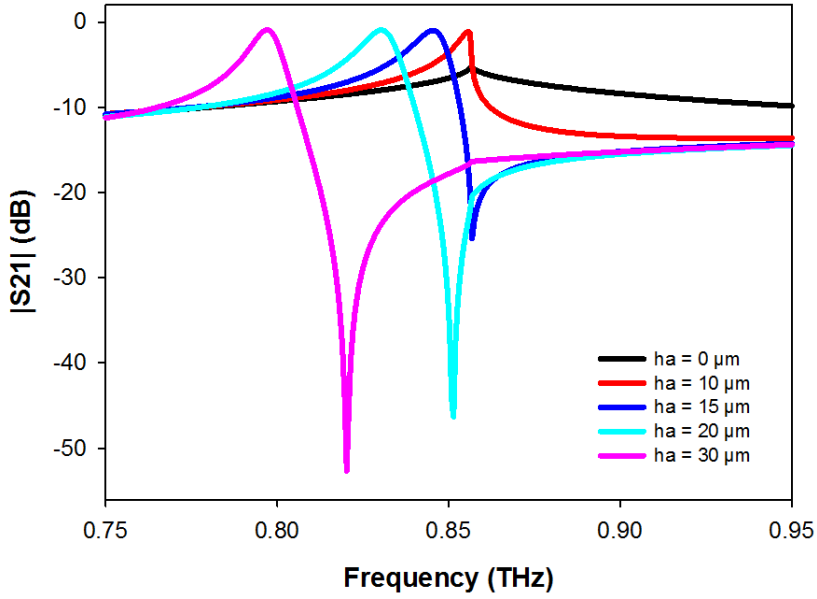


FIG. 3.30. Results of simulated anomalous ET without analyte (black curve), with $h_a = 10 \mu\text{m}$ (red curve), $h_a = 15 \mu\text{m}$ (blue curve), $h_a = 20 \mu\text{m}$ (cyan curve), and $h_a = 30 \mu\text{m}$ (pink curve).

We can appreciate that the analyte thickness needed to get a pole, is $h_a = 15 \mu\text{m}$. Another point of view can be fixing a frequency and observe the amplitude shift for each analyte thickness. If we plot this situation, fixing the frequency at f_{wood} , we get the curve that is shown at figure 3.31. Now, we are going to be able to sense until we have two equal values of

amplitude for two different thicknesses. We can observe that this occurs for a thickness of approximately $13\text{ }\mu\text{m}$.

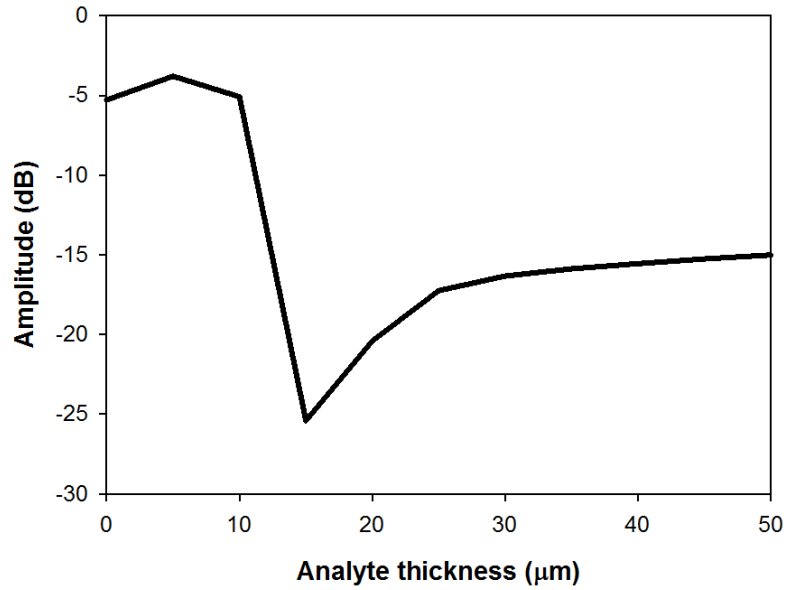


FIG. 3.31. Amplitude in dB of the structure versus analyte thickness.

With these results we can conclude that this structure is able to detect thicknesses larger than $15\text{ }\mu\text{m}$ if we focus on the frequency shift, and thicknesses below $13\text{ }\mu\text{m}$ if we focus on the amplitude shift; so there is only a little gap between $13\text{ }\mu\text{m}$ and $15\text{ }\mu\text{m}$ that cannot be distinguishable.

A further study is also made to compare the values with the ones achieved in the previous structure of $h = 75\text{ }\mu\text{m}$. First, the maximum peak frequency shift can be observed in figure 3.32.

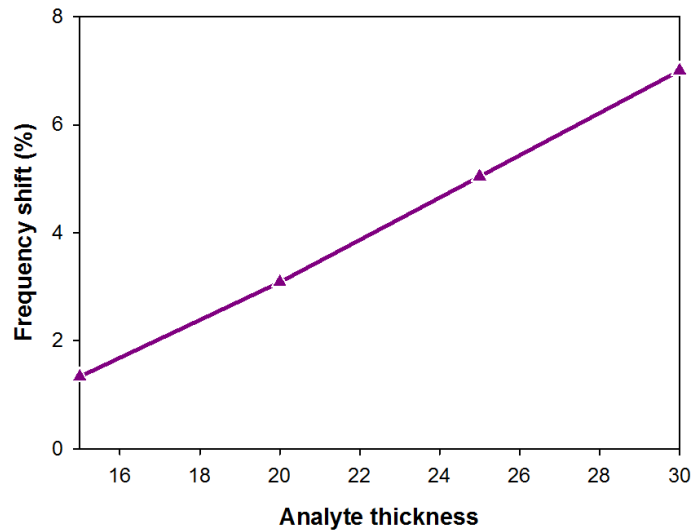


FIG. 3.32. Peak frequency shift of the structure versus analyte thickness.

Here, a maximum frequency shift of 7% is achieved for an analyte thickness of 30 μm , while in the last structure; we obtained a shift of 11% for the same thickness. For these values, we obtain the sensitivity that varies between 0.8 and 3.4, values similar to those obtained previously. Regarding the FoM, we are in the range between 0.05 and 0.3, somewhat lower than in the previous case, see figure 3.33.

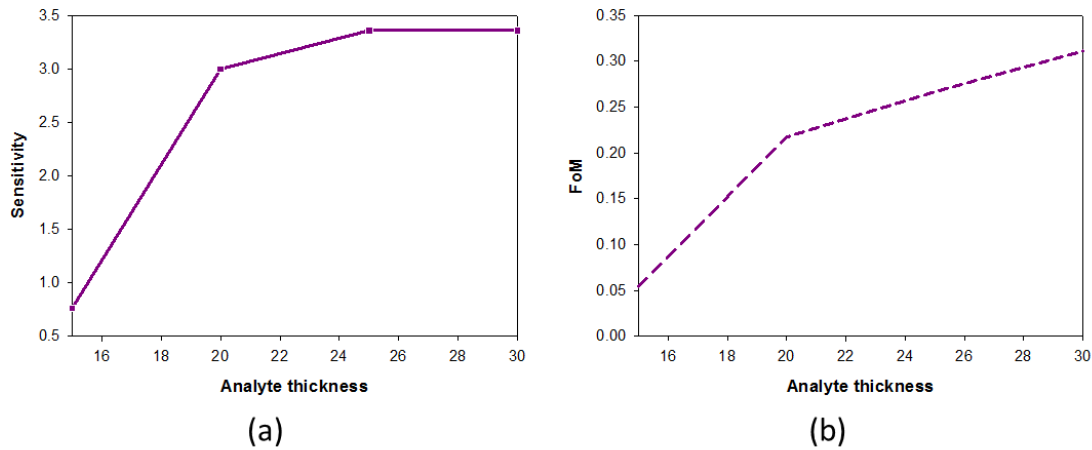


FIG. 3.33. (a) Sensitivity for the anomalous ET (solid curve). (b) FoM for the anomalous ET.

To finish this study, we analyze the relationship between the permittivity, ϵ , and the analyte thickness. What is expected is that with very tiny analyte thickness, we would be capable to detect materials with very high permittivity; whereas with thick enough analyte, we would be able to detect also a very small permittivity. For this, we have taken values of permittivity between 2.5 and 10, as most materials that may be interesting to detect meet at that range, and the analyte thickness, as before, between 0 μm and 30 μm . We have assumed as detectable those values of permittivity that present a peak followed by a pole (anomalous ET). Results of the simulation can be shown at figure 3.34.

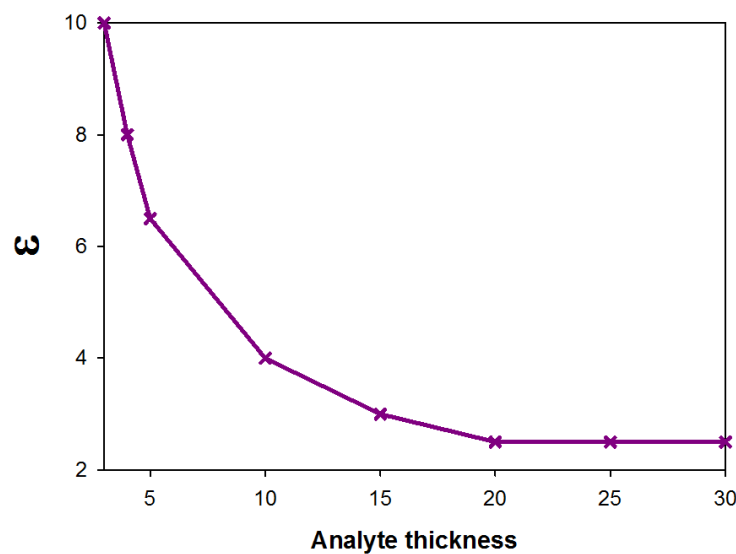


FIG. 3.34. Permittivity detectable vs. analyte thickness.

From this study we can conclude that for a thickness of $3\ \mu\text{m}$, we can detect materials with a permittivity of 10. If we increase the analyte thickness to 20, we can detect permittivities as small as 2.5. We have also represented the results of the transmission coefficient for some analyte thicknesses ($5\ \mu\text{m}$, $10\ \mu\text{m}$ and $20\ \mu\text{m}$) in contour plots that can be observed at figure 4.35, where we can see clearly how the frequency location of the peak at the anomalous transmission varies according to the permittivity in each case. Figure 3.35(a) shows the contour plot of a simulated analyte of thickness $3\ \mu\text{m}$. We can observe that the null of transmission (pole) frequency is almost unchanged as the permittivity grows. In figure 3.35(b) we can observe the contour plot of a simulated analyte of thickness $10\ \mu\text{m}$. In this case a frequency redshift of the pole is observed when the permittivity increases. Last, figure 3.35(c) shows the same contour for an analyte thickness of $20\ \mu\text{m}$. Here we can observe, besides the frequency redshift of the pole, another null of transmission at higher frequencies due to the substrate resonances.

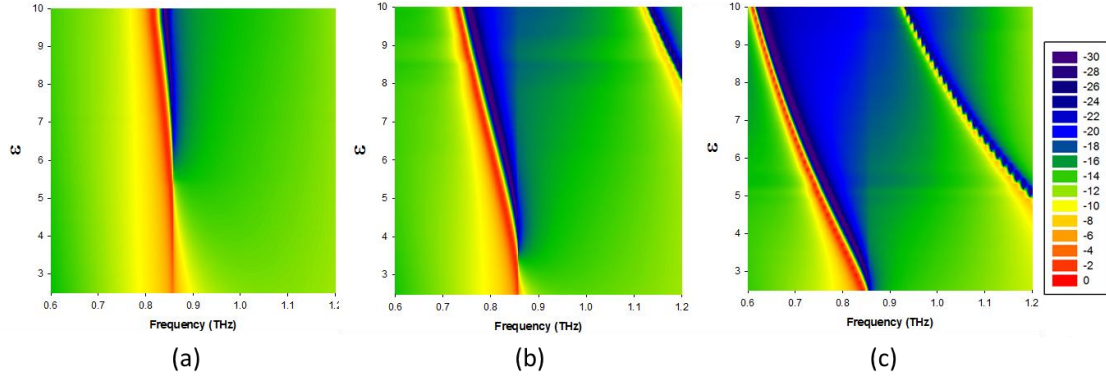


FIG. 3.35. Contour plot of the analyte permittivity versus frequency for different analyte thicknesses: (a) $h_a = 3\ \mu\text{m}$. (b) $h_a = 10\ \mu\text{m}$. (c) $h_a = 20\ \mu\text{m}$.

To sum up, we can say that this structure presents good performance as thin film sensor and as a refractometer, with very promising quality values. Regarding its use as a fungi detector, its performance is far from optimal, due to the large size difference between the hole and the spheres, as said before. Next, a different type of structure with promising results as fungi detector device will be studied.

3.3. Densely Packed Frequency Selective Surface

The last sensing platform considered in this work is based on the so-called Densely Packed Frequency Selective Surfaces (DPFSSs). We consider here two DPFSS, one capacitive and another inductive, and analyze two different configurations: without ground plane, in transmission; and with ground plane, where we evaluate the reflection. Our aim is to assess their behavior both as a refractometer and fungi detector.

3.3.1. Capacitive structure

The unit cell of this structure consists of a metallic patch of aluminum (lossy metal) thin film of $0.4 \mu\text{m}$ thickness and conductivity, $\sigma_{Al} = 3.56 \times 10^7 \text{ S/m}$, on top of a PP substrate of thickness $h_{pp} = 29 \mu\text{m}$, permittivity $\epsilon_{pp} = 2.25$, and lost tangent $\delta_{pp} = 0.001$. The schematic and boundary conditions of this structure can be shown at figure 3.36. We are going to study two cases, with different boundary conditions:

- With a ground plane: in this case, the ground plane thickness is $h_G = 1.2 \mu\text{m}$ and we study the reflection of the structure (S11 parameter).
- Without ground plane: we study the transmission of the structure (S21 parameter).

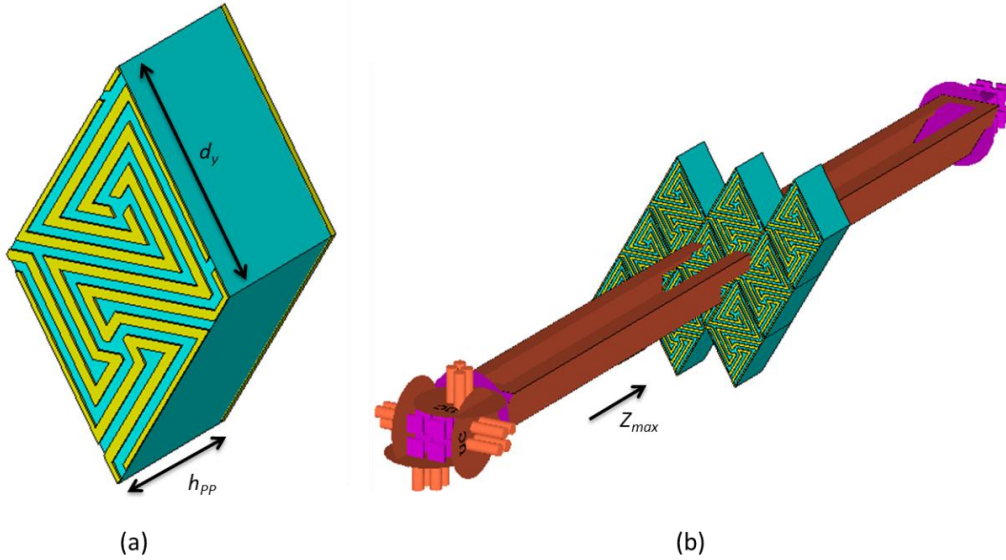


FIG. 3.36.(a) Schematic of the unit cell with a ground plane. Dimensions: polypropylene substrate height, $h_{pp} = 29 \mu\text{m}$; unit cell lateral period, $d_y = 36.4 \mu\text{m}$; aluminum thickness, $h_{Al} = 0.4$; ground plane thickness, $h_G = 1.2 \mu\text{m}$. Dielectric properties of the substrate: PP permittivity, $\epsilon_{pp} = 2.25$; lost tangent, $\delta_{pp} = 0.001$. Electric properties of the metallic film: Aluminum electric conductivity, $\sigma_{Al} = 3.56 \times 10^7 \text{ S/m}$. (b) Boundary conditions of the unit cell.

This is, as in the case of the cross-dipole, a patch-type structure, so it will behave as a notch filter at the resonance frequency. In the simulations only normal incidence is considered with orthogonal polarizations, vertical and horizontal; and the same simulation characteristics as before: Unit Cell boundary conditions in x and y axes, and Open + Add Space (i.e. perfectly matched layers) in z axis, taking the excitation from Z_{max} . The structure was simulated in the frequency span from 0 GHz to 600 GHz. The frequency response of both cases, transmission and reflection of the empty structure is shown at figure 3.37. As vertical and horizontal polarizations are almost identical, all the simulations are going to be under vertical polarization and normal incidence.

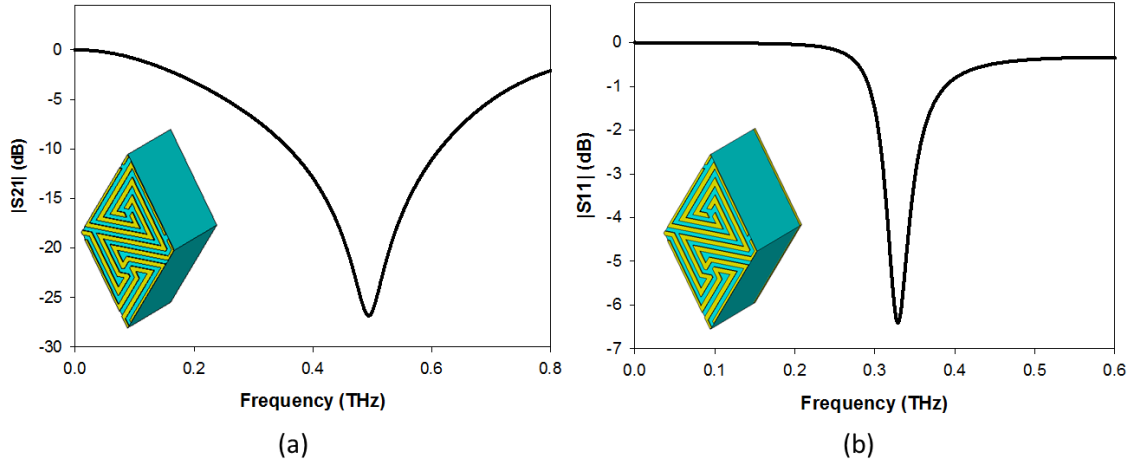


FIG. 3.37. (a) Results of simulated transmission of the structure without ground plane (b) Results of simulated reflection of the structure with ground plane.

It can be observed that the structure without ground plane presents a stop-band resonance at $f_{RT} = 496$ GHz in transmission, whereas the structure with ground plane has an reflection dip at $f_{RA} = 329$ GHz, where the reflection is around -6.5 dB and, obviously the transmission is null due to the presence of the ground plane. For simplicity, in this and the following studies we will show only transmission for the structure without ground plane and reflection for the structure with ground plane.

The behavior of the structure as a refractometer is now evaluated. With that aim in view, we deposit an analyte $3 \mu\text{m}$ thick and vary its refractive index from 1 to 2 with a step width of 0.2. The results of this simulation, both transmission (without ground plane) and reflection (with ground plane) are shown in figure 3.38.

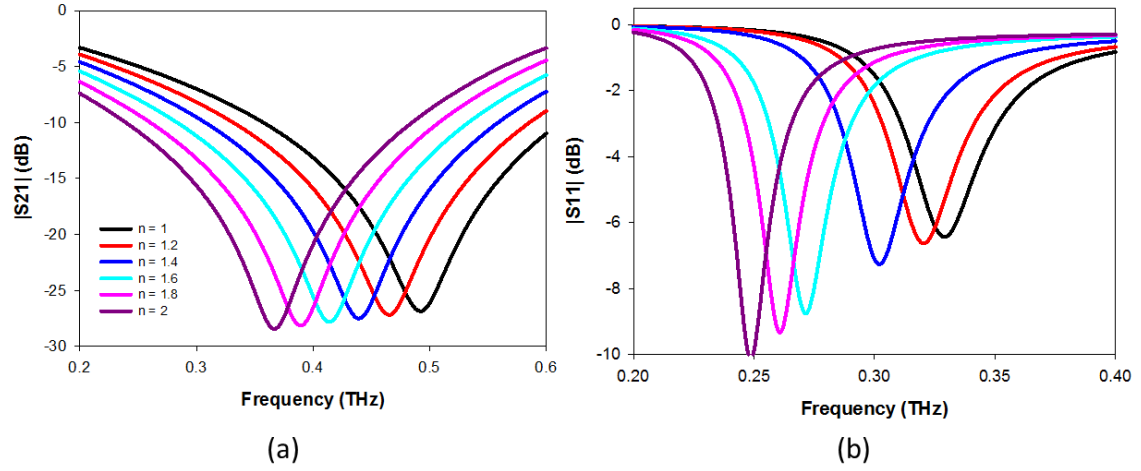


FIG. 3.38. (a) Transmission coefficient magnitude of the structure without ground plane , analyte thickness $h_a = 3 \mu\text{m}$ and different refractive index values. (b) Reflection coefficient magnitude of the structure with ground plane, analyte thickness $h_a = 3 \mu\text{m}$ and different refractive index values.

We can observe that the frequency shift is larger as we increase the refractive index. In particular for this structure, we have a minimum resonance frequency shift of 27 GHz in transmission and a shift of 8 GHz in reflection, which corresponds with relative shift values of 5.5% and 2.4% respectively. The maximum frequency shift that we obtain occurs in the case where $n = 2$, and have values of 125 GHz (25%) in transmission; and 80 GHz (24%) in reflection. We can see this frequency shift in figure 3.39.

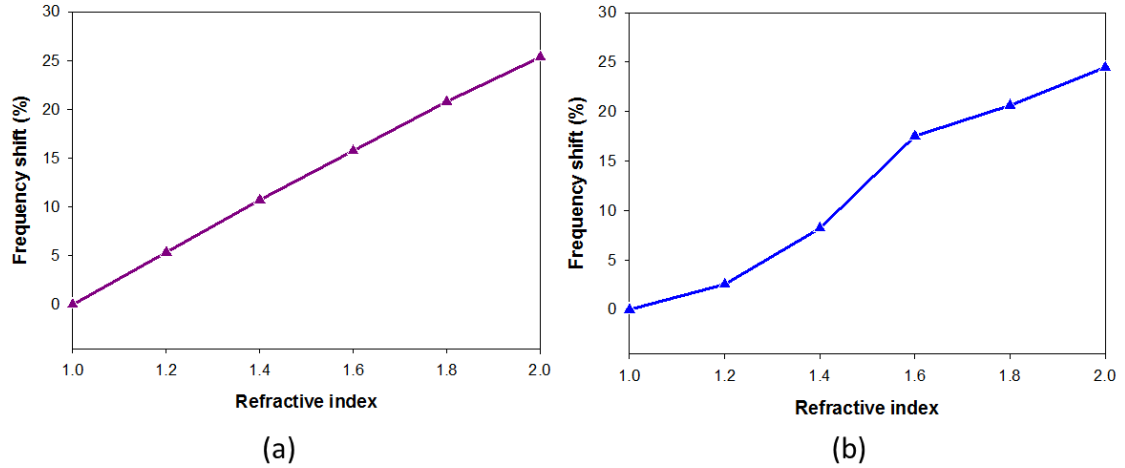


FIG. 3.39. (a) Resonance frequency shift vs. refractive index for $h_a = 3 \mu\text{m}$, transmission. (b) Same as (a), reflection configuration.

We can observe that the frequency shift achieved is pretty similar for both configurations, and all refractive index values, except the one with $n = 1.6$, where we achieve a larger frequency displacement (2% increase) in the reflection case. From these values of frequency shift, we obtain the sensitivity that varies between 112 and 132 in the case of

transmission; and between 42 and 153 in the case of reflection, see figure 3.40(a). Regarding the FoM, it reaches values between 0.22 and 0.24 in the transmission mode, whereas this number rises to the range from 1.1 to 4.5 in the reflection mode, see figure 3.40(b). This is due to the different width of the FWHM in both cases. As it can be seen in figure 3.38, it is much reduced in the second case (reflection). In any case, even the values for the transmission configuration are still reasonably good and similar to the structures previously studied, but with thinner analyte.

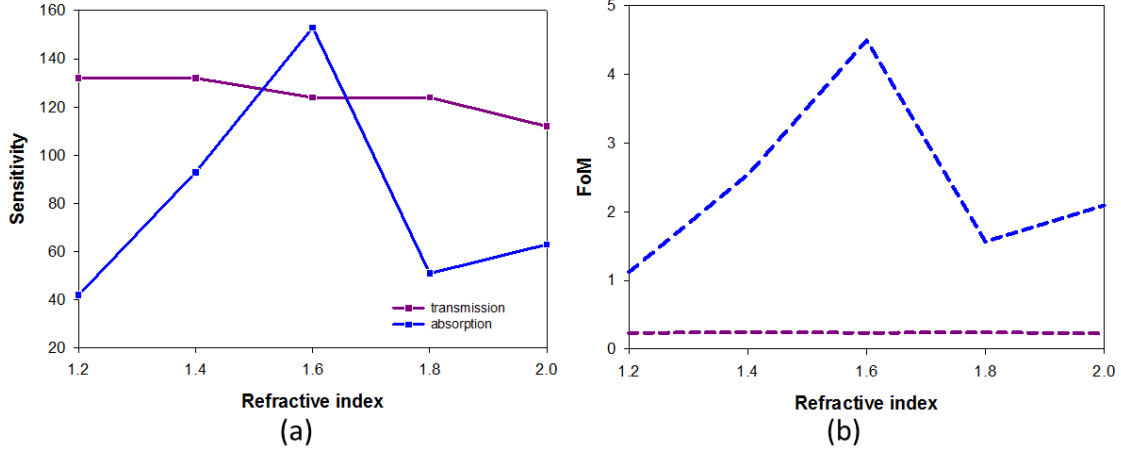


FIG. 3.40. (a) Sensitivity for transmission configuration (purple curve), and the same for reflection configuration (blue curve). (b) FoM for transmission configuration (purple curve), and the same for reflection configuration (blue curve).

As a next step in the study, now we are going to check the performance of this structure as a fungi detector. As we did in the cross-dipole, ten different simulations, first for the structure without ground plane and then for the ground plane configuration have been carried out depositing each time different fungi concentrations, with the purpose of being able to discriminate between them. This time, due to convergence issues of the numerical simulator with spheres, fungi have been characterized as cylinders, with radius $r_f = 2 \mu\text{m}$, height $h_f = 1 \mu\text{m}$; and permittivity $\epsilon_{\text{fungi}} = 8$. As the unit cell of this structure has lower dimensions than the ones studied previously, this time we have deposited lower fungi concentrations too. Concretely, we have analyzed the following amounts of fungi: $N = 5$, $N = 20$, $N = 50$ and $N = 100$. Several simulations were made for each case, to observe statistically where the resonance took place, and how big the variance between different samples within the same case is. The results are shown in figure 3.41 and table 3.6.

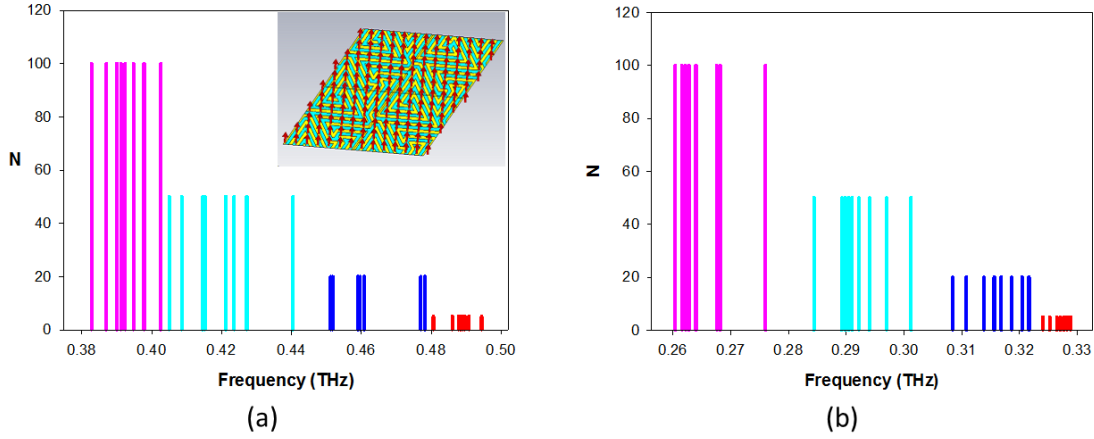


FIG. 3.41. (a) Representation of the frequency resonance for all the simulations carried out for $N = 5$ (red curve), $N = 20$ (blue curve), $N = 50$ (cyan curve), and $N = 100$ (pink curve) for transmission configuration. (b) The same as (a) for reflection configuration.

(a)

| N | Frequency resonance for different simulations (GHz) | | | | | | | | | | Average(GHz) | Variance |
|-----|---|-------|-------|-------|-------|-------|-------|-------|-------|-------|--------------|----------|
| 0 | | | | | | | | | | | 496 | |
| 5 | 487.8 | 487.8 | 489.0 | 486.0 | 490.8 | 487.8 | 489.6 | 488.4 | 480.6 | 494.4 | 483.2 | 30.8 |
| 20 | 478.2 | 451.8 | 451.2 | 459.0 | 477.0 | 460.8 | 477.0 | 477.0 | 477.0 | 459.6 | 449.5 | 67.1 |
| 50 | 440.4 | 415.2 | 421.2 | 415.2 | 427.2 | 405.0 | 421.2 | 414.6 | 423.6 | 408.6 | 411.2 | 124 |
| 100 | 392.4 | 402.6 | 390.0 | 392.4 | 397.8 | 394.8 | 382.8 | 391.2 | 387.0 | 391.2 | 380.9 | 72.3 |

(b)

| N | Frequency resonance for different simulations (GHz) | | | | | | | | | | Average(GHz) | Variance |
|-----|---|-------|-------|-------|-------|-------|-------|-------|-------|-------|--------------|----------|
| 0 | | | | | | | | | | | 329 | |
| 5 | 327.0 | 324.0 | 325.2 | 327.0 | 325.2 | 327.6 | 328.2 | 325.2 | 328.8 | 326.4 | 326.5 | 2.3 |
| 20 | 310.9 | 315.6 | 320.4 | 313.8 | 318.6 | 316.8 | 308.4 | 318.6 | 321.6 | 316.8 | 316.1 | 17.2 |
| 50 | 289.8 | 290.4 | 292.2 | 294.0 | 289.2 | 291.0 | 297.0 | 289.8 | 301.2 | 284.4 | 291.9 | 21.4 |
| 100 | 260.4 | 262.8 | 262.8 | 264.0 | 276.0 | 261.6 | 268.2 | 262.2 | 261.6 | 267.6 | 264.7 | 22.2 |

Table 3.6. (a) Frequency resonance for all the simulations carried out for each fungi concentration, average and variance for each case for transmission configuration. (b) The same as (a) for reflection configuration.

As in case of cross-dipole, this variation of the resonance frequency is due to the arrangement of the fungi in the structure. For the rest of the study, we have taken the curves closest to the average represented on table 3.6, and represented them in figure 3.42(b). As we can observe, if we choose this curves, the overlapping between the different fungi concentrations disappears.

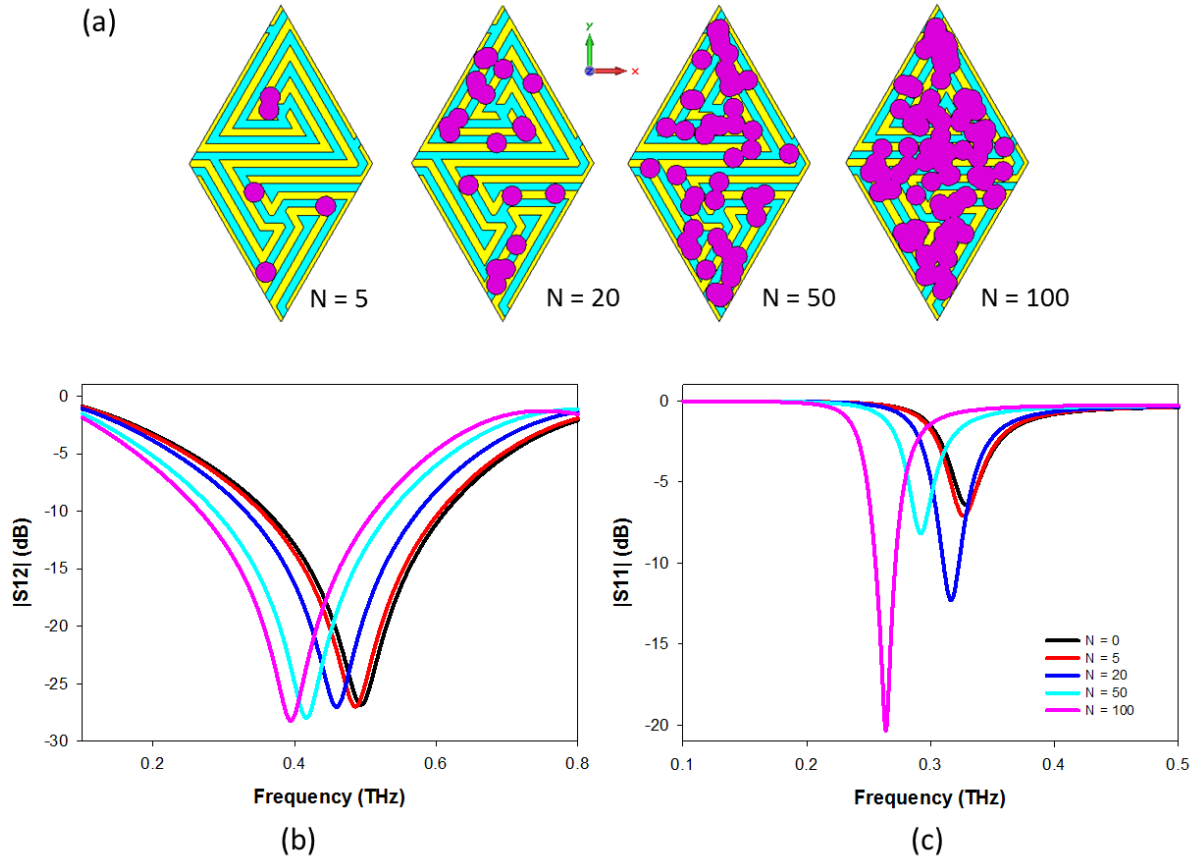


FIG. 3.42. (a) Front view of the structure with $N = 5$, $N = 20$, $N = 50$, and $N = 100$ fungi (purple cylinders). (b) Results of simulated transmission for different fungi concentrations. (c) Results of simulated reflection for different fungi concentrations.

We can observe that the resonance frequency experiments a redshift in both configurations, transmission and reflection, that increases with the fungi concentration. A minimum frequency shift of 12 GHz (transmission) and 2.6 GHz (reflection), and a maximum of 104 GHz (transmission) and 65 GHz (reflection), that corresponds with a relative variation of 2.4%, 0.8%, 21%, and 20% respectively, can be observed for the extreme cases respectively, $N = 5$ and $N = 100$ fungi. We can see this variation of the frequency plotted in figure 3.43.

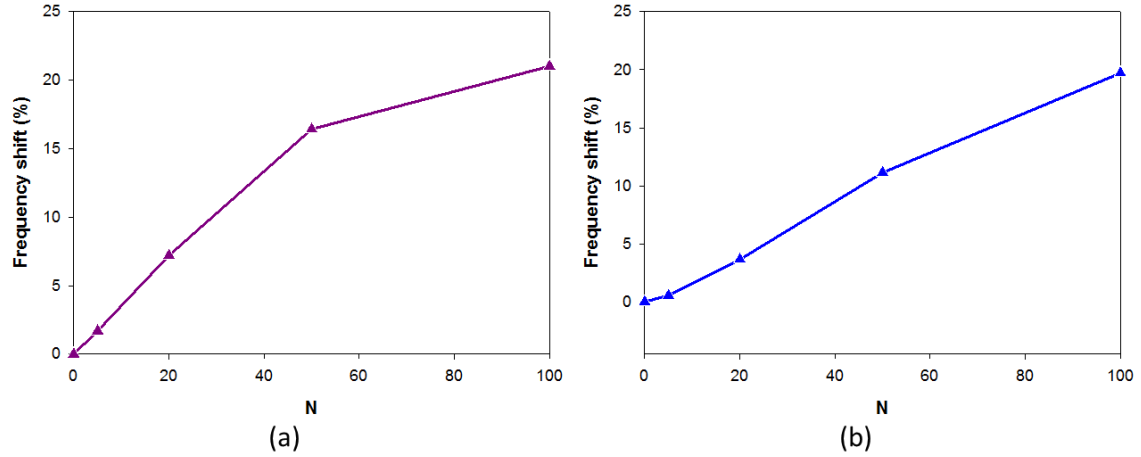


FIG. 3.43. (a) Resonance frequency shift vs. fungi concentration, transmission configuration. (b) Same as (a), reflection configuration.

As it was seen before for the structure operating as a refractometer, the frequency shift achieved is pretty similar for both configurations, transmission and reflection. In this case the sensitivity varies between 0.4 and 1.8 in transmission, and between 0.3 and 0.8 in reflection. As before, we have the opposite situation if we observe the FoM, since in this case the values are higher in reflection than in transmission, with a maximum value of 0.02 (reflection) and 9.1×10^{-4} (transmission). This, again, can be explained because of the difference between the width of the FWHM in both cases, being quite narrower in the case of reflection. (See figure 3.44).

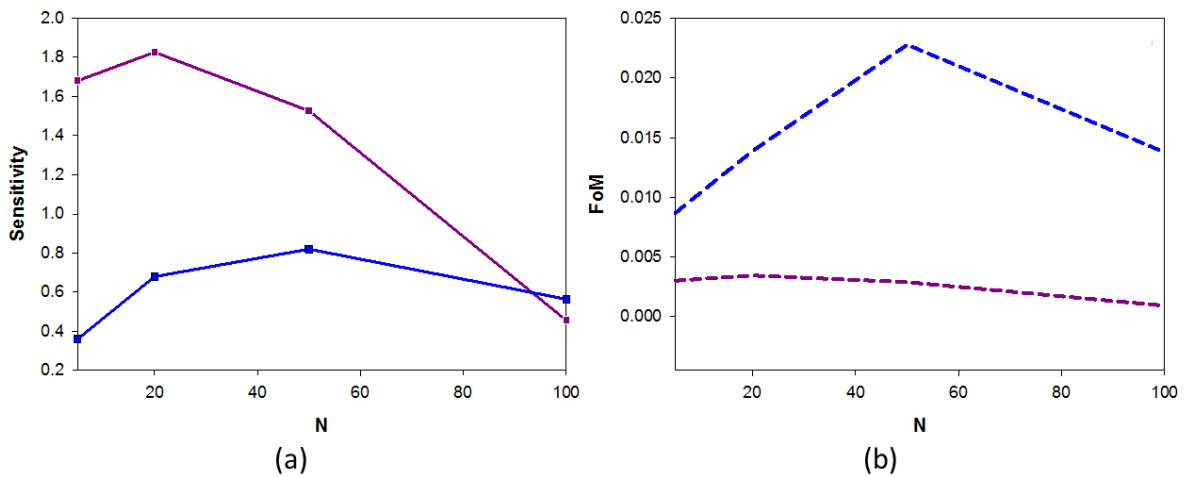


FIG. 3.44. (a) Sensitivity for transmission configuration (purple curve), and the same for reflection configuration (blue curve). (b) FoM for transmission configuration (purple dotted curve), and the same for reflection configuration (blue dotted curve).

Even though these values are smaller than in other studies performed, one must keep in mind that we are depositing very small concentrations of fungi, and still are being able to

detect them, so this demonstrates that this structure can be envisaged as a competitive biological sensor.

Since this is a more complex structure, we have represented the surface currents and electric field at the resonance frequency of the empty unit cell, to see in which areas the intensity is greater, and filled these areas with fungi to test if we get a greater frequency shift. (See figure 3.45 and 3.46).

When the fungi are placed in the zones where the interaction with the electric field is greater, we obtain a shift equivalent to the case of $N = 100$, but with only $N = 16$ fungi.

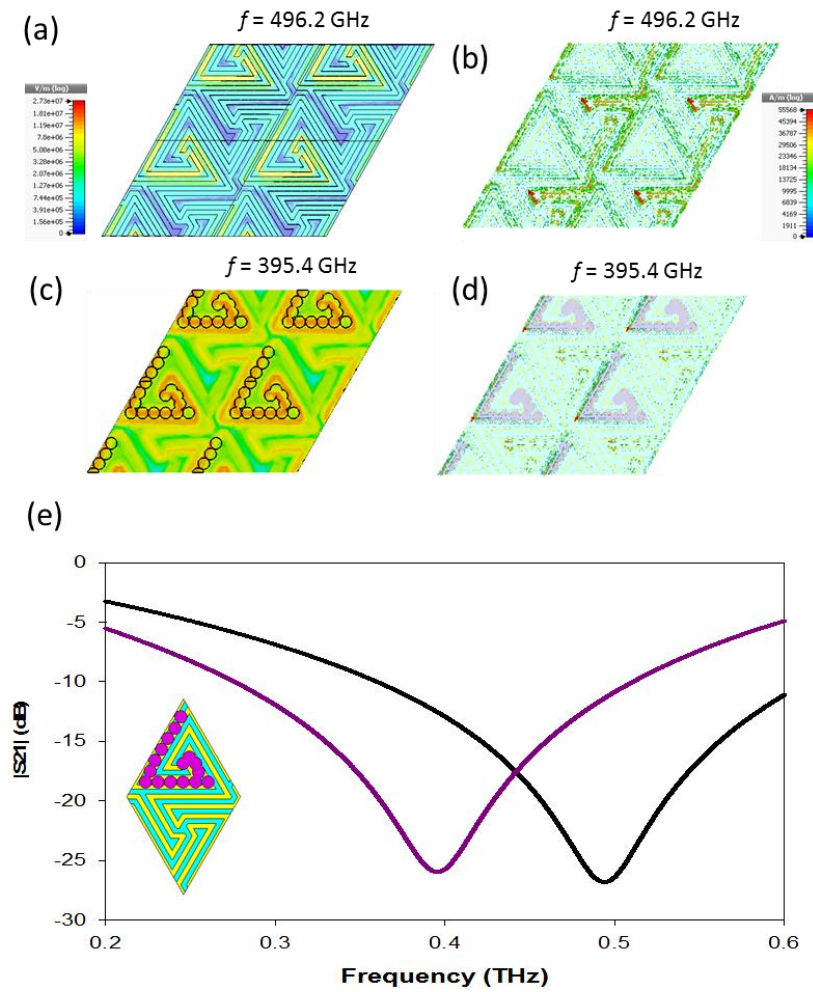


FIG. 3.45. (a) Electric field for the empty structure (transmission): arrow representation. (b) Surface currents for the empty structure (transmission): arrow representation. (c) The same as (a) for $N = 16$ fungi placed at the regions of large electric field concentration and transmission mode. (d) The same as (b) for $N = 16$ fungi placed at the regions of large electric field concentration and transmission mode. (e) Transmission coefficient (purple curve) and comparison with the empty structure, without fungi (black solid curve) for the transmission mode.

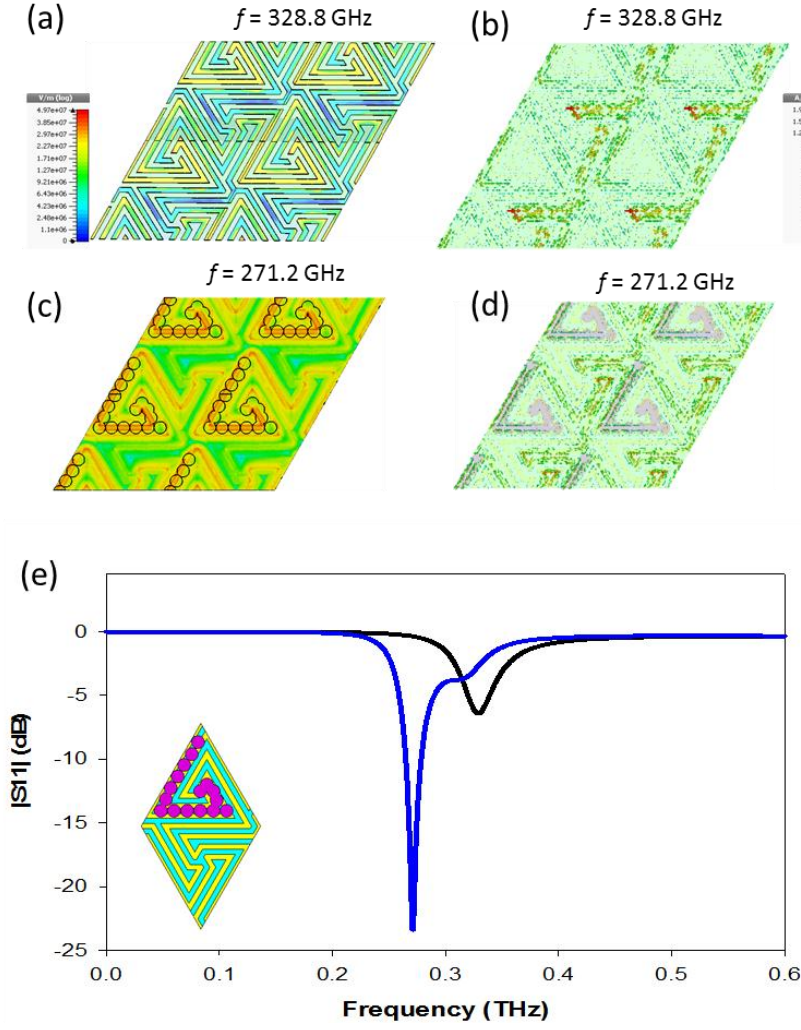


FIG. 3.46. (a) Electric field for the empty structure (reflection): arrow representation. (b) Surface currents for the empty structure (reflection): arrow representation. (c) The same as (a) for $N = 16$ fungi placed at the regions of large electric field concentration and reflection mode. (d) The same as (b) for $N = 16$ fungi placed at the regions of large electric field concentration and reflection mode. (e) Reflection coefficient (blue curve) and comparison with the empty structure, without fungi (black solid curve) for the reflection configuration.

3.3.1. Inductive structure

As before, this time we have an aluminum thin film of $0.4 \mu\text{m}$ thickness and conductivity, $\sigma_{Al} = 3.56 \times 10^7$ S/m on top of PP substrate of same thickness $h_{PP} = 29 \mu\text{m}$, permittivity $\epsilon_{PP} = 2.25$, and lost tangent. $\delta_{PP} = 0.001$. The same two configuration as in the capacitive structure will be studied: transmission (without ground plane) and reflection (with ground plane of thickness $h_G = 1.2 \mu\text{m}$). The boundary conditions and the schematic of the unit cell are shown in figure 3.47.

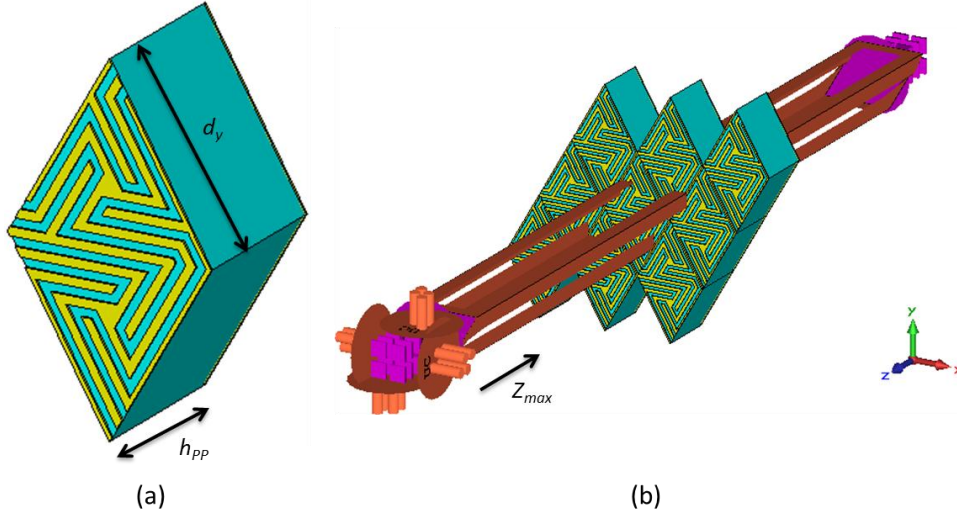


FIG. 3.47.(a) Schematic of the unit cell with a ground plane. Dimensions: polypropylene substrate height, $h_{pp} = 29 \mu\text{m}$; unit cell lateral period, $d_y = 36.4 \mu\text{m}$; aluminum thickness, $h_{Al} = 0.4 \mu\text{m}$; ground plane thickness, $h_G = 0.4 \mu\text{m}$. Dielectric properties of the substrate: PP permittivity, $\epsilon_{pp} = 2.25$; loss tangent, $\delta_{pp} = 0.001$. Electric properties of the metallic film: Aluminum electric conductivity, $\sigma_{Al} = 3.56 \times 10^7 \text{ S/m}$. (b) Boundary conditions of the unit cell.

The same simulation characteristics have been chosen: orthogonal polarizations, vertical and horizontal; and the same simulation characteristics as before: Unit Cell boundary conditions in x and y axes, and Open + Add Space (i.e. perfectly matched layers) in z axis, taking the excitation from Z_{max} . The structure was simulated in the frequency span from 800 GHz to 1500 GHz in the case of transmission; and from 600 GHz to 1000 GHz in the reflection configuration. We can see the transmission and reflection of the empty inductive structure for vertical polarization in figure 3.48.

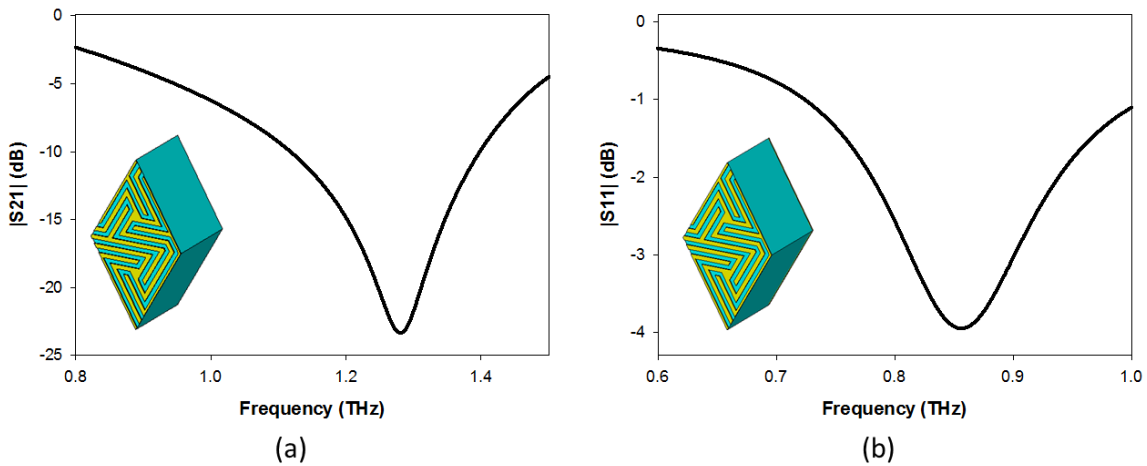


FIG. 3.48. (a) Results of simulated empty structure. (b) Results of simulated vertical absorption empty structure.

Inductive structures always have a peak of transmission in DC (at $f = 0$ Hz) due to its equivalent inductive circuit, where an inductance acts as a short circuit. In our case, this is not different. The structure presents a peak of transmission, but this peak is too wide and not convenient for sensing applications. Therefore, we chose to work with the first dip after the transmission peak which is narrower.

It can be observed that the structure without ground plane presents a stop-band resonance at $f_{RT} = 1280$ GHz in transmission, whereas the structure with ground plane has an reflection dip at $f_{RA} = 856$ GHz, where the reflection is around -5 dB and, obviously the transmission is null due to the presence of the ground plane. We realize that with the same dimensions as for the capacitive structure, the resonance in this case is located at much higher frequencies in both cases: 1280 GHz instead of 496 (transmission), and 856 GHz instead of 329 GHz (reflection). To study the inductive structure behavior as a refractometer, we have deposited, again, analyte of thickness $3\text{ }\mu\text{m}$ and varied its refractive index from 1 to 2 with a step width of 0.2. The results of this simulation, both transmission and absorption are shown in figure 3.49.

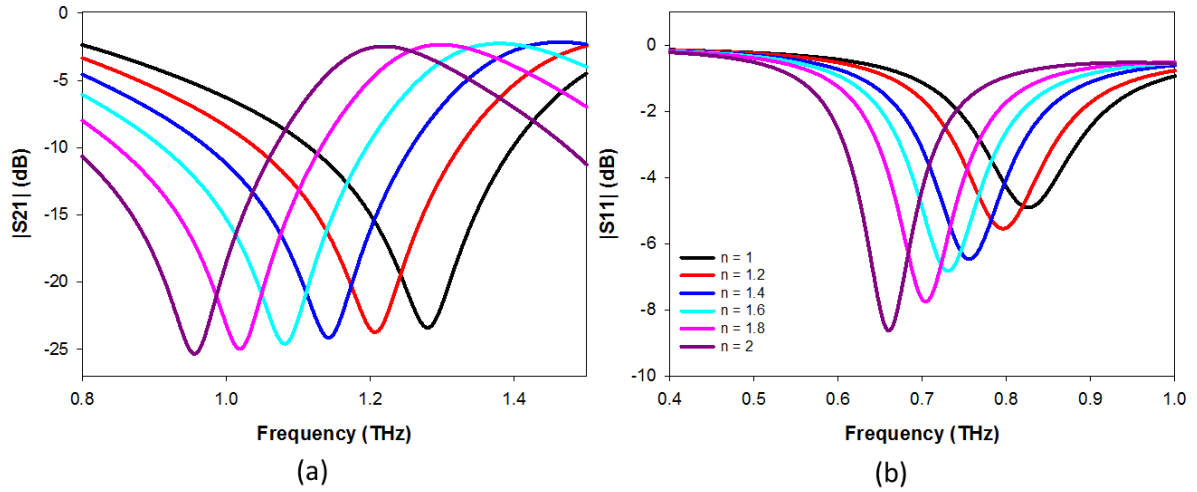


FIG. 3.49. (a) Transmission with analyte thickness $h_a = 3\text{ }\mu\text{m}$ and different refractive index values. (b) Reflection with analyte thickness $h_a = 3\text{ }\mu\text{m}$ and different refractive index values.

Again, the frequency shift increases with the refractive index. In this case, we have a minimum frequency shift of 74 GHz in transmission, and a frequency shift of 44 GHz in reflection. These values correspond with relative shifts of 5.8% and 5.14% respectively, greater than the shift values reached in the capacitive structure (4.7% and 1.3%). This structure also has greater maximum shift values, reaching a displacement of 325 GHz (25.4%) in transmission, and 208 GHz (24.3%) in reflection, overtaking the 19% and 20% of the previous structure. We can observe this frequency shift in figure 3.50.

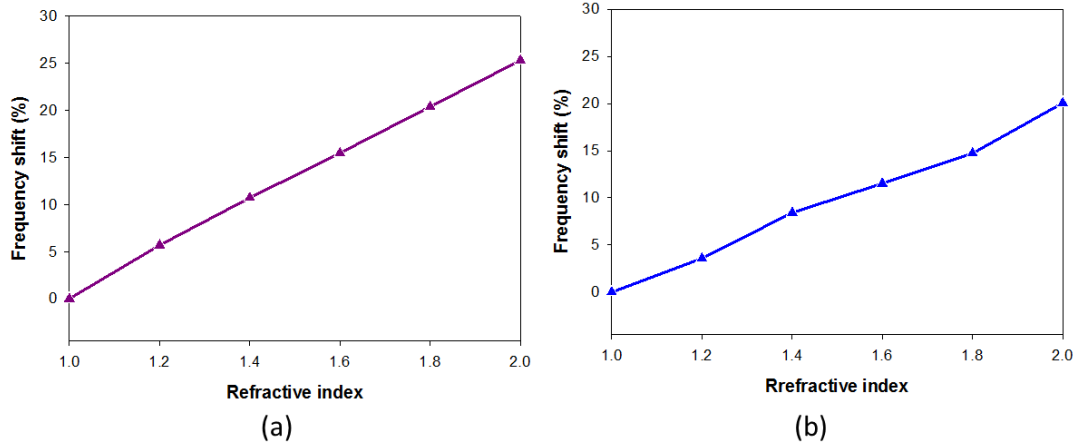


FIG. 3.50. (a) Resonance frequency shift vs. refractive index for $h_a = 3 \mu\text{m}$, transmission. (b) Same as (a), reflection configuration.

From these values of frequency shift, we obtain a sensitivity that varies between 304 and 364 for the transmission configuration, and between 132 and 220 for the reflection mode. Thus in terms of sensitivity solely the transmission structure has better quality values. But, regarding the FoM, the transmission mode has values between 0.53 and 0.6, while the reflection configuration reaches values from 1.2 to 2.1. (See figure 3.51). This difference between both cases is due to the narrower FWHM of the reflection mode.

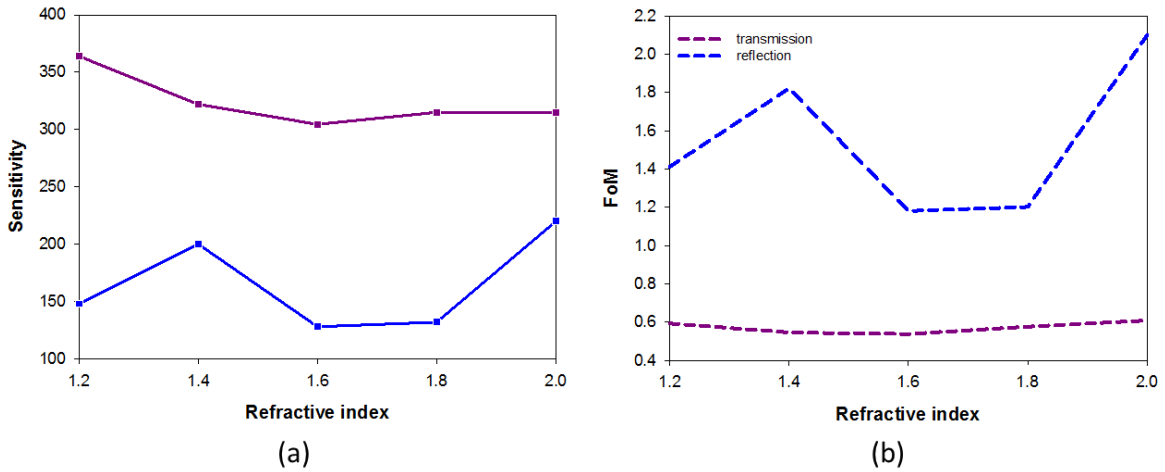


FIG. 3.51. (a) Sensitivity for transmission configuration (purple curve), and the same for reflection configuration (blue curve). (b) FoM for transmission configuration (purple dotted curve), and the same for reflection configuration (blue dotted curve).

We can observe that the values reached for the sensitivity are better in this structure than in the capacitive one, having maximum values of 364 (transmission) and 220 (reflection) in the inductive structure instead of 124 (transmission) and 108 (reflection) in the capacitive. On the other hand, the values of FoM are also a little better for the transmission in this case (0.6 vs 0.2), but lower for the reflection configuration (maximum of 2.1 vs maximum of 3). This comparison and the following between both structures is presented at the end of this section, in table 3.7.

The procedure to perform the study of the structure as a fungi detector is the same as before: fungi characterized as cylinders, with radius $r_f = 2 \mu\text{m}$, height $h_f = 1 \mu\text{m}$; and permittivity $\epsilon_{\text{fungi}} = 8$; and concentrations of $N = 5$, $N = 20$, $N = 50$ and $N = 100$; and ten different simulations, first for the structure without ground plane and then for the ground plane configuration for each case. We can observe the results of all the simulations in figure 3.52 and table 3.7.

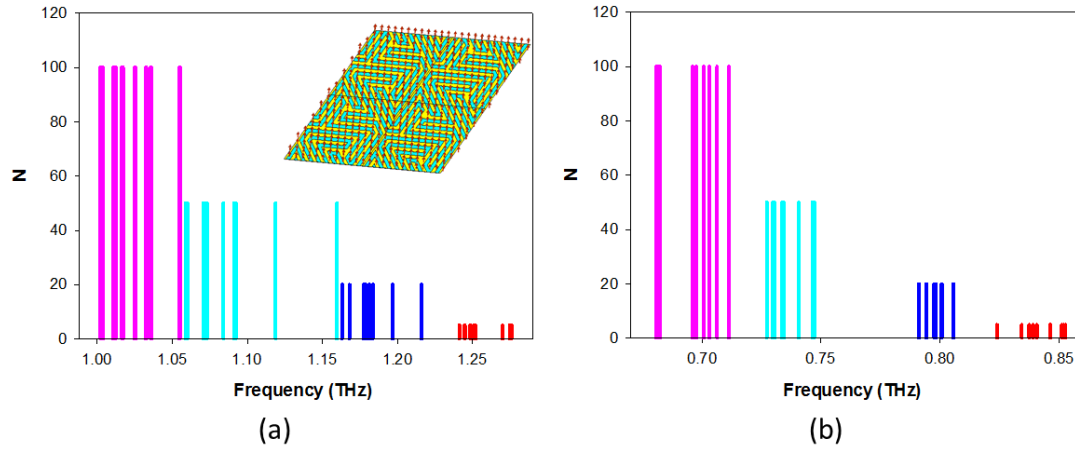


FIG. 3.52. (a) Representation of the frequency resonance for all the simulations carried out for $N = 5$ (red curve), $N = 20$ (blue curve), $N = 50$ (cyan curve), and $N = 100$ (pink curve) for transmission configuration for vertical polarization (inset). (b) The same as (a) for reflection configuration.

(a)

| N | Frequency resonance for different simulations (GHz) | | | | | | | | | | Average(GHz) | Variance |
|-----|---|--------|--------|--------|--------|--------|--------|--------|--------|--------|--------------|----------|
| 0 | | | | | | | | | | | 1280.8 | |
| 5 | 1244.8 | 1276.0 | 1250.8 | 1270.0 | 1248.4 | 1241.2 | 1250.8 | 1252.0 | 1276.0 | 1274.8 | 1258.4 | 195.5 |
| 20 | 1163.2 | 1181.2 | 1183.6 | 1196.8 | 1168.0 | 1178.8 | 1216.0 | 1177.6 | 1168.0 | 1178.8 | 1181.5 | 268.8 |
| 50 | 1058.8 | 1092.4 | 1073.2 | 1084.0 | 1118.8 | 1060.0 | 1084.0 | 1070.8 | 1091.2 | 1159.6 | 1089.3 | 919 |
| 100 | 1054.8 | 1036.0 | 1032.4 | 1010.8 | 1012.0 | 1003.6 | 1025.2 | 1016.8 | 1025.2 | 1054.8 | 1022.6 | 389 |

(b)

| N | Frequency resonance for different simulations (GHz) | | | | | | | | | | Average(GHz) | Variance |
|-----|---|-------|-------|-------|-------|-------|-------|-------|-------|-------|--------------|----------|
| 0 | | | | | | | | | | | 856 | |
| 5 | 846.4 | 837.6 | 851.2 | 840.8 | 840.8 | 839.2 | 834.4 | 852.0 | 852.8 | 824.0 | 840.8 | 22.6 |
| 20 | 794.4 | 805.6 | 794.4 | 794.4 | 805.6 | 800.8 | 798.4 | 791.2 | 797.6 | 791.2 | 800 | 45.6 |
| 50 | 729.6 | 746.4 | 734.4 | 747.2 | 733.6 | 729.6 | 727.2 | 740.8 | 730.4 | 747.2 | 742.6 | 96.5 |
| 100 | 697.6 | 680.8 | 700.8 | 682.4 | 706.4 | 711.2 | 696.0 | 703.2 | 681.6 | 700.8 | 695.2 | 68.5 |

Table 3.7. (a) Frequency resonance for all the simulations carried out for each fungi concentration, average and variance for each case for transmission configuration. (b) The same as (a) for reflection configuration.

As in the capacitive structure, and for the rest of the study, we have taken the curves closest to the average represented in table 3.7, and represented them in figure 3.53. If choosing this curves, the overlapping between the different fungi concentrations disappears.

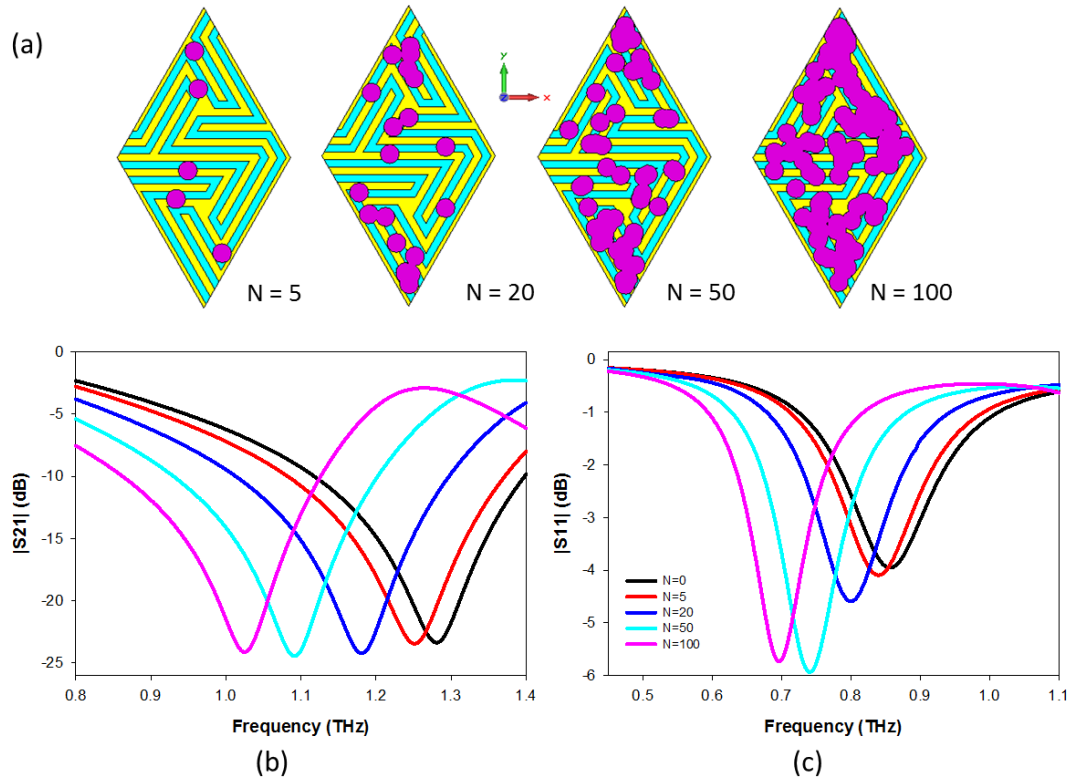


FIG. 3.53. (a) Front view of the structure with $N = 5$, $N = 20$, $N = 50$, and $N = 100$ fungi (purple cylinders). (b) Results of simulated transmission for different fungi concentrations. (c) Results of simulated reflection for different fungi concentrations.

We can see that there is a redshift on the frequency resonance for both configurations, which increases with the fungi concentration. This time, we have a minimum frequency shift ($N = 5$) of 21.6 (1.68%) for transmission configuration, and 15.2 (1.77%) for reflection configuration. The maximum frequency shift ($N = 100$) that we have achieved is 258 GHz (20%) for transmission and 161 GHz (19%) for reflection; values similar to what we observed in the capacitive structure. We can observe this frequency shift plotted in figure 3.54.

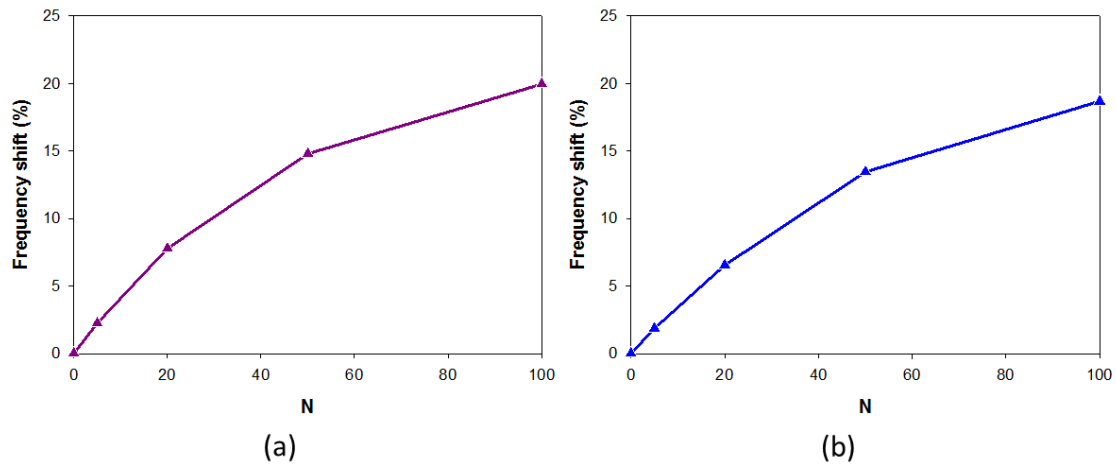


FIG. 3.54. (a) Resonance frequency shift vs. fungi concentration for vertical polarization, transmission configuration. (b) Same as (a), reflection configuration.

The values are rather similar in both configurations, and also with respect to the values achieved for the capacitive structure. The sensitivity has been plotted in figure 3.55. It reaches values between 1.3 and 5.8 in transmission, and between 0.9 and 3.2 in reflection. This means an enhancement of 69% (transmission) and 75% (reflection) from the capacitive structure. Regarding the FoM, we have a maximum of 9×10^{-3} in transmission, and 0.04 in reflection. Again, we obtain larger values than in the previous structure, with an increment of 90% (transmission) and 50% (reflection).

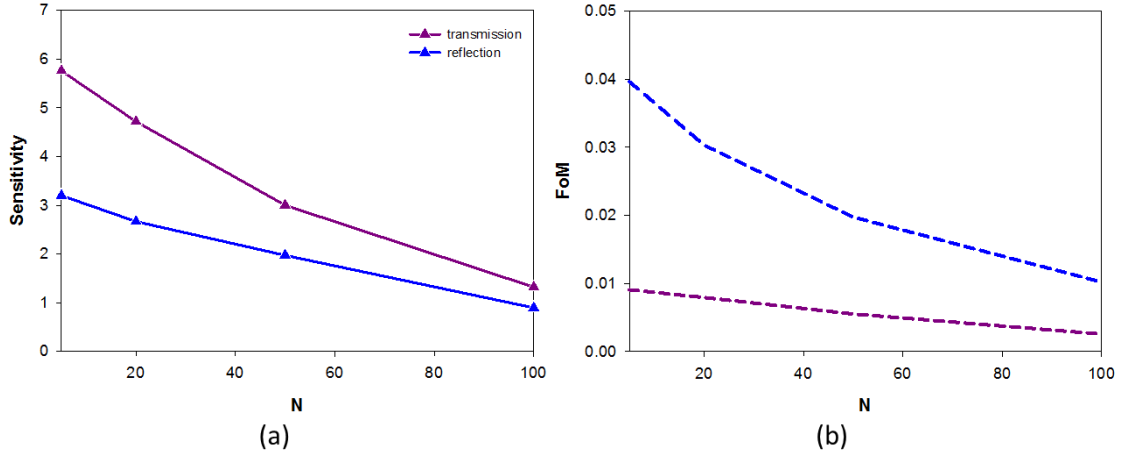


FIG. 3.55. (a) Sensitivity for transmission configuration (purple curve), and the same for reflection configuration (blue curve). (b) FoM for transmission configuration (purple dotted curve), and the same for reflection configuration (blue dotted curve).

As we did in the previous structure, we have represented the surface currents and electric field at the resonance frequency of the empty unit cell, to see in which areas the intensity is larger, and filled these areas with fungi to test if we get a greater frequency shift, see figure 3.56 and 3.57.

When placing the fungi in regions where the interaction with intense electric field, we obtain the curves plotted in figure 3.56(e) and 3.57(e). As we can observe, we have a frequency shift of 187 GHz (transmission) and 88 GHz (reflection); so we are achieving a shift equivalent to the case $N = 50$, but with only $N = 14$, which highlights, once again, the importance of the fungi location.

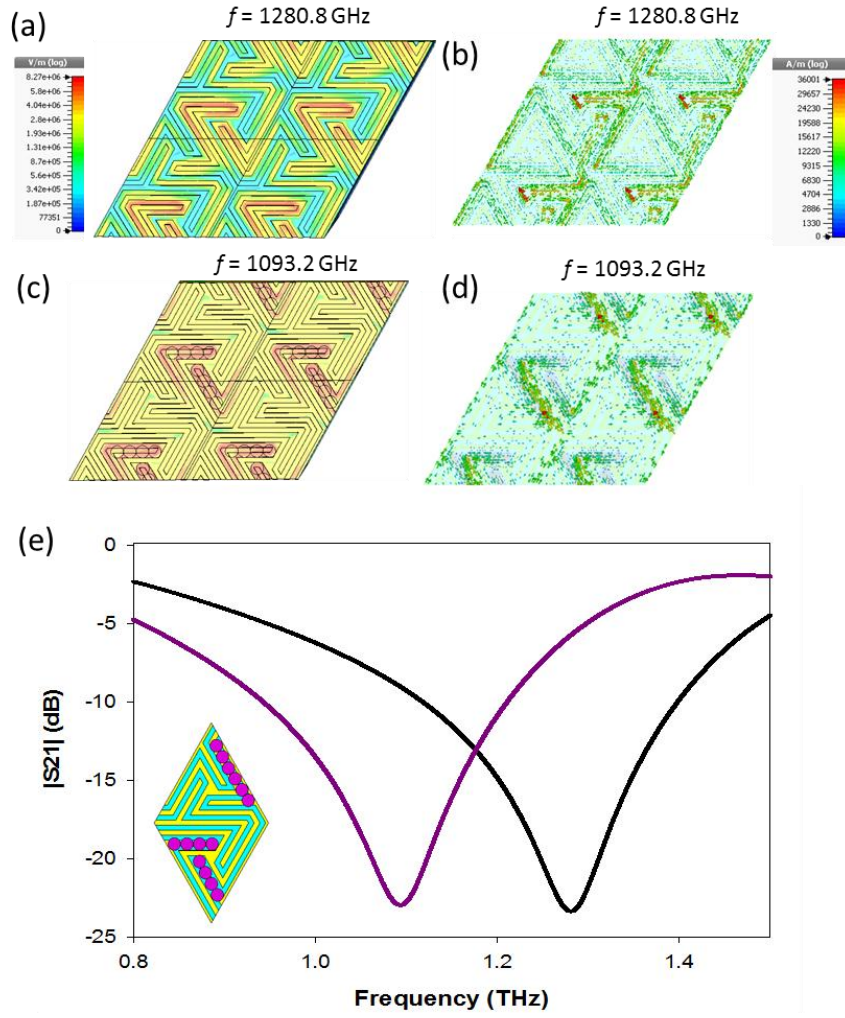


FIG. 3.56. (a) Electric field for the empty structure (transmission): arrow representation. (b) Surface currents for the empty structure (transmission): arrow representation. (c) The same as (a) for $N = 14$ fungi placed at the regions of large electric field concentration and transmission mode. (d) The same as (b) for $N = 14$ fungi placed at the regions of large electric field concentration and transmission mode. (e) Transmission coefficient for vertical polarization (purple solid curve) and comparison with the empty structure, without fungi (black solid curve) for the transmission mode.

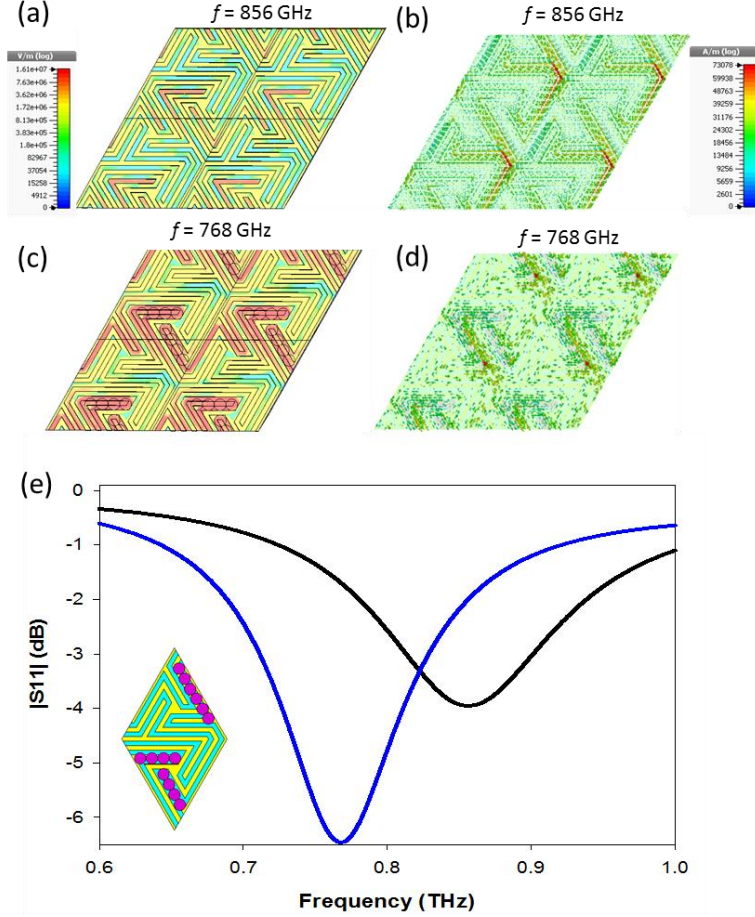


FIG. 3.57. (a) Electric field for the empty structure (reflection): arrow representation. (b) Surface currents for the empty structure (reflection): arrow representation. (c) The same as (a) for $N = 14$ fungi placed at the regions of large electric field concentration and reflection mode. (d) The same as (b) for $N = 14$ fungi placed at the regions of large electric field concentration and reflection mode. (e) Reflection coefficient for vertical polarization (blue solid curve) and comparison with the empty structure, without fungi (black solid curve) for the reflection configuration.

To sum up, a comparison between both structures, capacitive and inductive; and both configurations, transmission and reflection are shown in table 3.8. Table 3.8(a) shows the comparison between both structures acting as a refractometer. If we focus on the quality parameter, the FoM, we can observe that in this case the inductive structure has quite better values than the capacitive. In table 3.8(b) we can observe the comparison between both structures acting as a fungi detector. Again, looking at the FoM we can say that the inductive structure presents better values. We can also note that, in general, the sensitivity reaches higher values in the transmission configuration. However, we have the opposite if we focus on the FoM, being the values reached by the reflection configuration notably higher. As we said before, the FoM is a more realistic and practical parameter to measure the quality of a sensor, so we can say that the structure with ground plane (reflection) may be better option for the task of sensing.

Anyway, with the results obtained in this study, we can say that these structures, both capacitive and inductive, presents good performance as fungi detector in both configurations

(transmission and reflection). In fact this structure is able to detect extremely small amount of fungi ($N = 5$), with a notable frequency shift.

(a)

| | | Capacitive | | Inductive | |
|-----------------|-----------------|--------------|------------|--------------|------------|
| | | Transmission | Reflection | Transmission | Reflection |
| Empty structure | Resonance (GHz) | 496 | 329 | 1280 | 856 |
| n = 1 | Resonance (GHz) | 492 | 329 | 1279.4 | 825.6 |
| | Δf (%) | 0.8 | 0 | 0 | |
| n = 1.2 | Resonance (GHz) | 465.6 | 320.4 | 1206.6 | 796 |
| | Δf (%) | 6.2 | 2.6 | 5.7 | 3.6 |
| n = 1.4 | Resonance (GHz) | 439.2 | 301.8 | 1142.2 | 756 |
| | Δf (%) | 11.4 | 8.26 | 10.7 | 8.4 |
| n = 1.6 | Resonance (GHz) | 414.4 | 271.2 | 1081.3 | 730.4 |
| | Δf (%) | 16.4 | 17.6 | 15.5 | 11.5 |
| n = 1.8 | Resonance (GHz) | 389.6 | 261 | 1018.3 | 704 |
| | Δf (%) | 21.4 | 20.7 | 20.4 | 14.7 |
| n = 2 | Resonance (GHz) | 367.2 | 248.4 | 955.3 | 660 |
| | Δf (%) | 26 | 24.5 | 25.3 | 20 |
| Sensitivity | | 112-132 | 42-153 | 304-364 | 228-220 |
| FoM | | 0.22-0.24 | 1.1-4.5 | 0.53-0.6 | 1.2-2 |

(b)

| | | Capacitive | | Inductive | |
|-------------|-----------------|----------------------|----------------------|----------------------|------------|
| | | Transmission | Reflection | Transmission | Reflection |
| N = 0 | Resonance (GHz) | 496 | 329 | 1280 | 856 |
| N = 5 | Resonance (GHz) | 483.2 | 326.5 | 1252 | 840 |
| | Δf (%) | 2.6 | 0.8 | 2.2 | 1.9 |
| N = 20 | Resonance (GHz) | 449.5 | 316.1 | 1181.2 | 800 |
| | Δf (%) | 9.4 | 4 | 7.8 | 6.5 |
| N = 50 | Resonance (GHz) | 411.2 | 291.9 | 1091.2 | 740.8 |
| | Δf (%) | 17.1 | 11.3 | 14.8 | 13.5 |
| N = 100 | Resonance (GHz) | 380.9 | 264.7 | 1025.2 | 696 |
| | Δf (%) | 23.2 | 19.5 | 20 | 18.7 |
| Sensitivity | | 0.5-1.8 | 0.4-0.8 | 1.3-5.8 | 0.9-3.2 |
| FoM (máx) | | 3.4×10^{-3} | 1.4×10^{-2} | 0.9×10^{-2} | 0.02 |

Table 3.8. Comparison between capacitive structure and inductive structure. (a) Comparison of both structures as a refractometer. (b) Comparison of both structures as a fungi detector.

3.4. Experimental measurements

Up to now, in this chapter we have numerically evaluated different DP-FSS, of both types capacitive and inductive. In this section we present the initial experimental

measurements we carried out to demonstrate the previous findings. All the prototypes were fabricated on a thin film PP substrate. The FSS was lithographically patterned on a $0.35\ \mu\text{m}$ thick Al layer sputtered on the PP slab via vacuum thermal deposition method. Prior to sputtering, the PP film was treated with a glow discharge in Ar atmosphere to improve adhesion of Al to PP. To pattern the FSS, we employed a contact photolithography technique, which was specifically adapted to flexible solid film substrates, such as PP, whose industrial production does not allow obtaining a liquid material suitable for posterior film deposition via spin coating. The microscope pictures of the three prototypes and line widths can be seen in figure 3.58 and table 3.9. The geometries of the fabricated DP-FSS prototypes are listed within the table 3.10.


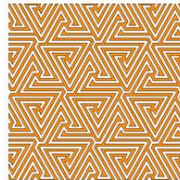
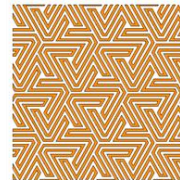
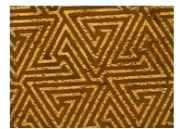


| | Capacitive FSS #1 | Inductive FSS #1 | Capacitive FSS #2 |
|--------------------|---|---|---|
| Geometry |  |  |  |
| Microscope picture |  |  |  |
| PP / Al | $h_{PP} = 100\ \mu\text{m}$ | $h_{PP} = 50\ \mu\text{m}$ | $h_{PP} = 50\ \mu\text{m}$ |

Table 3. 9. Geometries of fabricated DP-FSS and PP thickness.

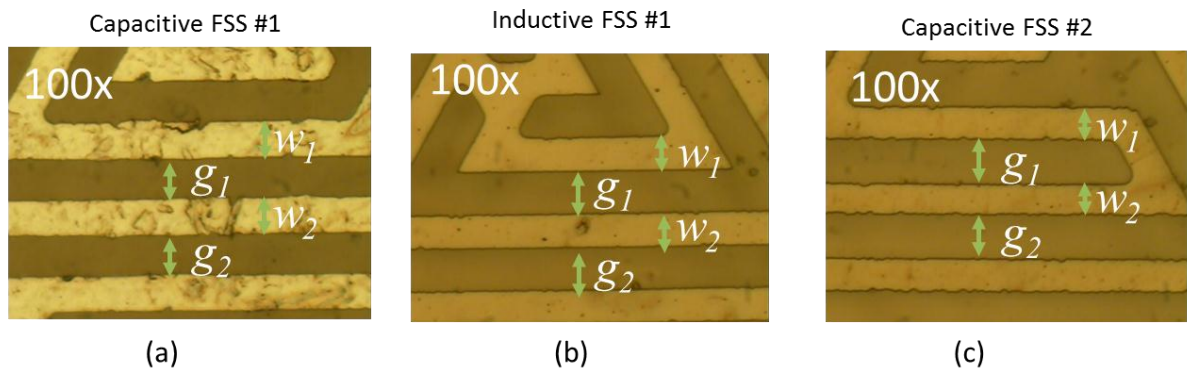


Fig. 3. 58. Microscope 100x magnifications for the three prototypes.

| Dimension | Capacitive FSS #1 (μm) | error | Inductive FSS #1 (μm) | error | Capacitive FSS #2 (μm) | error |
|-----------|--|-------|---------------------------------------|-------|--|-------|
| w_1 | ≈ 9.3 | 7% | ≈ 8.5 | 15% | ≈ 8.7 | 13% |
| w_2 | ≈ 9.3 | 7% | ≈ 8.9 | 11% | ≈ 8.3 | 17% |
| g_1 | ≈ 11 | 10% | ≈ 11.5 | 15% | ≈ 12.1 | 21% |
| g_2 | ≈ 10.7 | 7% | ≈ 12 | 20% | ≈ 12.1 | 21% |

Table 3.10. Line widths for the different prototypes and error.

The structures were simulated using the frequency domain solver of CST, with the simulation parameters that are described in the previous chapters. The experimental measurements were performed using the ABmm VNA, as explained in chapter 2, with different frequency spans depending on the structure studied:

- Capacitive #1 : frequency span between 45 GHz and 70 GHz (V band), with a step width of 20 MHz.
- Inductive #1 : frequency span between 110 GHz and 160 GHz (D band), with a step width of 20 MHz.
- Capacitive #2 : frequency span between 68GHz and 112 GHz (W band) , with a step width of 20 MHz.

Figure 3.59 shows a comparison between the simulated structures, on the right, and the measured ones, on the left. We can observe that in all cases, the measured resonance happens at higher frequencies than the simulated ones. The capacitive #1 structure has its null of transmission at 65 GHz instead of 62 GHz, which corresponds to a blueshift of 3 GHz (6%). The inductive #1 structure presents its pole at 137 GHz instead of 130, which corresponds to a shift of 7 GHz (5%). Finally, the capacitive #2 structure has its resonance at 94 GHz, instead of 70 GHz, which means a shift of 24 GHz (34%). This mismatch can be explained due to the inaccuracy in the process of fabrication. In fact, having a look at figure 3.58 and table 3.10, it can be seen that the line widths deviate from those considered in the simulation process, where the lines were designed to have a width of 10 μm . We can observe that the structure whose simulated and measured results differs more (capacitive #2), is the one with larger error in the width of its lines (it can be observed at first sight in the microscope photographs).

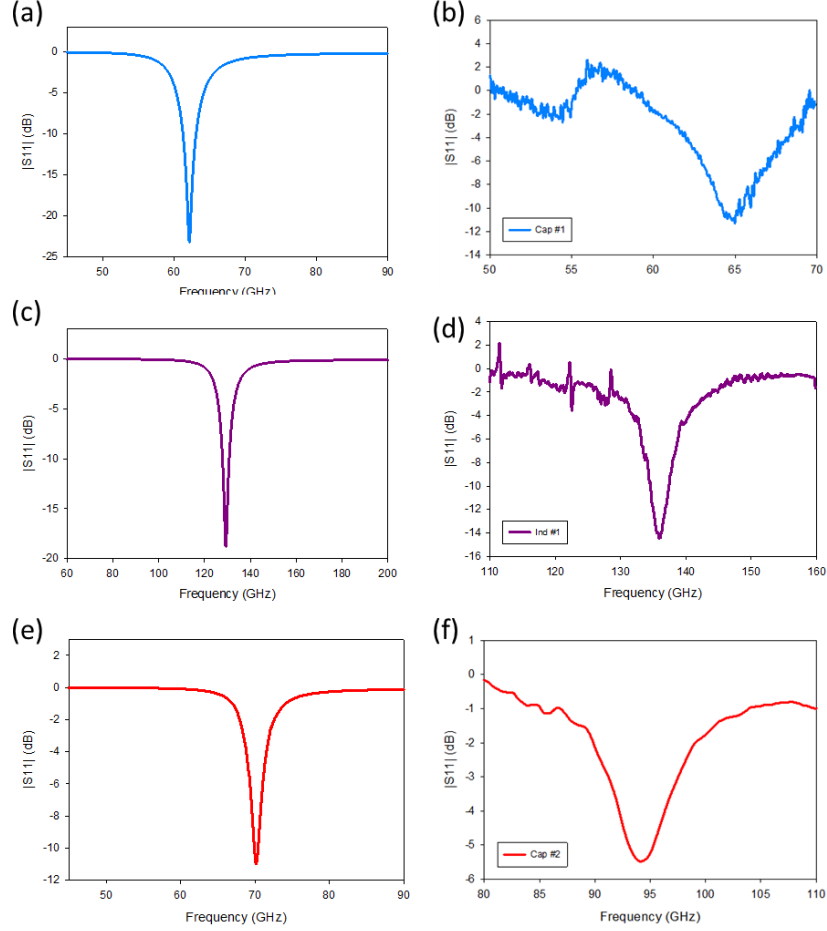


FIG. 3. 59. (a) Simulated reflection coefficient for capacitive #1 structure. (b) Measured reflection coefficient for capacitive #1 structure. (c) The same as (a) for inductive #1 structure. (d) The same as (b) for inductive #1 structure. (e) The same as (a) for capacitive #2 structure. (f) The same as (b) for capacitive #2 structure.

Next, we deposited an analyte made of a photoresistive material on the capacitive (#1) structure by spin coating. The analyte thickness chosen was $h_a = 10 \mu\text{m}$ (approximately), which corresponds to $2.1 \times 10^{-4} \lambda$. We can observe in figure 3.60 that, as we obtained at the simulated results, a frequency redshift takes place. In this case, we achieved a frequency shift of more than 12 GHz, which corresponds to a relative shift of 18.4%. The rest of structures has not been analyzed as thin film sensor because of lack of time, but they will be studied in the future. These are just preliminary results, but they serve to demonstrate the promising sensing capabilities of this type of structures.

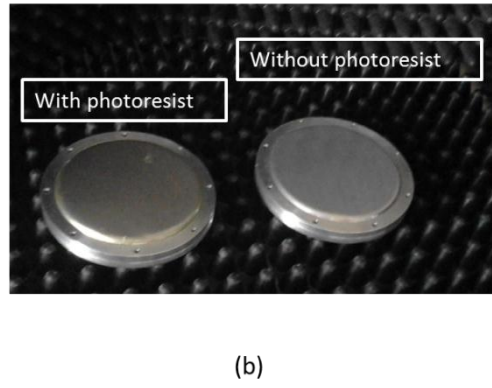
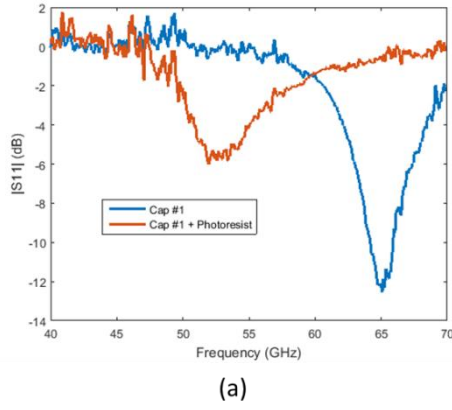


FIG. 3. 60. (a) Measured reflection coefficient for capacitive #1 structure without photoresist (blue curve), and with photoresist of $h_o = 10 \mu\text{m}$ (orange curve) . (b) Picture of the measured samples for the capacitive #1 structure, with and without photoresist.

4. Conclusions and future work

In this chapter, a summary of the conclusions obtained during this work is presented, as well as a list of future lines that could be done in the future, to continue with this work.

4.1. Conclusions

- In this chapter we have demonstrated that sensing in the THz region using metasurfaces and FSS provides interesting results. In our case, the three options chosen for this study have met the expectations set by other studies and papers and, in some cases, the values have been very promising.
- The cross-dipole FSS analyzed shows competitive sensing capabilities in both configurations (patch and slot structures) when used as a refractometer or thin film sensor, with a simple geometry, easy to design, analyze and fabricate. On the other hand, when used as a fungi detector it presents the problem of band overlapping for different fungi concentrations. In this respect, other solutions seem preferable.
- The hole array studied in this work has demonstrated good performance as a thin film sensor, with very encouraging values of sensitivity and FoM for both regular and anomalous ET bands. Furthermore, the potential of the anomalous ET for sensing purposes due to its narrow peak of transmission and frequency dependence has been highlighted.
- Regarding the DPFSS, we have revealed that they are extremely promising structures for high sensitivity biological sensing devices, in our case, fungi detectors. Due to its complex geometry and small size, they allow detecting very small amounts of sample, with high values of sensitivity and FoM. In addition, it is remarkable that these structures are independent of the polarization.
- The experimental measurements carried out, demonstrate the promising performance of DPFSSs as sensors, due to its large frequency shift demonstration when depositing only a $2.1 \times 10^{-4} \lambda$ of material. Although because of lack of time only a single structure has been studied, all of the prototypes presented in this work have potential for sensing purposes, and will be also studied.

4.2. Future work

- Study of the behavior of the Hole Array when depositing analyte on the aluminum side and check if in that configuration we can obtain better sensitivity and FoM values for the regular ET.
- Study of a new structure of hole array, the coaxial hole array, where the electric field concentration should be higher and, at first sight, it could achieve better results for fungi detector.
- Perform a biological study characterizing fungi as cylinders in the hole array and cross-dipole, and check if the frequency shift achieved is better than the one in the case of characterizing fungi as spheres.
- Do the experimental demonstration of all the structures mentioned in this work, measuring all of them at the TERALAB.
- Characterization of DP-FSS, depositing on them biological analyte (fungi or other microorganisms) to check the simulated good results of this work.
- Study the possibility of designing other kind of structures, or with other geometries, with the purpose of obtaining better structures for its use as sensors.

5. Bibliography and references

- [1] M. J. Fitch and R. Osiander, "Terahertz Waves for Communications and Sensing," *Johns Hopkins APL Tech. Dig.*, vol. 25, no. 4, pp. 348–355, 2004.
- [2] P. Rodríguez-Ulibarri and M. Beruete, "Sensing at Terahertz frequencies," 2016.
- [3] P. H. Siegel, "Terahertz technology," *IEEE Trans. Microw. Theory Tech.*, vol. 50, no. 3, pp. 910–928, Mar. 2002.
- [4] V. G. Veselago, "The electrodynamics of substances with simultaneously negative values of ϵ and μ ," *Sov. Phys. Uspekhi*, vol. 10, no. 4, 1968.
- [5] J. A. Porto and F. J. Garcia, "Transmission Resonances on Metallic Gratings with Very Narrow Slits," pp. 2845–2848, 1999.
- [6] D. R. Smith, D. R. Smith, W. J. Padilla, W. J. Padilla, D. C. Vier, D. C. Vier, S. C. Nemat-Nasser, S. C. Nemat-Nasser, S. Schultz, and S. Schultz, "Composite Medium with Simultaneously Negative Permeability and Permittivity," *Phys. Rev. Lett.*, vol. 84, no. 18, pp. 4184–4187, 2000.
- [7] J. B. Pendry, "Negative refraction makes a perfect lens," *Phys. Rev. Lett.*, vol. 85, no. 18, pp. 3966–3969, 2000.

- [8] D. Schurig, J. J. Mock, B. J. Justice, S. A. Cummer, J. B. Pendry, A. F. Starr, and D. R. Smith, "Metamaterial electromagnetic cloak at microwave frequencies.," *Science*, vol. 314, no. 5801, pp. 977–80, Nov. 2006.
- [9] J. B. Pendry, D. Schurig, and D. R. Smith, "Controlling electromagnetic fields.," *Science*, vol. 312, no. 5781, pp. 1780–2, Jun. 2006.
- [10] J. F. O'Hara, W. Withayachumnankul, and I. Al-Naib, "A Review on Thin-film Sensing with Terahertz Waves," *J. Infrared, Millimeter, Terahertz Waves*, vol. 33, no. 3, pp. 245–291, Mar. 2012.
- [11] Z. Jakšić, S. Vuković, J. Matovic, and D. Tanasković, "Negative Refractive Index Metasurfaces for Enhanced Biosensing," *Materials (Basel)*, vol. 4, no. 1, pp. 1–36, Dec. 2010.
- [12] "MetaTHz." [Online]. Available: <http://opto1.artov.imm.cnr.it/metathz/index.php/research-bar/terahertz-metamaterials>.
- [13] I. F. Akyildiz, J. M. Jornet, and C. Han, "Terahertz band: Next frontier for wireless communications," *Phys. Commun.*, vol. 12, pp. 16–32, 2014.
- [14] L. Ho, M. Pepper, and P. Taday, "Terahertz spectroscopy: Signatures and fingerprints," *Nat. Photonics*, vol. 2, no. September, pp. 541–543, 2008.
- [15] M. Tonouchi, "Cutting-edge terahertz technology," *Nat. Photonics*, vol. 1, no. 2, pp. 97–105, Feb. 2007.
- [16] S. J. Park, J. T. Hong, S. J. Choi, H. S. Kim, W. K. Park, S. T. Han, J. Y. Park, S. Lee, D. S. Kim, and Y. H. Ahn, "Detection of microorganisms using terahertz metamaterials.," *Sci. Rep.*, vol. 4, p. 4988, 2014.
- [17] L. Xie, W. Gao, J. Shu, Y. Ying, and J. Kono, "Extraordinary sensitivity enhancement by metasurfaces in terahertz detection of antibiotics.," *Sci. Rep.*, vol. 5, p. 8671, 2015.
- [18] L. Cong, S. Tan, R. Yahiaoui, F. Yan, W. Zhang, and R. Singh, "Experimental demonstration of ultrasensitive sensing with terahertz metamaterial absorbers: A comparison with the metasurfaces," *Appl. Phys. Lett.*, vol. 106, no. 3, p. 031107, 2015.
- [19] P. Rodríguez-Ulibarri, S. A. Kuznetsov, and M. Beruete, "Wide angle terahertz sensing with a cross-dipole frequency selective surface," *Appl. Phys. Lett.*, vol. 111104, 2016.
- [20] T. W. Ebbesen, H. J. Lezec, H. F. Ghaemi, T. Thio, and P. A. Wolff, "Extraordinary optical transmission through sub-wavelength hole arrays," *Nature*, vol. 391, no. 6668, p. 667, 1998.
- [21] I. Avrutsky, Y. Zhao, and V. Kochergin, "Surface-plasmon-assisted resonant tunneling of light through a periodically corrugated thin metal film.," *Opt. Lett.*, vol. 25, no. 9, pp. 595–597, 2000.
- [22] M. Beruete, M. Sorolla, I. Campillo, J. S. Dolado, L. Martín-Moreno, J. Bravo-Abad, and F. J. García-Vidal, "Enhanced millimeter-wave transmission through subwavelength hole arrays," *Opt. Lett.*, vol. 29, no. 21, pp. 2500–2502, Nov. 2004.
- [23] M. Beruete, M. Sorolla, I. Campillo, J. S. Dolado, L. Martinn-Moreno, J. Bravo-Abad, and

- F. J. Garcia-Vidal, "Enhanced millimeter wave transmission through quasioptical subwavelength perforated plates," *IEEE Trans. Antennas Propag.*, vol. 53, no. 6, pp. 1897–1903, 2005.
- [24] F. Medina, F. Mesa, and R. Marqués, "Extraordinary transmission through arrays of electrically small holes from a circuit theory perspective," *IEEE Trans. Microw. Theory Tech.*, vol. 56, no. 12, pp. 3108–3120, 2008.
- [25] M. Beruete, M. Navarro-Cia, and M. Sorolla Ayza, "Understanding Anomalous Extraordinary Transmission From Equivalent Circuit and Grounded Slab Concepts," *IEEE Transactions on Microwave Theory and Techniques*, Sep-2011. [Online]. Available: <http://ieeexplore.ieee.org/lpdocs/epic03/wrapper.htm?arnumber=5958636>.
- [26] M. Beruete, M. Navarro-Cía, S. A. Kuznetsov, and M. Sorolla, "Circuit approach to the minimal configuration of terahertz anomalous extraordinary transmission," *Appl. Phys. Lett.*, vol. 98, no. 1, pp. 3–5, 2011.
- [27] T. Weiland, "A discretization method for the solution of Maxwell's equations for six-component Field," *Int. J. Electron. Commun.*, vol. 31, no. 3, pp. 116–120, 1977.
- [28] "CST HELP." [Online]. Available: CST STUDIO SUITE 2014\Online Help\cst_studio_suite_help.htm.
- [29] "ABmm millimetre." [Online]. Available: <http://www.abmillimetre.com/Products.htm>.

6. Author's merits

International Conferences

- I. Jáuregui, P. Rodríguez-Ulibarri, S. A. Kuznetsov, M. Beruete, "THz sensing with classical FSS", The 10th International Congress on Advanced Electromagnetic Materials in Microwaves and Optics, Metamaterials 2016 (2016). **Accepted.**

National Conferences

- P. Roriguez-Ulibarri, I. Jáuregui, S. A. Kuznetsov, M. Beruete, "THz sensing structures based on classical cross-dipole FSS", XXXI Simposium Nacional de la Unión Científica Internacional de Radio, URSI 2016, (2016). **Accepted.**

Journal Papers

- International journal paper on preparation.